CHAPTER

3

EXPERIMENTAL ASPECTS OF NMR SPECTROSCOPY

Theoretical descriptions of the basics of NMR spectroscopy have been presented in Chapters 1 and 2. This chapter discusses aspects of experimental NMR spectroscopy that are essential for acquisition of one-dimensional spectra and that serve as building blocks for more complex multidimensional techniques to be introduced in Chapters 4, 6, and 7.

3.1 NMR Instrumentation

Figure 3.1 illustrates a block diagram of a pulsed Fourier transform NMR spectrometer. The main subsystems of an NMR spectrometer are the superconducting magnet, probe, pulse programmer and rf transmitter, receiver, and data acquisition and processing computer. A brief description of each of these components follows. Necessary adjustments of the spectrometer for routine use are described in subsequent sections of this chapter.

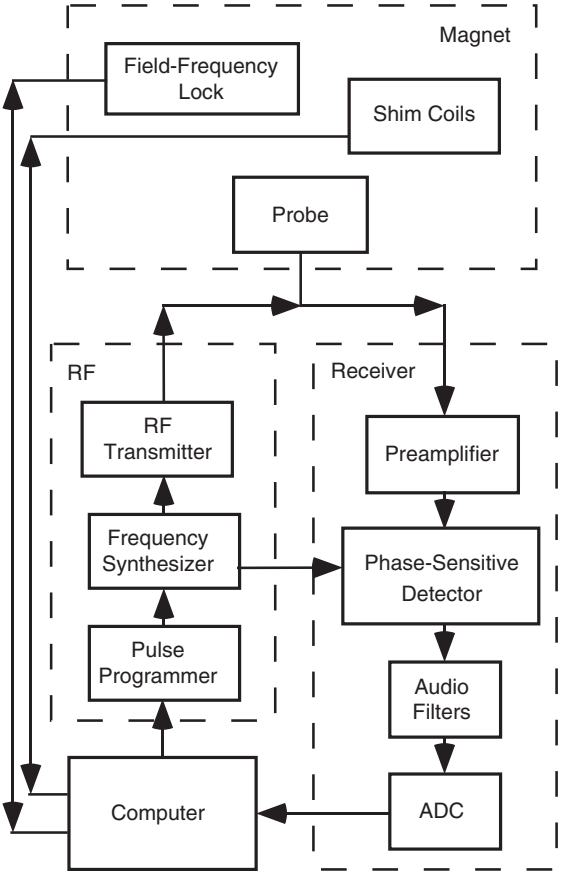

FIGURE 3.1 Block diagram of an NMR spectrometer. The major components — including the magnet, rf electronics, receiver, and computer — and important subsystems are illustrated.

A schematic of a superconducting magnet system is illustrated in Fig. 3.2. The magnet consists of a superconducting solenoid immersed in liquid helium. The liquid helium dewar is surrounded by a thermal radiation shield, a vacuum space, and an outer dewar filled with liquid nitrogen. The room-temperature bore of the magnet is centered on the z-axis of the solenoid and houses the room-temperature shim coils and the probe. NMR spectroscopy requires enormous magnetic fields with extremely high homogeneity over macroscopic volumes.

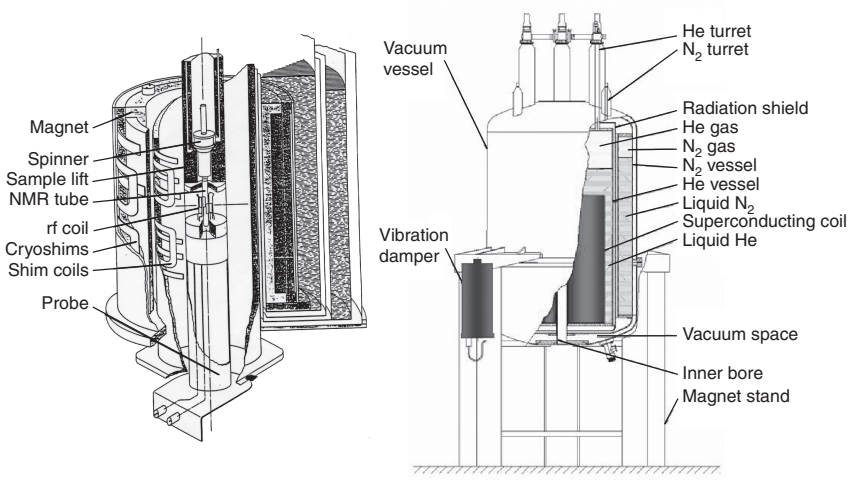

FIGURE 3.2 Cutaway diagram of a superconducting magnet. The probe, sample spinner, and room-temperature shim coils are positioned coaxially in the room-temperature bore of the magnet. The solenoid and cryoshim coils are immersed in liquid helium. The helium dewar is surrounded by a thermal radiation shield, vacuum space, and a liquid nitrogen dewar. Diagram courtesy of Bruker Instruments, Inc.

Present-generation magnets have field homogeneities on the order of 1 part in 10^9. As of 2005, the largest commercially available magnets have magnetic field strengths of 21.1 T with ^{1}H Larmor frequencies of 900 MHz. In the absence of other effects (such as increased contributions to the linewidth from chemical shift anisotropy, discussed in Section 5.4.4), the resolution in an NMR spectrum increases linearly with B_0 and the sensitivity increases as $B_0^{3/2}$ (*1*). Thus, a 900-MHz spectrometer should have 50% greater resolution and 84% greater sensitivity than a 600-MHz spectrometer. The impetus for continued development of higher field magnets is therefore obvious.

For high-resolution NMR spectroscopy, the temporal stability and spatial homogeneity of the magnetic field are critical. Temporal stability is affected both by the inevitable slow decay of the magnetic field, typically less than 10 Hz/hr for modern magnets, and by perturbations due to local influences on the field. The latter include external magnetic fields and moving metal objects, such as elevators. The stability of the static magnetic field is maintained using the field-frequency lock system.

The lock circuitry is essentially a specifically tuned (usually to deuterium) NMR spectrometer that operates in parallel to the main spectrometer. The lock system continually measures the resonance frequency of deuterium, or other lock nuclei, in the sample. If the frequency begins to drift, then the electric current in a room-temperature electromagnet, called the Z_0 coil, housed in the bore of the superconducting magnet is adjusted to return the frequency of the lock nucleus to its nominal value. In most cases, deuterated solvents provide a convenient method for introducing the necessary deuterium nuclei into the sample. The spatial homogeneity of the magnetic field is optimized by adjusting the currents in a set of room-temperature electromagnets called shims. Procedures for shimming are discussed in Section 3.8.2.3.

The coupling that exists between the lock system and the magnet shimming is sometimes overlooked. As noted above, the lock system works by adjusting the electrical current in the Z_0 coil to provide a small magnetic field that compensates for variations in the main field. If the Z_0 coil (which is physically part of the shim stack) is imperfectly constructed, then the Z_0 coil will contribute an additional spatial inhomogeneity to the static magnetic field. This additional contribution to inhomogeneity gets progressively worse as the lock current in the Z_0 coil increases. Normally, inhomogeneity of the Z_0 field is treated simply as another contribution to overall inhomogeneity of the B_0 field, and is corrected during the shimming process. However, if the lock current appreciably changes after the shimming has been done, as would be the case during a long experiment on a magnet with a high drift rate, inhomogeneity due to the Z_0 coil can be reintroduced, degrading the spectral lineshape as a function of time.

The probe, illustrated in Fig. 3.3 is positioned coaxially in the room-temperature bore of the magnet. Probe design strongly affects the sensitivity of the spectrometer, the homogeneity of the B_1 rf fields, the susceptibility to rf heating of the sample, and the quality of the solvent suppression. In its simplest manifestation, the probe consists simply of an rf circuit containing one or more wire coils in proximity to the NMR sample. In principle, quadrature detection of the precessing magnetization can be obtained by using two orthogonal coils (one for detecting the x-magnetization and the other for detecting the y-magnetization). Orthogonal crossed coils tuned to the same frequency are difficult to construct and optimize; modern high-resolution probes utilize a single Helmholtz coil design and obtain quadrature detection as described in Section 3.2.2. In most designs, the same coil is used for applying rf pulses and for detecting subsequent evolution of the magnetization. Depending on the probe, rf circuits may be tuned to a single frequency, may be

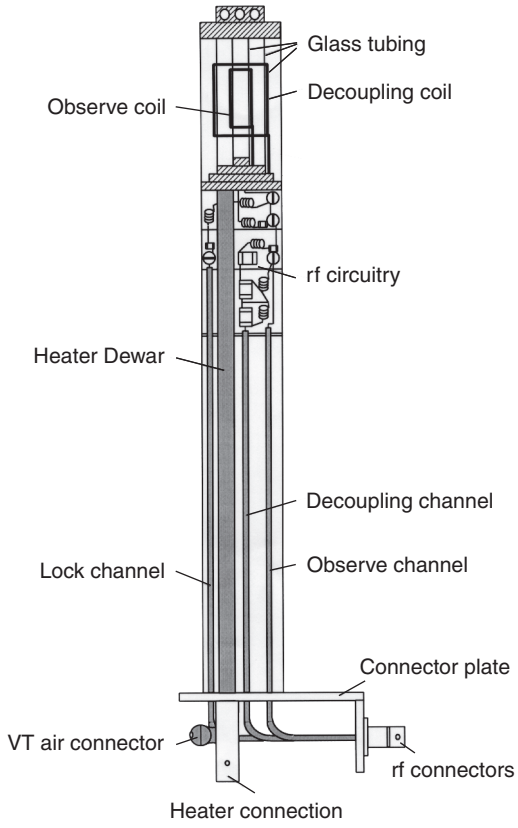

FIGURE 3.3 Probe assembly. Illustration of the major components of a high-resolution NMR spectroscopy rf probe. Diagram courtesy of Bruker Instruments, Inc.

double tuned to be simultaneously sensitive to two different nuclei, or may be tunable over a wide frequency range (as in a so-called broadband probe). For example, a triple-resonance ^{1}H–^{13}C–^{15}N probe contains two coils. One coil is double-tuned to ^{1}H and ^{2}H (for the lock system) and the other coil is double-tuned for ^{13}C and ^{15}N. The characteristics of the probe rf circuit are given by the quality factor, Q, and complex impedance, Z:

$$Q = \omega L/R, \qquad [3.1]$$

$$Z = R + i[\omega L - 1/(\omega C)], \qquad [3.2]$$

in which ω is the resonance frequency, L is the inductance, R is the resistance, and C is the capacitance of the coil circuit (for simplicity, the effects of the sample magnetism on the impedance have been omitted). The main task for the user is to tune the resonant frequency and match the impedance of the probe prior to use; other operating characteristics of the probe are difficult to alter without major reconstruction or retrofitting (Section 3.6.2.1).

In conventional NMR probes, the signal-to-noise (S/N) ratio is limited ultimately by thermal noise in the rf coil and preamplifier. The main factors contributing to the basic S/N ratio of NMR measurements are contained in the following expression (*2, 3*):

$$\mathrm{S/N} \propto \frac{N\gamma_e\gamma_d^{3/2}B_0^{3/2}K}{\sqrt{\Delta f(T_cR_c + T_a[R_c + R_s] + T_sR_s)}}, \qquad [3.3]$$

in which N is the number of observed nuclei in the sample, γ_e and γ_d are the magnetogyric ratios of the excited and detected nuclei, respectively, B_0 is the static magnetic field strength, K is a factor dependent on the coil design, Δf is the receiver bandwidth (in Hertz), R_c and T_c are the resistance and temperature, respectively, of the coil, T_a is the noise temperature of the preamplifier, T_s is the sample temperature, and R_s is the resistance induced by the sample in the coil. Probes have been introduced commercially that provide increased S/N by cooling the rf coil and preamplifier to reduce the noise contributions from these sources. These probes are referred to as "cryogenic probes." In 2006, current-generation cryogenic probes operate at coil temperatures of $\sim$20 K and provide increases in sensitivity of approximately a factor of four for samples with low-conductivity buffers; the sensitivity increase is less than the theoretical maximum due to the need to thermally insulate the sample from the rf coil, which adversely affects the filling factor (the ratio of the sample volume to the effective volume of the rf coil). As indicated by [3.3], an unfortunate consequence of lowering T_c, R_c, and T_a is that the S/N ratio is much more sensitive to the sample resistance, R_s. The fact that R_s is proportional to the sample conductivity leads to the result that the achievable S/N in a cryogenic probe is highly dependent on the conductivity of the sample buffer. The buffer conductivity is dependent on both the concentration and the mobility of the ions in solution, and thus improvements in S/N can be achieved by use of low-mobility ions (*3, 4*). Improvements in S/N can sometimes be achieved simply by using a smaller diameter sample tube, especially if the

same absolute amount of sample material is retained (*5*); this approach works by reducing the coupling between the conductive sample and the rf coil, and can also be beneficial in noncryogenic probes. Employing sample tubes with asymmetric geometry and a "squashed" rf coil design also has been shown to reduce the sample resistance (*6*), providing another potential means of rendering cryogenic probe performance less susceptible to sample buffer conditions. Another possibility is to switch solvents: protein NMR experiments are normally performed using samples in aqueous buffer, but solvents with low conductivity have proved to be quite useful in cryogenic probe applications (*7*).

The rf transmitter consists of frequency synthesizers, amplifiers, and associated electronics for producing pulses of highly monochromatic rf electromagnetic radiation with defined phases and amplitudes. Typically, one transmitter subsystem is dedicated to ^{1}H frequencies; one or more additional transmitters are used to generate rf frequencies for heteronuclear spectroscopy. The amplitude of the rf field measured in frequency units is given by $\omega_1 = \gamma B_1$; therefore, proportionally higher power amplifiers are required for low-γ nuclei. Typical ^{1}H amplifiers have peak output powers of 50–100 W; broadband amplifiers for heteronuclear spectroscopy have peak output powers in the range of 300–1000 W. The pulse programmer implements the pulse program necessary to perform an NMR experiment by controlling the timing, durations, amplitudes, and phases of the rf pulses. Radiofrequency pulses with arbitrary phase angles are generated by applying a phase-shifted rf field that is linearly polarized along a fixed axis in the laboratory reference frame (see [1.18]).

Careful consideration and consistent treatment of the signs of NMR frequencies and phases are important for proper implementation of experiments and interpretation of spectral data. Levitt and co-workers have identified a number of sign inconsistencies that are introduced in the hardware, the pulse programming language, and the data processing software among different commercial NMR spectrometers (*8, 9*). These inconsistencies frequently are unnoticed, because the errors introduced by each mutually cancel in many, but not all, circumstances. The following discussion focuses on the convention employed for the signs of the phases of rf pulses, because the choice of convention directly impacts the practical implementation of certain pulse sequences, such as those employed in Transverse Relaxation Optimized Spectroscopy (TROSY; Chapter 7) or other spin-state-selective experiments. Levitt emphasizes that the sense of the phase shift of the rf nutation axis (phase shift of the rf pulse) and the sense of the nutation itself (rotation by the pulse) must be distinguished. The convention chosen for the sense of the nutation

has no practical consequences and both "positive" and "negative" conventions are found in the literature; a positive (right-handed) rotation convention is mathematically convenient and conforms to the usage of Ernst and co-workers (*10*) as well as of this text. On the other hand, the convention chosen for the sense of the phase shift of the nutation axis is very important, and must be taken into account when implementing pulse sequences on a particular NMR spectrometer.

The effect of the sense of the nutation axis phase shift is illustrated by the two-pulse experiment:

$$90_x\text{–}\tau\text{–}90_\phi, \qquad [3.4]$$

in which $\tau = 1/(4\nu)$ and ν is the resonance offset (measured in Hz). If ν is positive, the magnetization vector initially collinear with the $+z$-axis (i.e., the direction of the static external field $\mathbf{B}_0$) is rotated to the $-z$-axis if the pulse phase $\phi = +y$. In contrast, if $\phi = -y$, then the magnetization is rotated to the $+z$-axis. The resulting orientation of the magnetization is obviously quite different in these two cases, and the sense of the nutation axis phase shift is absolutely critical to determining the final outcome in this example.

Standard conventions for the sense of the nutation axis phase shift have not been adopted by commercial spectrometer manufacturers. Thus, if the two-pulse experiment is performed by coding the pulse sequence with explicit phase $\phi = +y$, different results will be obtained using spectrometers from different manufacturers; however, all spectrometers manufactured by a given company appear to maintain a consistent convention. The origin of the different sign conventions stems from the control of the rf carrier phase. The rf generation scheme of a transmitter (xmtr) channel of an NMR spectrometer includes a carrier wave of the general form

$$s^{\text{xmtr}}(t) \cong \cos\left(\left|\omega^{\text{xmtr}}\right| t + \psi^{\text{xmtr}}\right), \qquad [3.5]$$

in which $|\omega^{\text{xmtr}}|$ is a positive number representing the oscillation frequency of the carrier wave as generated by the frequency synthesis scheme, and ψ^{xmtr} is a phase constant. The pulse programming software specifies the phase ψ^{xmtr} to control the phase of an rf pulse derived from the signal $s^{\text{xmtr}}(t)$. However, the relationship of this "raw" phase to the rotating-frame nutation axes is dependent on a number of hardware-specific design elements, such as the rf mixing schemes employed to generate the final transmitted rf pulse from $s^{\text{xmtr}}(t)$ (*9*); thus, the hardware phase changes implemented via ψ^{xmtr} do not necessarily correspond to the desired sense of the nutation axis phase shifts that

determines spin dynamics. In addition, most, if not all, commercial NMR spectrometer software packages lack a mechanism for accounting for the sign of the magnetogyric ratio of the spins being observed or manipulated. For example, the sense of nutation around a rotating-frame axis during application of an rf pulse is reversed for spins with negative versus positive gyromagnetic ratios, due to the relationship $\omega_1 = -\gamma B_1$.

The preceding issues become particularly relevant when translating the results of a spin dynamics calculation or a published pulse sequence into the actual pulse sequence code for a particular spectrometer. For example, if the spin dynamics calculations call for a pulse with $+y$ phase, then the spectroscopist needs to know whether to specify a pulse with $+y$ or $-y$ phase in the pulse programming language of the NMR spectrometer. In many experiments, the lack of rigor in specifying the sense of the nutation axis phase shift has no significant consequence. If a $(+y, -y)$ two-step phase cycle is employed to select for or against a particular spin coherence or polarization — for example, in a heteronuclear single-quantum correlation (HSQC) experiment — then uncertainty as to the sense of the phase shift only results in an inconsequential 180° phase shift of the detected signal. In other cases, however, such as the TROSY experiment, proper translation of the spin dynamic phases into the required hardware phases is essential. Typically, when a pulse sequence is reported in the literature, the pulse phases correspond to those employed on the NMR spectrometer used for testing the experiment. To code that pulse program for a spectrometer from another vendor, any difference in the sense of nutation axis phase shifts, related to different vendors' spectrometers, must be taken into account. Oftentimes, the proper phase shifts can be determined simply by running a test experiment; if the expected result is not obtained, then the usage of $+y$ and $-y$ pulses should be reversed.

Useful information about the sense of the nutation axis phase shifts can be gained from the simple two-pulse experiment used as an illustration at the beginning of this discussion, applied to any sample in H_2O. Place the ^1H transmitter frequency upfield (i.e., to the right) of the water resonance by some offset ν, and apply a 90° $+x$ pulse. According to the sign analysis provided by Levitt (*8, 9*), the water magnetization will precess from the $-y$-axis toward the $-x$-axis in the rotating frame. After the delay period τ, the magnetization will be aligned approximately along the $-x$-axis. At that point, a $+y$ pulse should return the water magnetization to the $+z$-axis, and thus subsequent detection of the free induction decay (FID) should show a minimal signal, relatively speaking. On the other hand, if the sense of

$+y$ and $-y$ pulse phases has been reversed on the spectrometer in use, the water magnetization will be placed approximately along the $-z$-axis after the second pulse. Subsequent detection of the FID will reveal an enormous signal from the water magnetization as it traverses through the x–y plane as a result of radiation damping. The specific phase convention employed by two spectrometer manufacturers has been documented by Roehrl et al. (*11*).

The receiver includes the preamplifier, phase-sensitive detector, and analog-to-digital converter. The preamplifier provides an initial stage of amplification of the NMR signal prior to further detection and processing. The noise figure of the preamplifier is a critical parameter fixing the signal-to-noise level of the spectrometer, because subsequent amplification and detection stages in the receiver unavoidably amplify the preamplifier noise along with the signal. To minimize losses, the preamplifier is located as close to the probe as practical. The phase-sensitive detector achieves quadrature detection of the signal as described in Section 3.2.2. The detector also includes audio filters designed to restrict the frequency bandwidth of the receiver. As discussed in Section 3.2.1, the filters reduce the amount of noise aliased into the spectrum. Unavoidably, the intensity of signals with frequencies near the cutoff of the filters will be attenuated. In addition, the time constants of the audio filters are one of the significant sources of phase errors in NMR spectroscopy (*12*). The analog-to-digital converters (ADCs) convert the amplified analog signal to binary numbers for subsequent digital processing. Current-generation NMR spectrometers use 16-bit digitizers as a compromise between conversion speed and dynamic range. A 16-bit digitizer can represent numbers between -2^8 and 2^8-1 ($-32{,}768$ to $32{,}767$). Clearly, the magnitude of the analog signal must not exceed the dynamic range of the ADC (or of earlier amplification stages). Similarly, if the magnitude of the analog signal is too small (approximately less than 1/2 bit), then the analog signal rarely registers on the ADC. In this case, extremely long acquisitions will be required to detect the signal and the results will contain distortions from digital quantization noise (i.e., the signal will only be observed to take on a limited number of digital values, see Section 3.2.2).

The data acquisition and processing system which may consist of multiple computers, control the operation of the various spectrometer components. In particular, the data acquisition computer must implement a pulse programming language to permit the user to control the pulse programmer. The processing computer must permit digital signal processing of the recorded time-domain signal to produce the frequency-domain spectrum.

3.2 Data Acquisition

In modern pulsed Fourier transform NMR spectrometers, transverse magnetization is generated by a series of one or more rf pulses. The evolution in time of the magnetization generates a time-varying voltage in the probe coil. The voltage is amplified and digitized by the receiver and recorded by the NMR spectrometer. The resulting voltage-versus-time signal is called an *interferogram* or *free induction decay*; the latter term refers specifically to the signal recorded during the acquisition period, whereas the term "interferogram" may refer either to the FID or to the signals detected indirectly during evolution periods of multidimensional NMR experiments. The digitized time-domain signal is (generally) Fourier transformed to generate the frequency-domain NMR spectrum. As discussed in the following sections, representation of a continuous time-varying signal by a discretely sampled, digitized sequence has profound consequences for NMR spectroscopy. Most of the considerations discussed here for acquisition and data processing of the observable magnetization signal apply equally well to acquisition and processing of the signals recorded indirectly during the evolution periods of multidimensional NMR experiments. Issues particularly important for multidimensional NMR spectroscopy are discussed in Chapter 4.

3.2.1 SAMPLING

The continuous NMR signal, $s(t)$, is sampled at evenly spaced time intervals and is represented as $s(k\Delta t)$ for $k = 0, 1, \ldots$, in which the sampling interval is Δt. The *Nyquist frequency*,

$$f_{\mathrm{n}} = 1/(2\Delta t), \qquad [3.6]$$

defines the highest frequency sinusoidal signal that is sampled at least twice per period if the sampling rate is Δt^{-1}. The Nyquist frequency plays a central role in digital signal processing applications, including NMR spectroscopy, because of the sampling theorem (*13*):

> *If a continuous function in time, $s(t)$, is bandwidth limited to frequencies smaller in magnitude than some value f_c, then the continuous function is completely determined by the discretely sampled sequence, $s(k\Delta t)$, provided that the sampling interval Δt is such that $f_n \geq f_c$.*

The sampling theorem requires that the sampling interval be $\Delta t \leq 1/(2f_c)$ or that the sampling rate be greater than or equal to $2f_c$. If the conditions of the sampling theorem are met, then the continuous function is given identically by

$$s(t) = \sum_{k=-\infty}^{\infty} s(k\Delta t)\,\mathrm{sinc}[2\pi f_n(t - k\Delta t)], \qquad [3.7]$$

with $\mathrm{sinc}(x) = \sin(x)/x$.

If a signal is recorded with a sampling interval Δt, then the frequency range accurately represented is given by

$$-f_n \leq \nu \leq f_n. \qquad [3.8]$$

The total frequency interval is termed the spectral width, SW, and is given by

$$\mathrm{SW} = 2f_n = 1/\Delta t. \qquad [3.9]$$

If the signal is not bandwidth limited, then the signal components with frequencies $|\nu| > f_n$ appear artifactually within the frequency range $-f_n \leq \nu \leq f_n$. The spurious representation of frequencies greater than the Nyquist frequency is called *folding* or *aliasing*. As discussed in Section 4.3.4.3, conventional NMR usage ascribes slightly different meanings to the two terms. As a result of the sampling theorem, the frequency spectrum represented by the signal sequence must be periodic with a period equal to $2f_n = 1/\Delta t$. Thus, a frequency, $\nu > f_n$ appears in the spectrum of a complex data sequence at an aliased frequency, ν_a, given by,

$$\nu = 2mf_n + \nu_a, \qquad [3.10]$$

in which m is an integer. Equation [3.10] indicates that frequencies greater than f_n (or less than $-f_n$) are "wrapped around" and appear at the other edge of the spectrum. By way of illustration, Fig. 3.4 shows two cosine waves with frequencies ν_0 and $\nu_1 = \nu_0 + 2f_n$. The discretely sampled points are identical for each sine wave; thus, both signals will be represented identically in the sampled data, and the frequency ν_1 will be aliased to the frequency ν_0. In general, aliased or folded peaks have systematically altered phases because the frequency-dependent phase error is a function of ν_0 but the phase correction applied is a function of ν_a. This property can be used to identify aliased peaks. Because ν_a depends upon the spectral width, folded or aliased peaks will change their apparent positions in the spectrum if the spectral width is changed.

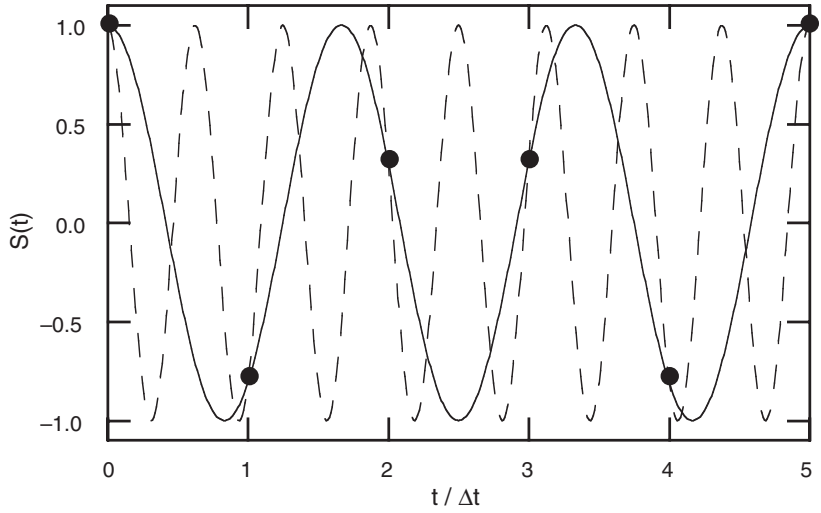

FIGURE 3.4 The Nyquist theorem. Sine waves with frequencies ν_0 (solid line) and $\nu_0 + 2f_n$ (dashed line) are illustrated. The two sine waves are sampled digitally at the Nyquist frequency Δt. The digital representations of the two sine waves are identical (solid dots). As a consequence, the two sine waves appear to have the same frequency in the digitally sampled data, and the high-frequency component is aliased to the lower frequency.

Folding and aliasing are used to advantage in multidimensional NMR spectroscopy to minimize the spectral width in the indirectly detected dimensions (Section 4.3.4.3).

3.2.2 OVERSAMPLING AND DIGITAL FILTERS

At first glance, the sampling theorem would appear to present a fatal flaw for Fourier transform NMR. Because the noise in the continuous signal would be expected to be nearly white (i.e., to have an infinite bandwidth), an infinite amount of noise power would be aliased into the frequency-domain NMR spectrum. To avoid this catastrophe, the receivers in NMR spectrometers incorporate analog filters to limit the bandwidth of the signal. All filters have a passband, a stopband, and a transition band. Ideally, the passband would cover the entire spectral range of interest, and the stopband would eliminate any noise from being aliased into the region of interest. If the sampling rate is chosen to be the minimum allowed by the sampling theorem (Section 3.21.), then the passband of the analog filter must be at least as large as the observed

spectral width to avoid attenuation of the NMR signals. Unfortunately, because the transition band between the pass- and stopbands of any filter is finite, some noise unavoidably will be aliased into the spectrum. The regions near the edges of the spectral window will be most strongly affected.

In principle analog filters can be designed that have extremely sharp cutoffs (i.e., extremely narrow transition bands), which would minimize the problem of aliased noise. However, filters have two deleterious effects on the NMR spectrum: (*i*) the transient response of the filter to the incoming signal distorts the initial points of the FID and (*ii*) the group delay of the filter retards the phase evolution of the resonance signals and results in frequency-dependent phase errors in the NMR spectrum (see Section 3.3.2.3) (*12*). As a result, filters with sharp cutoffs result in large, highly undesirable, phase distortions of the NMR spectrum.

The simplest and most effective solution is to employ a sampling rate significantly higher than the minimal rate required to avoid aliasing, a technique that is referred to as oversampling. The cutoff frequency of the analog filters is chosen such that any significant noise that is aliased into the spectral window will fall in the wings of the spectrum, outside the spectral region containing NMR signals. In addition, simpler analog filters that have more favorable phase characteristics can be employed, because the criterion for the width of the transition band can be relaxed. In principle, data storage requirements are increased when oversampling is used, because more data points must be acquired to obtain the same digital resolution. Although this was a significant concern in the past, advances in storage technology have all but eliminated the need to compromise acquisition parameters to minimize data sizes.

Oversampling also has important consequences for quantization noise. When the NMR signal is fed to the analog-to-digital converter, the continuous range of analog signal amplitudes is transformed to a discrete and finite set of numbers. The minimum step size between distinct numbers is determined by the number of bits in the ADC; the greater the number of bits, the smaller the step size for a given maximum allowable signal amplitude. The current generation of commercial solution-state NMR spectrometers typically employs 16-bit ADCs. Because the continuous-valued analog signal can only be converted to a finite number of distinct digital values, errors are introduced. If the analog signal at a given sampling point n is $y(n)$ and the nearest output level of the ADC is $y_q(n)$, then the digitized signal will have a quantization error of $e(n) = y(n) - y_q(n)$. For most practical purposes, the quantization error can be modeled as a random variable uniformly

distributed over the appropriate error range Δ, in which Δ is the step size in the ADC. The basic assumptions underlying this model are that (1) the error $e(n)$ is uniformly distributed over the range Δ, (2) the error $e(n)$ and the error $e(m)$ for $m \neq n$ are uncorrelated, and (3) the error $e(n)$ is uncorrelated with the ADC input $y(n)$. Although these assumptions do not hold in general, they are valid when the quantization step size Δ is small and the signal sequence $y(n)$ traverses several quantization levels between two successive samples. In this model, the quantization error has the appearance of a noise source that is added to the NMR signal, which is therefore referred to as quantization noise. The effect of quantization noise is expressed in the form of a signal-to-noise (power) ratio, $S/N = 10 \log(P_s/P_n)$, where P_s is the signal power and P_n is the quantization noise power, which is given by $P_n = \Delta^2/12$. If the allowed signal range is $-0.5Y_m \leq y(n) \leq 0.5Y_m$, and a b-bit digitizer is employed, then $\Delta = Y_m 2^{-b}$. In this case, $S/N = 6.02b + 10.8 - 20 \log\left(Y_m/\sqrt{P_s}\right)$. For each additional bit used in the digitizer, the signal-to-quantization noise (power) ratio improves by 6 dB; the last term in this expression also indicates that a decrease in the S/N ratio will occur if the signal strength is not optimized to the full range of the digitizer. High-resolution digitizers are particularly important for sampling high dynamic range NMR data, i.e., data consisting of a superposition of signals of vastly different strength. If a weak signal is thought of as a weak modulation of a very strong signal, then the modulations will be subject to substantial error when digitized if the digitizer step size is on the order of, or larger than, the amplitude of the modulations. For this reason, the signal fed into the ADC should be maximized, while ensuring that the signal will never exceed the allowable range of the ADC for any FID anticipated during the experiment.

Once quantization noise has been minimized by making full use of the available bits in the digitizer, additional improvements can be obtained by oversampling. The spectrum of the quantization noise is evenly distributed up to the Nyquist frequency; therefore, an increase in the sampling rate will result in a reduction in the quantization noise as it is spread over the broader frequency range. In quantitative terms, the quantization root-mean-square noise will be reduced by a factor of $\sqrt{2}$ for each doubling of the sampling rate. In addition, the analog filter bandwidth is increased in step with the increase in the observed spectral window when oversampling. As a result, the noise level of the FID is increased. If the NMR data have a very high dynamic range and very low system noise (i.e., the noise level of the analog signal fed to the ADCs), then the additional noise fluctuations result in a greater chance

that the signal $y(n)$ will traverse at least several quantization levels between two successive samples. This effect thereby improves the validity of the statistical model for quantization noise.

Sampling rates of several hundred kilohertz at 16-bit resolution are readily attainable using modern ADCs. To take full advantage of the benefits of oversampling, the ADC must be run at or near its maximum sampling rate. As a result, the region containing the actual NMR signals will typically be only a small fraction of the total spectral width, and a very large number of data points will need to be sampled to maintain the same digital resolution as for the case in which oversampling has not been employed. To avoid the need to manipulate and archive such large data sets, which would be particularly burdensome in multidimensional experiments, a method for reducing the data size while preserving the benefits of oversampling is desired. For this purpose, digital filters are ideally suited (*14–16*). Generally speaking, a digital filter performs the same function on a digital signal as an analog filter does on an analog signal. The oversampled NMR data can be processed with a low-pass (or in some cases a bandpass) digital filter to suppress all of the noise outside of the spectral region of interest while simultaneously reducing the effective sampling rate by a factor D. The process of reducing the sampling rate by an integer factor D (down-sampling by D) is called *decimation*. Digital filters provide several advantages over analog filters. The performance of an analog filter can be affected by temporal variations in the characteristics of the electronic components from which it is constructed; a digital filter, on the other hand, is absolutely stable by its inherent nature. A digital filter allows for great flexibility in reconfiguring the digital signal processing operations by simply changing the algorithms employed, whereas reconfiguration of an analog filter requires a new circuit to be constructed. Digital filters allow for the possibility of adaptive filtering, where the filter performance is altered "on the fly" in response to changes in the characteristics of the time-domain signal.

An important criterion in designing digital filters for NMR data processing applications is that the filter should not introduce phase distortions within the passband of the filter. This requirement dictates the need for using a so-called finite impulse response (FIR) or nonrecursive filter. A general form for such a filter is given by

$$y(n) = \sum_{k=-(M-1)/2}^{(M-1)/2} c(k)x(n-k), \qquad [3.11]$$

where $x(n)$ is the time-domain input FID data, $y(n)$ is the filtered output data, and the M values (M odd) of $c(k)$ are the coefficients that definite the characteristics of the digital filter. Absence of phase distortion in the passband of the filter requires that the filter coefficients be symmetric about index 0, $c(-k) = c(k)$. A vast literature describes methods for designing the filter coefficients; input parameters for the filter design include the width of the passband, the allowable amplitude modulation in the passband, the width of the transition band, and the minimum attenuation level in the stopband. In typical NMR applications, filters with a few hundred coefficients are employed. The convolution calculation, [3.11], can be executed either in the spectrometer host computer or with dedicated digital signal processing hardware in the spectrometer receiver unit. Down-sampling of the FID to reduce the spectral window to a reasonable size can be accomplished simply by applying [3.11] only to every Dth input data point, which results in a decimation factor of D.

A significant challenge in implementing the digital filter algorithm [3.11] is posed by the question as to how to "prime" the filter (*17*). Inspection of [3.11] reveals that for the first $(M-1)/2$ output values (assuming for the moment that no decimation is performed), the required input data set is incomplete; $x(1)$ is the earliest available data point from the FID, whereas values back to $n = -(M-1)/2$ are required. In many applications of digital filter technology, the problem of missing data is rather inconsequential, because the transient distortion that results can be ignored. However, in NMR applications, faithful reproduction of the early part of the FID is critical for spectral fidelity, especially for minimizing baseline distortions. Therefore, the question of how to prime the filter cannot be ignored. This problem has been addressed in at least two fundamentally different ways in currently available commercial NMR spectrometers. The details of the different methods are proprietary to a large extent; however, the general principle behind each method can be recognized. In one approach, an approximation method is employed to introduce pseudo data in front of the FID to fill in for the missing real data. Various prescriptions exist for defining these pseudo data. In one approach, pseudo data points are calculated using the same window function that was employed in the design of the digital filter coefficients $c(k)$ (*17*). The general method of filling in the required real data by approximate pseudo data yields a filtered output signal that appears like a normal FID, and which can therefore be subjected to conventional, post-acquisition data processing. In the second approach, an alternate form

of [3.11] is used:

$$y(n) = \sum_{k=0}^{M-1} d(k)x(n-k), \qquad [3.12]$$

in which the filter coefficients $d(k)$ are symmetric about the midpoint $(M-1)/2$ and the missing data points for $2-M \leq n \leq 0$ are simply substituted with zeros. Consequently, the effective origin of the FID signal is delayed by $(M-1)/2$ points (prior to decimation) and the step response of the digital filter appears at the beginning of the filtered output signal. As a result, unconventional data processing steps are required to obtain the desired NMR spectrum. The most straightforward procedure is simply to Fourier transform the data as usual, and correct for the time shift in the origin of the FID by applying a large first-order phase correction of the NMR spectrum. The exact value of the required phase correction constant is determined by the details of the digital filter design and can be obtained from a lookup table. If the baseline of the FID is not centered about zero, baseline correction involving use of the step response of the digital filter, which requires exact knowledge of the digital filter coefficients, is required prior to Fourier transformation.

The problem arising from the step response of the digital filter is completely analogous to the situation that arises when analog filters are employed. The main practical difference is that the analog filters normally employed are of relatively low order, and thus the duration of the transient response is usually limited to a small number of points at the beginning of the FID. Digital filters, on the other hand, are designed to have very sharp cutoffs, and thus the step response affects a proportionally larger region of the FID. The tail end of the FID will also be affected by the filter step response as the filter runs out of real data. However, this issue is normally inconsequential, because the signal has typically decayed into the noise, and in any case is attenuated by the application of a window function prior to Fourier transformation.

To this point the discussion of digital filters has focused on their use to suppress signals above a specified cutoff frequency, i.e., in low-pass applications. However, a major advantage of digital filter technology is the versatility in filter design, and a bandpass filter can be designed as easily as can be a low-pass filter. A bandpass filter sometimes is employed in commercial spectrometers to eliminate quadrature images, as discussed in the next section.

3.2.3 QUADRATURE DETECTION

As has already been described, the frequencies of resonance signals in NMR spectroscopy are measured as offset frequencies from an rf reference frequency. Offset frequencies can be positive (resonance frequency greater than the reference) or negative (resonance frequency less than the reference). Characterization of a sinusoidal signal requires that both the sign and absolute magnitude of the offset frequency be determined. A single detector measures the trigonometric projection of the harmonic signal onto a reference axis. Thus, a single detector might measure the cosinusoidally varying component of the signal. The sign of the frequency cannot be determined from such a data sequence. As is well known, both the cosine and sine components of a harmonic signal must be recorded in order to determine the sign of the frequency. Sampling a signal in a manner such that both the sine and cosine components are recorded is known as *quadrature* detection.

In the earliest days of Fourier transform NMR spectroscopy, single-channel detection was the norm and the problem of determination of the sign of the offset was solved by placing the rf reference frequency at one edge of the frequency spectrum. In this case, all the resonance offset frequencies have the same sign, so that quadrature detection is unnecessary. Almost without exception, modern NMR spectrometers record the signal in quadrature during acquisition of the FID; consequently, the rf reference can be set in the middle of the frequency spectrum. The latter approach offers some significant experimental advantages: (*i*) the frequency range that must be excited by the rf pulses is reduced by half, which reduces rf transmitter power requirements by a factor of four; (*ii*) the required sampling rate is halved, which simplifies data acquisition hardware; and (*iii*) aliasing of noise into the spectrum is minimized.

As illustrated in Fig. 3.5, quadrature detection during acquisition is accomplished by dividing the signal produced in a single coil into two channels. The high-frequency (MHz) signals in the two channels are mixed with rf reference frequencies to generate audio frequency (kHz) signals. The two rf reference frequencies are 90° out of phase; therefore, the output of one channel consists of a cosine modulated signal at the frequency $\omega_0 - \omega_{\text{ref}}$ and the other channel consists of a sine modulated signal at the same frequency. The two channels constitute the quadrature pair for frequency discrimination. If the signal produced at the output of the probe and preamplifier is sinusoidally modulated as $\cos \omega_0 t$, and for simplicity, the initial signal phase is assumed to be zero without loss of

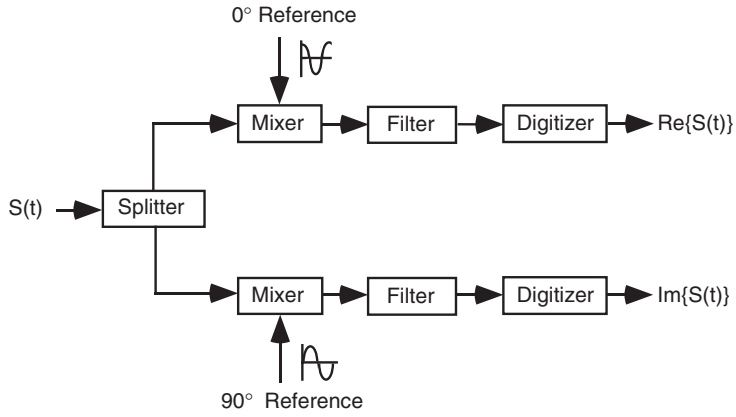

FIGURE 3.5 Experimental scheme for quadrature detection. The incoming signal recorded by the probe and preamplifier is split into two parallel channels. The signal in each channel is mixed with a reference signal, passed through a low-pass audio filter and digitized. Orthogonal components of the signal are obtained by shifting the relative phase of the reference signals by 90°.

generality, then the process of detection can be represented by

$$\begin{aligned}
\cos(\omega_0 t) &\xrightarrow{\text{Splitter}} \cos(\omega_0 t) - i\cos(\omega_0 t) \\
&\xrightarrow{\text{Mixers}} \cos(\omega_0 t)\ \cos(\omega_{\text{rf}} t) - i\cos(\omega_0 t)\ \sin(\omega_{\text{rf}} t) \\
&= \tfrac{1}{2}\ \cos[(\omega_0 + \omega_{\text{rf}})t] + \tfrac{1}{2}\ \cos[(\omega_0 - \omega_{\text{rf}})t] \\
&\quad - \tfrac{1}{2} i\ \sin[(\omega_0 + \omega_{\text{rf}})t] + \tfrac{1}{2} i\ \sin[(\omega_0 - \omega_{\text{rf}})t] \\
&\xrightarrow{\text{Audiofilters}} \tfrac{1}{2}\ \cos[(\omega_0 - \omega_{\text{rf}})t] + \tfrac{1}{2} i\ \sin[(\omega_0 - \omega_{\text{rf}})t] \\
&= \tfrac{1}{2}\cos[\Omega t] + \tfrac{1}{2} i\ \sin[\Omega t] \\
&= \tfrac{1}{2}\ \exp[i\Omega t],
\end{aligned} \qquad [3.13]$$

in which $i = \sqrt{-1}$ is used as a mathematical mechanism to distinguish between the signals in the two detection channels. The signal in the first (real) channel is modulated as $\cos \Omega t = [\exp(i\Omega t) + \exp(-i\Omega t)]/2$; therefore, the frequency-domain spectrum will contain two signals with positive amplitudes at frequencies $+\Omega$ and $-\Omega$. The signal in the second (imaginary) channel is modulated as $\sin \Omega t = [\exp(i\Omega t) - \exp(-i\Omega t)]/(2i)$; therefore, the frequency-domain spectrum will consist of a positive amplitude signal at a frequency of $+\Omega$, and a negative amplitude signal

at $-\Omega$. Combining the frequency-domain signals from the two channels as shown by [3.13] cancels the signals at a frequency of $-\Omega$ and yields a final frequency-domain spectrum containing a single signal with a frequency of $+\Omega$. The signals present at each step of the detection process are illustrated in Fig. 3.6. If the sensitivities of the two quadrature detection channels are not identical, the signal at $-\Omega$ will

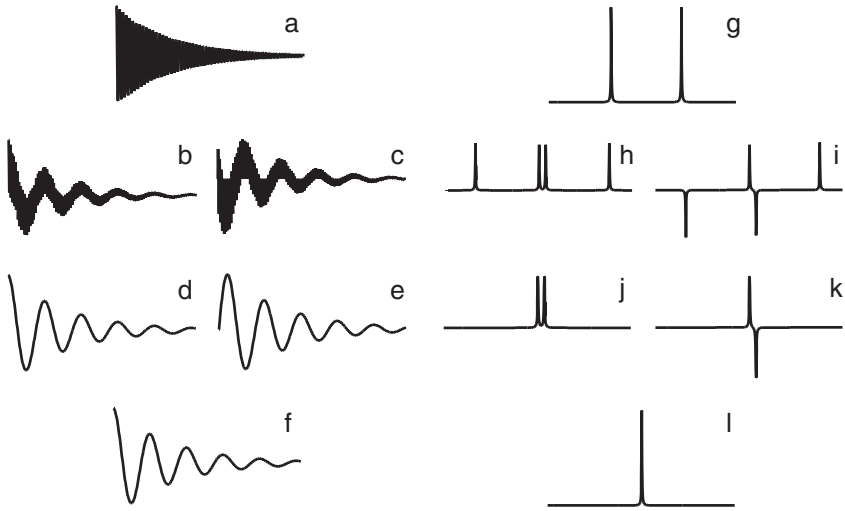

FIGURE 3.6 Quadrature detection. (a) The FID sampled by a single coil in the probe generates a signal modulated as $\cos(\omega_0 t)$ that yields (g) a frequency-domain spectrum consisting of signals at $\pm\omega_0$. To obtain quadrature detection, the signal is split into two channels. (b) The first channel is mixed with a reference signal modulated as $\cos(\omega_{rf} t)$ to generate a new FID. (h) The frequency-domain spectrum consists of signals at frequencies $\pm(\omega_0 - \omega_{rf})$ and $\pm(\omega_0 + \omega_{rf})$. (c) The second channel is mixed with a reference signal modulated as $\sin(\omega_{rf} t)$ to generate a new FID. (i) The frequency domain spectrum consists of signals at frequencies $\pm(\omega_0 - \omega_{rf})$ and $\pm(\omega_0 + \omega_{rf})$; however, because the sine function is odd, the symmetric signals are inverted relative to each other. (d, e) The filters remove the high frequency components of the two signal channels. (j, k) The resulting frequency domain spectrum contains only frequencies $\pm(\omega_0 - \omega_{rf})$. (f) The two channels are combined to yield a single complex data set. The frequency-domain spectrum, obtained by summing (j) and (k) or by transforming the complex data set (f), contains a single resonance signal at a frequency $\Omega = \omega_0 - \omega_{rf}$. For clarity, all sine-modulated signals have been phase shifted by 90° in the frequency domain, which is equivalent to multiplication by i when forming the complex signal $s(t) = s_x(t) + is_y(t)$, in which $s_x(t)$ and $is_y(t)$ are the outputs of the two quadrature channels.

not be identically nulled. The final frequency-domain spectrum will contain a small signal at a frequency of $-\Omega$ that is called a quadrature image. Cyclically ordered phase sequence (CYCLOPS) cycling frequently is used to reduce quadrature images (Chapter 4, Section 4.3.2.3). Techniques for quadrature detection during the evolution periods of multidimensional NMR experiments are discussed in Section 4.3.4.

It should be emphasized here that the detection scheme described here, in which the NMR signal is converted to the audio frequency range in a single mixing step, is an oversimplification of the actual design used in most current spectrometers. In order to optimize the performance of various electronic components, and to reduce the need for broadband frequency response, the mixing scheme is frequently implemented in two steps, with the NMR frequency first being converted down (or sometimes up) to some intermediate frequency (IF), and in a second step the quadrature detection scheme is implemented to convert the IF signal down to the audio frequency range.

A very recent development in spectrometer design has eliminated the need for a hardware quadrature detection scheme. This design has become feasible by the development of ultra-fast, high dynamic range analog-to-digital converters and fast digital signal processing hardware. In general terms, the NMR signal is converted down to some intermediate frequency range, such as 20 MHz, and converted directly to a digital signal, instead of being down-converted again to the audio frequency range. Digital signal processing techniques are then employed to down-sample the signal and select the spectral band of interest.

Although CYCLOPS phase cycling (Section 4.3.2.3) is very effective at eliminating quadrature images, it requires increasing the number of phase cycle steps by a factor of four, which frequently results in unacceptably long data acquisition times in multidimensional NMR experiments. A clever alternative can be implemented on modern commercial spectrometers equipped with digital filter technology (Section 3.2.2). The basis of this technique is quite simple. The NMR experiment is performed in a normal fashion until the start of the acquisition period. At that point, the receiver reference frequency is shifted past one end of the range of NMR signals, so that all NMR signals have the same sign, relative to the receiver reference. The FID is then recorded, using oversampling to ensure that no aliasing occurs, even with the shifted receiver reference frequency. Thus, any quadrature images that may exist will occur on the opposite side of the receiver reference, in an otherwise blank spectral region. At this point, instead of using a low-pass digital filter, a bandpass filter is used to select the

spectral region containing the NMR signals, and reject the region containing the quadrature images. The resulting NMR spectrum is completely free of quadrature images, without any need for increasing the length of the phase cycles. As an added bonus, any DC offset in the FID also is eliminated and baseline correction prior to Fourier transformation is unnecessary. Even though this procedure, referred to as Digital Quadrature Detection (DQD) by one of the commercial instrument manufacturers, is very effective, it should not substitute for careful calibration of the amplitude and phase balance of the quadrature channels in the receiver.

3.3 Data Processing

The representation of the NMR signal as a discrete sampling sequence in digital form means that powerful numerical digital signal processing techniques can be used to extract the information content of the signal. The most common processing approach is to convert the time-domain signal into a frequency-domain spectrum by applying a Fourier transform. Various processing algorithms can be applied prior to or after the Fourier transformation to optimize the resulting spectrum. In addition, alternative techniques for spectral analysis, generally first applied in electronic or optical signal processing fields, are increasingly being applied to NMR spectroscopy to obviate the drawbacks to Fourier transformation (Section 3.3.4). A comprehensive monograph of data processing in NMR spectroscopy has been published (*18*).

3.3.1 FOURIER TRANSFORMATION

The Fourier transformation as applied in NMR spectroscopy defines a relationship between one function in the time domain and another function in the frequency domain (*19*):

$$\begin{aligned} S(\omega) &= \mathscr{F}\{s(t)\} = \int_{-\infty}^{\infty} s(t)e^{-i\omega t}dt, \\ S(\nu) &= \mathscr{F}\{s(t)\} = \int_{-\infty}^{\infty} s(t)e^{-i2\pi\nu t}dt, \end{aligned} \qquad [3.14]$$

in which $\omega = 2\pi\nu$. The two functions $s(t)$ and $S(\omega)$ [or $s(t)$ and $S(\nu)$] are said to form a Fourier transform pair. The inverse Fourier transformations are defined by

$$\begin{aligned} s(t) &= \mathscr{F}^{-1}\{S(\omega)\} = \frac{1}{2\pi}\int_{-\infty}^{\infty} S(\omega)e^{i\omega t}d\omega, \\ s(t) &= \mathscr{F}^{-1}\{S(\nu)\} = \int_{-\infty}^{\infty} S(\nu)e^{i2\pi\nu t}d\nu. \end{aligned} \quad [3.15]$$

Fourier transformation and inverse Fourier transformation are linear operations and satisfy the following relationships,

$$\mathscr{F}\{cs(t)\} = \mathscr{F}\{s(t)\}, \quad [3.16]$$

$$\mathscr{F}\{s(t)+r(t)\} = \mathscr{F}\{s(t)\}+\mathscr{F}\{r(t)\}, \quad [3.17]$$

in which c is a complex constant.

For completeness, some important theorems concerning Fourier transformations are now listed. Proofs of these theorems can be found in standard texts (*19*).

1. Similarity,

$$\mathscr{F}\{s(at)\} = \frac{1}{|a|}S(\omega/a) = \frac{1}{|a|}S(\nu/a). \quad [3.18]$$

2. Time shifting,

$$\mathscr{F}\{s(t-\tau)\} = e^{-i\omega\tau}S(\omega) = e^{-i2\pi\nu\tau}S(\nu). \quad [3.19]$$

3. Frequency shifting,

$$\begin{aligned} \mathscr{F}\{s(t)e^{-i\omega_0\tau}\} &= S(\omega-\omega_0), \\ \mathscr{F}\{s(t)e^{-i2\pi\nu_0\tau}\} &= S(\nu-\nu_0). \end{aligned} \quad [3.20]$$

4. Derivative theorem,

$$\mathscr{F}\left\{\frac{d^k}{dt^k}s(t)\right\} = (i\omega)^k S(\omega) = (i2\pi\nu)^k S(\nu). \quad [3.21]$$

5. Convolution. If the *convolution integral* of two functions $r(t)$ and $s(t)$ is defined as

$$r(t) * s(t) = \int_{-\infty}^{\infty} r(\tau)s(t-\tau)\,d\tau, \quad [3.22]$$

then

$$\mathcal{F}\{r(t) * s(t)\} = R(\omega)S(\omega) = R(\nu)S(\nu), \qquad [3.23]$$

6. Correlation. If the *correlation integral* of two functions $r(t)$ and $s(t)$ is defined as

$$\text{Corr}[r(t), s(t)] = \int_{-\infty}^{\infty} r(t+\tau)s(\tau)\,d\tau, \qquad [3.24]$$

then

$$\mathcal{F}\{\text{Corr}[r(t), s(t)]\} = R(\omega)S^*(\omega) = R(\nu)S^*(\nu), \qquad [3.25]$$

in which $S^*(\omega)$ and $S^*(\nu)$ are the complex conjugates of $S(\omega)$ and $S(\nu)$, respectively.

7. Parseval's theorem,

$$\int_{-\infty}^{\infty} |s(t)|^2 dt = \int_{-\infty}^{\infty} |S(\omega)|^2 d\omega = \int_{-\infty}^{\infty} |S(\nu)|^2 d\nu. \qquad [3.26]$$

These theorems have important practical consequences for NMR spectroscopy. The similarity theorem demonstrates that broadening of a function in one dimension results in narrowing of the function in the other dimension. The time-shifting theorem demonstrates that delaying acquisition (intentionally or due to instrumental delays) in the time domain results in a frequency-dependent phase shift in the frequency domain. The frequency-shifting theorem permits the apparent frequencies in the frequency domain to be shifted after acquisition. The convolution and correlation theorems provide efficient means of calculating the convolution and correlation of two functions. In most cases, the convolution or correlation of two functions is obtained more efficiently by Fourier transforming both functions, multiplying their transforms, and inverse Fourier transforming the product than by direct integration. As discussed later, apodization of the free induction decay in the time domain is performed to convolute the signal in the frequency domain with a more desirable lineshape function. Parseval's theorem demonstrates that the signal energy is identical in the two domains and implies that the information content of the signal is identical in the time and frequency domains.

The most important operation for pulsed Fourier transform NMR spectroscopy in liquids is the Fourier transform of the time-domain signal for a damped oscillator, which is given by

$$s(t) = I_0 \exp[(i\omega_0 - \lambda_0)(t + t_0) + i\phi_0] \qquad [3.27]$$

for $t \geq 0$; $s(t) = 0$ for $t < 0$. In [3.27], I_0 is the initial signal amplitude, ω_0 is the frequency, λ_0 is the decay constant (usually the transverse relaxation rate constant), ϕ_0 is the initial signal phase, and t_0 is the value of the initial sampling delay. The initial sampling delay may arise from instrumental delays or may be intentionally set. The Fourier transform of $s(t)$ is

$$\begin{aligned}
S(\omega) &= I_0 \ \exp[(i\omega_0 - \lambda_0)t_0 + i\phi_0] \int_0^\infty \exp\{[i(\omega_0 - \omega) - \lambda_0]t\}dt \\
&= I_0 \ \exp[(i\omega_0 - \lambda_0)t_0 + i\phi_0] \frac{\exp\{[i(\omega_0 - \omega) - \lambda_0]t\}}{i(\omega_0 - \omega) - \lambda_0}\Bigg|_0^\infty \\
&= I_0 \ \exp[(i\omega_0 - \lambda_0)t_0 + i\phi_0] \frac{-1}{i(\omega_0 - \omega) - \lambda_0} \\
&= I_0 \ \exp[(i\omega_0 - \lambda_0)t_0 + i\phi_0] \frac{-1}{i(\omega_0 - \omega) - \lambda_0} \ \times \ \frac{-i(\omega_0 - \omega) - \lambda_0}{-i(\omega_0 - \omega) - \lambda_0} \\
&= I_0 \ \exp[(i\omega_0 - \lambda_0)t_0 + i\phi_0] \frac{i(\omega_0 - \omega) + \lambda_0}{(\omega_0 - \omega)^2 + \lambda_0^2} \\
&= I_0 \ \exp[(i\omega_0 - \lambda_0)t_0 + i\phi_0][A(\omega) + iD(\omega)],
\end{aligned} \qquad [3.28]$$

in which the absorption, $A(\omega)$, and dispersion, $D(\omega)$, lineshapes can be expressed as

$$A(\omega) = \frac{\lambda_0}{\lambda_0^2 + (\omega_0 - \omega)^2}, \qquad [3.29]$$

$$D(\omega) = \frac{(\omega_0 - \omega)}{\lambda_0^2 + (\omega_0 - \omega)^2}. \qquad [3.30]$$

The Lorentzian lineshapes are illustrated in Fig. 3.7. The linewidth of the absorptive Lorentzian is defined as the full-width at half-height (FWHH) and is given by $\Delta\omega_{\mathrm{FWHH}} = 2\lambda_0$ or $\Delta\nu_{\mathrm{FWHH}} = \lambda_0/\pi$.

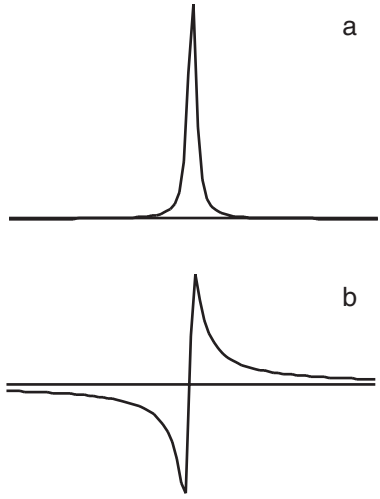

FIGURE 3.7 (a) Adsorptive and (b) dispersive Lorentzian lineshapes. The Fourier transform of an exponentially damped sinusoid generates a frequency-domain signal with real and imaginary components described by the adsorptive and dispersive Lorentzian functions, respectively.

The maximum and minimum cusps of the dispersive lineshape are separated by exactly the absorptive linewidth. Note that for large frequency offsets, the decay of the absorptive Lorentzian lineshape is proportional to $1/(\omega_0-\omega)^2$, but the decay of the dispersive Lorentzian lineshape is proportional to $1/(\omega_0-\omega)$. Accordingly, absorptive-phase lineshapes yield much more highly resolved NMR spectra and are greatly preferred to dispersive lineshapes.

Because the free induction decay is sampled digitally, the experimental frequency domain spectrum is calculated using the discrete Fourier transform

$$S(\nu) = S(k/N\Delta t) = \mathscr{F}\{s(j\Delta t)\} = \sum_{j=0}^{N-1} s(j\Delta t)e^{-i2\pi jk/N}, \qquad [3.31]$$

in which N is the number of (complex) data points, Δt is the sampling interval, $k = -N/2, \ldots, 0, \ldots, N/2$, and the digitized signal, corresponding to the continuous signal [3.27], is described by

$$s(j\Delta t) = I_0 \exp[(i\omega_0 - \lambda_0)(j\Delta t + t_0) + i\phi_0]. \qquad [3.32]$$

The inverse transform is given by

$$s(j\Delta t) = \mathscr{F}^{-1}\{S(k/N\Delta t)\} = \frac{1}{N}\sum_{k=0}^{N-1} S(k/N\Delta t)e^{i2\pi jk/N}. \qquad [3.33]$$

The frequency range represented by the Fourier transformed signal is $-1/(2\Delta t) \le \nu \le 1(2\Delta t)$ in discrete steps of $\Delta\nu = 1/(N\Delta t)$. In terms of the Nyquist frequency, $-f_n \le \nu \le f_n$ Equation [3.31] shows that the discrete Fourier transform of the N input signal points yields $N+1$ frequency domain data points. In fact, $S(f_n) = S(-f_n)$, so that only N unique points are obtained in the frequency-domain function. Most Fourier transformation algorithms provide as output the N points for $k = -N/2, \ldots, N/2-1$; i.e., the point $S(f_n)$ is not returned. Consequently, the zero frequency point in the frequency domain spectrum is not $k = N/2$ but rather $k = N/2 + 1$. The discrete Fourier transform [3.31] can be expressed as

$$S(\omega_k) = I_0 \exp[(i\omega_0 - \lambda_0)t_0 + i\phi_0]\frac{1 - \exp[N\Delta t(i\omega_0 - i\omega_k - \lambda_0)]}{1 - \exp[\Delta t(i\omega_0 - i\omega_k - \lambda_0)]}, \quad [3.34]$$

in which $\omega_k = 2\pi k/(N\Delta t)$ and the series [3.31] has been summed using the identity

$$\sum_{j=0}^{N-1} x^j = \frac{1 - x^N}{1 - x}. \qquad [3.35]$$

Equation [3.34] is equivalent to [3.28] if $\Delta t \to 0$ and $N \to \infty$ while $N\Delta t\lambda_0 \gg 1$. This limit represents quasi-continuous sampling of the time-domain signal until it has completely decayed.

If $s(j\Delta t)$ is a real function, then

$$\begin{aligned} S([N-k]/N\Delta t) &= \sum_{j=0}^{N-1} s(j\Delta t)e^{-i2\pi j(N-k)/N} \\ &= \sum_{j=0}^{N-1} s(j\Delta t)e^{-i2\pi j + i2\pi jk/N} \\ &= \sum_{j=0}^{N-1} s(j\Delta t)e^{i2\pi jk/N} \\ &= S^*(k/N\Delta t). \end{aligned} \qquad [3.36]$$

Equation [3.36] demonstrates that unique values of $S(k/N\Delta t)$ are obtained only for $k = 0, \ldots, N/2 - 1$. Thus, for an N-point real time-domain signal, a unique $N/2$-point complex frequency-domain spectrum is obtained. Incidentally, $S(0) = S^*(1/\Delta t)$ and is consequently a real number.

The discrete Fourier transform is never calculated numerically by using [3.31]. Direct calculation of the Fourier transformation is an order N^2 process, which means that the computational burden increases as the square of the number of data points. Instead, the discrete Fourier transformation is calculated using the Fast Fourier Transformation (FFT) algorithm, which is an order $N \log_2 N$ process. The time savings afforded by the FFT algorithm are enormous: for a data sequence of 256 complex points, the FFT algorithm is on the order of 32 times more rapid; for a data sequence of 4096 complex points, the FFT is on the order of 300 times more efficient. From the standpoint of the spectroscopist, the use of the FFT algorithm has one important consequence: the number of data points, N, must be an integral power of two (i.e., $N = 2^m$, with m an integer). If the acquired number of data points satisfy $2^{m-1} < N < 2^m$, then the data sequence must be extended to 2^m points. The data may be extended by zero-filling (Section 3.3.2.1) or by linear prediction (Section 3.3.4).

3.3.2 DATA MANIPULATIONS

Direct Fourier transformation of a recorded NMR signal rarely yields an optimal frequency-domain spectrum. Instead, a number of digital signal processing techniques are applied prior to (and after) Fourier transformation in order to maximize the information available from the spectrum.

3.3.2.1 Zero-Filling Zero-filling or zero-padding is the process of appending a sequence of zeros to a data sequence prior to Fourier transformation. For example, as described in Section 3.3.1, FFT algorithms require that the number of data points, N, be equal to an integral power of two. If $2^{m-1} < N < 2^m$ for an integer m, then, prior to Fourier transformation, zero-filling is used to generate a new data sequence of 2^m points in which all points greater than N have the value zero.

NMR data obey the *causality* principle because $s(t) = 0$ for $t < 0$; that is, the signal does not precede its cause (i.e., the pulse sequence). Somewhat surprisingly, as a consequence of causality, the real and imaginary components of the complex frequency spectrum have a

deterministic relationship embodied in the Kramers–Kronig relations (*20*):

$$\mathrm{Re}\{S(\omega)\} = \frac{1}{\pi}\int_{-\infty}^{\infty} \frac{\mathrm{Im}\{S(\omega')\}}{\omega - \omega'}\, d\omega',$$
$$\mathrm{Im}\{S(\omega)\} = -\frac{1}{\pi}\int_{-\infty}^{\infty} \frac{\mathrm{Re}\{S(\omega')\}}{\omega - \omega'}\, d\omega'. \qquad [3.37]$$

The mathematical operation indicated is called the Hilbert transform and permits the complex spectrum to be reconstructed given only the real component. The Hilbert transform finds frequent application in NMR spectroscopy. In many cases, particularly in multidimensional spectroscopy, the imaginary portion of the spectrum is discarded to reduce data storage requirements. Subsequently, the imaginary component of the spectrum can be regenerated by using [3.37]. The resulting complex spectrum can be phased normally.

However, as noted by Ernst, the Kramers–Kronig relations do not hold for discretely sampled NMR data unless the data sequence is extended by a factor of two by zero-filling, because the periodicity in the signal implicit in the discrete Fourier transform renders the real and imaginary components of the spectrum independent (*20*). Thus, if $2^{m-1} < N \leq 2^m$, then real improvement in the information content of an NMR spectrum is obtained by zero-filling to obtain a sequence of 2^{m+1} data points. Additional zero-filling results only in cosmetic interpolation between data points in the frequency domain; no additional information is obtained.

3.3.2.2 Apodization Direct Fourier transformation of an interferogram rarely yields a spectrum that is satisfactory in all respects. Most commonly, the spectrum will exhibit a number of shortcomings: truncation artifacts, low signal-to-noise ratios, limited resolution, or undesirable peak shapes. The properties of the spectrum can be improved by convoluting the spectrum with a more satisfactory lineshape function:

$$S_f(\omega) = H(\omega) * S(\omega). \qquad [3.38]$$

Because convolution in the frequency domain is equivalent to multiplication in the time domain, common practice is to multiply the interferogram prior to Fourier transformation by the time-domain filter

function, $h(t)$, that represents the Fourier transform of the desired frequency-domain lineshape function,

$$S_f(\omega) = \mathscr{F}\{h(t)s(t)\}. \quad [3.39]$$

This process is variously termed windowing, apodization, or filtering in the time domain (*10, 13*).

The digital signal processing literature contains a wealth of theoretical and empirical studies of apodization; nonetheless, relatively simple approaches have proved of greatest value in NMR spectroscopy. Of the theoretical results, only two will be mentioned:

1. Reduction of truncation artifacts requires that the time-domain signal be smoothly reduced to zero. The resulting frequency-domain lineshape is thereby broadened. The minimum truncation ripple for a given degree of broadening is given by the Dolph–Chebycheff window:

$$h(t) = \mathscr{F}^{-1}\left\{\frac{\cos[2(N-1)\ \cos^{-1}\{z_0 \cos(\omega\Delta t/2)\}]}{\cosh[2(N-1)\ \cosh^{-1}(z_0)]}\right\}, \quad [3.40]$$

   in which $N+1$ is the number of sample points, Δt is the sampling period,

$$z_0 = [\cos(\delta\Delta t/4)]^{-1}, \quad [3.41]$$

   and δ is the broadening parameter measured in radians/sec. The Dolph–Chebycheff window is not normally used because of the complexity of [3.40]; however, it serves as a benchmark for evaluating the efficacy of other filter functions.

2. Maximum signal-to-noise ratio is obtained in a spectrum if a matched filter function is applied prior to Fourier transformation. The matched filter $h(t)$ is equal to the envelope function of the signal, $s_e(t)$. The envelope function is the function describing the decay of the signal (stripped of its harmonic content).

The acquisition time for the interferogram in NMR spectroscopy is limited to times $t \leq t_{max}$. Because the Fourier transformation algorithm assumes that data extends to $t = \infty$, the input signal for Fourier transformation can be represented as the product of the signal (extending to $t = \infty$) and the rectangle function:

$$s'(t) = s(t)r(t),$$

$$r(t) = \left\{ \begin{array}{lll} 1 & \text{for} & 0 \le t \le t_{\max} \\ 0 & \text{for} & t > t_{\max} \end{array} \right\}. \qquad [3.42]$$

The resulting frequency spectrum is given by

$$S'(\omega) = \mathscr{F}\{s(\tau)r(\tau)\} = S(\omega) * \text{sinc}\,(t_{\max}\omega), \qquad [3.43]$$

in which $\text{sinc}(x) = \sin(x)/x$. As shown in Fig. 3.8, convolution of $S(\omega)$ with the sinc function produces severe oscillating *truncation artifacts*. The truncation artifacts can be reduced by apodization with a filter function that reduces the amplitude of the signal smoothly to zero at $t_{\max}$. Figure 3.8 shows the lineshapes obtained for the cosine, Hamming, and Kaiser filter functions, respectively:

$$h(t) = \cos(\pi t/2t_{\max}), \qquad [3.44]$$

$$h(t) = 0.54 + 0.46\cos(\pi t/t_{\max}), \qquad [3.45]$$

$$h(t) = I_0\left\{\theta\sqrt{\left(1 - t^2/t_{\max}^2\right)}\right\}/I_0\{\theta\}. \qquad [3.46]$$

In [3.46], $I_0\{\theta\}$ is the zero-order modified Bessel function and θ is a parameter that determines the degree of apodization of the signal. Typical values of θ are π, 1.5π, and 2π; increasing values of θ reduce the truncation ripples while increasing the degree of line broadening of the resonance signal. The cosine window perhaps is the window function most frequently applied to truncated NMR signals. Although the Hamming and Kaiser windows are used relatively infrequently, both are expected to more closely approach the performance of the Dolph–Chebycheff window (*10*). The Kaiser window has the added advantage that θ can be adjusted to optimize the trade-off between apodization and line broadening in particular circumstances.

The Hanning window function is given by

$$h(t) = 0.5 + 0.5\cos(\pi t/t_{\max}) \qquad [3.47]$$

and is equivalent, as may be shown using standard trigonometric identities, to the cosine-squared bell window function:

$$h(t) = \cos^2(\pi t/2t_{\max}). \qquad [3.48]$$

The performance of the Hanning function is inferior to the cosine, Hamming, and Kaiser window functions; consequently, the cosine-squared bell window function is not recommended for routine use.

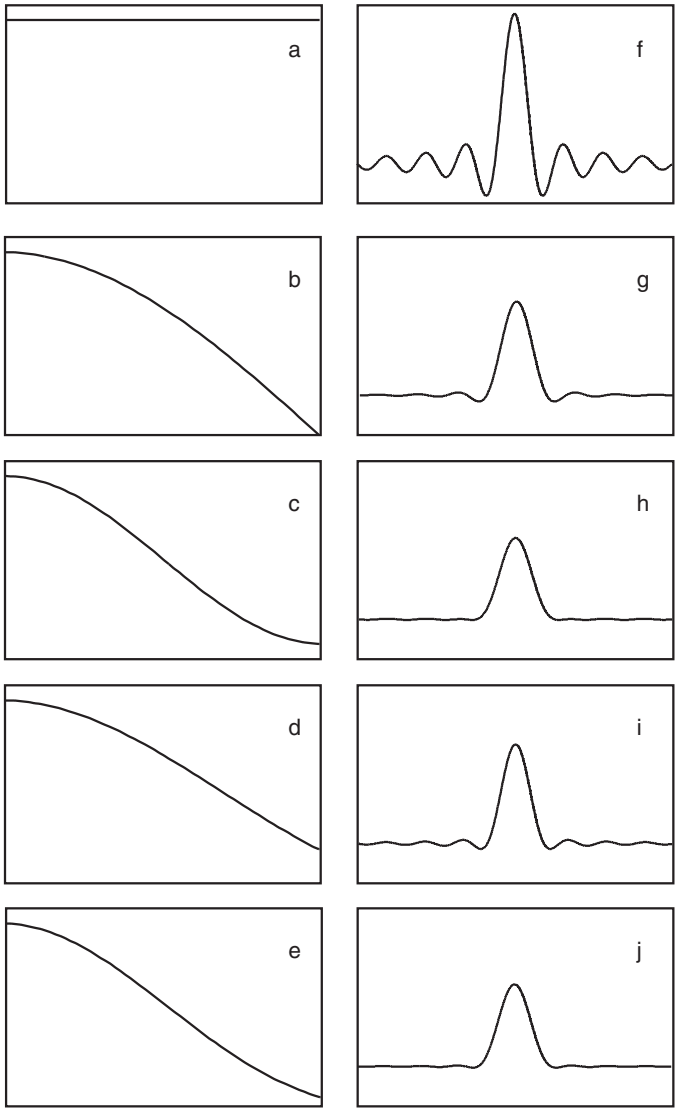

FIGURE 3.8 Window functions for apodization. In each case, the time-domain representation of the window function was zero-filled by a factor of two and Fourier transformed to yield the frequency-domain representation. (a) A uniform square wave input yields a (f) sinc function on output. Other apodization functions illustrated include (b, g) cosine bell, (c, h) Hamming function, (d, i) Kaiser window with $\theta = \pi$, and (e, j) Kaiser window with $\theta = 2\pi$.

The signals recorded during an NMR experiment are the sums of exponentially decaying sinusoidal functions. If sufficient data have been recorded to minimize truncation artifacts ($t_{max} > 3T_2$), then optimal sensitivity is obtained using the matched exponential filter function

$$h(t) = \exp(-\lambda t), \qquad [3.49]$$

in which λ is the line-broadening parameter. For matched filtering, $\lambda \approx \lambda_0 = R_2$ (i.e., 2λ is the full-width at half-height of the Lorentzian lineshape measured in s^{-1}). Matched exponential filtering has the effect of doubling the linewidth in the frequency domain. Matched exponential filtering has two drawbacks. First, because different resonance signals in the spectrum frequently have different linewidths, λ cannot be optimized for all lines simultaneously; thus, $h(t)$ invariably is an approximation to the desired matched filter. Second, the lineshape in the frequency domain is Lorentzian; consequently, the absorption lineshape decays as $1/\omega^2$. The resulting tails degrade resolution in the spectrum and hinder accurate integration of peak intensities. Despite these drawbacks, exponential filtering generally can be recommended for application to the FID recorded during the acquisition dimension of NMR experiments because the signal is rarely truncated severely during acquisition. Exponential filtering is applied to indirectly detected evolution periods very infrequently because the interferograms are almost always severely truncated.

Certain experiments, such as Correlation Spectroscopy (COSY) and multiple-quantum spectroscopy, yield antiphase peak shapes in the acquisition dimension. In these cases, the time-domain signal is initially zero and is sinusoidally modulated due to evolution of the scalar coupling interaction. Consequently, the exponential filter is not an appropriate matched filter. Instead, phase-shifted sine-bell functions frequently are applied:

$$h(t) = \sin\left[\pi\left(\frac{t + t_0}{t_{max} + t_0}\right)\right], \qquad [3.50]$$

in which $\pi t_0/(t_{max} + t_0)$ is the initial phase of the sine bell.

As noted previously, the natural lineshape in solution NMR spectroscopy is Lorentzian. The spectrum can be given a new lineshape by use of the filter function,

$$h(t) = s'_e(t)/s_e(t) = s'_e(t)\exp(\lambda t), \qquad [3.51]$$

in which $s'_e(t) = \mathcal{F}^{-1}\{S'(\omega)\}$, and $S'(\omega)$ is the desired lineshape. Lineshape transformations frequently are used to enhance the resolution in a

spectrum; however, resolution enhancement emphasizes later portions of the free induction decay. As a consequence, truncation artifacts may become more prominent (unless t_{max} is very large or the filter function is suitably apodized) and the signal-to-noise ratio in the spectrum may be reduced. As a corollary, resolution can be enhanced only if signal has been recorded for long times. If the data are truncated, then little resolution enhancement is possible using digital filtering (but see Section 3.3.4). The Lorentzian-to-Gaussian transformation is obtained using

$$s'_e(t) = \exp\left[-\frac{\lambda_g^2 t^2}{4\ln 2}\right] = \mathscr{F}^{-1}\left\{\frac{\sqrt{4\pi\ln 2}}{\lambda_g}\ \exp\left[-\frac{\omega^2 \ln 2}{\lambda_g^2}\right]\right\}. \qquad [3.52]$$

The resulting lineshape is Gaussian with a full-width-at-half-height equal to $\Delta\omega_{FWHH} = 2\lambda_g$ or $\Delta\nu_{FWHH}$

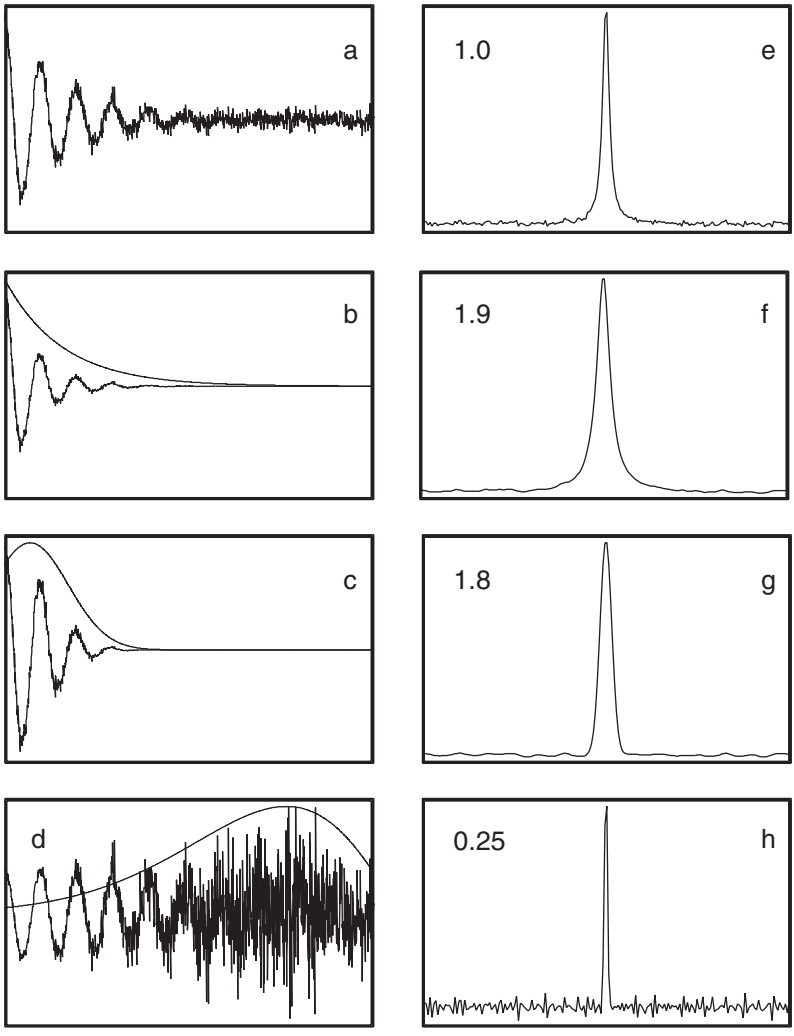

FIGURE 3.9 Digital resolution enhancement. (a) The unapodized FID and its (e) Fourier transform are illustrated. (b) A matched exponential window function and the resulting FID are shown together with (f) the resulting frequency-domain spectrum. (c) A Lorentzian-to-Gaussian transformation and the resulting FID are shown together with (g) the resulting frequency-domain spectrum. (d, h) Maximum resolution enhancement is obtained by multiplying the FID with an increasing exponential and apodizing with a Kaiser window function. The signal-to-noise ratio in (e) is arbitrarily assigned a value of unity; relative signal-to-noise ratios for (f, g, h) are shown in the figure.

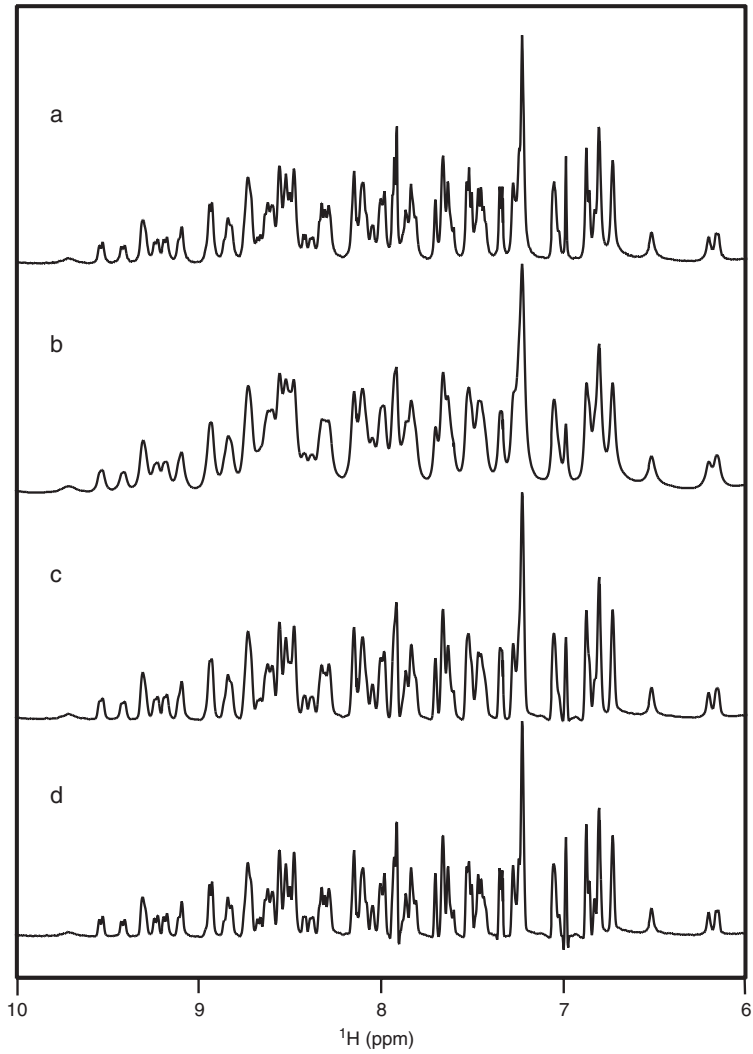

FIGURE 3.10 Digital resolution enhancement of ubiquitin ^{1}H NMR spectrum. The amide region from 6 to 10 ppm is illustrated for spectra obtained by Fourier transformation of (a) the unapodized FID, (b) an exponential window function, (c) a Lorentzian-to-Gaussian transformation, and (d) maximum resolution enhancement obtained by multiplying the FID with an increasing exponential and apodizing with a Kaiser window function. The window functions are similar to those used in Fig. 3.9. The signal-to-noise ratios for the resonance at 6.52 ppm are (a) 61, (b) 150, (c) 110, and (d) 73.

definition of the convolution function yields

$$A(S_f) = \int_{-\infty}^{\infty} \left[\int_{-\infty}^{\infty} H(\omega') S(\omega - \omega') d\omega' \right] d\omega. \quad [3.54]$$

Assuming that the order of integrations can be reversed,

$$A(S_f) = \int_{-\infty}^{\infty} \left[\int_{-\infty}^{\infty} H(\omega') S(\omega - \omega')\, d\omega' \right] d\omega$$

$$= \int_{-\infty}^{\infty} H(\omega') \left[\int_{-\infty}^{\infty} S(\omega - \omega')\, d\omega \right] d\omega'.$$

The part in square brackets on the last line is just the integral of the function $S(\omega)$, regardless of the value of ω' (because the integration limits are infinity); thus, the variable ω' can be dropped from the inner integral, which then gives

$$A(S_f) = \left[\int_{-\infty}^{\infty} H(\omega')\ d\omega' \right] \left[\int_{-\infty}^{\infty} S(\omega)\ d\omega \right]$$

$$= A(H)A(S). \quad [3.56]$$

The final results states that the integrated area of the apodized resonance peak is equal to the product of the area of the nonapodized peak and the area of the Fourier transform of the window function. Therefore, relative peak integrals within a spectrum are independent of the window function applied (assuming that $A(H) \neq 0$). Equation [3.56] also demonstrates that apodization does not alter peak integrals if $A(H) = 1$, which is the case if $h(0) = 1$, that is, if the initial value of the apodization function is unity.

3.3.2.3 Phasing The digitized signal represented by [3.27] gives rise to a spectrum given by [3.28] that displays a frequency-dependent phase error. The spectrum can be written as

$$S(\omega) = I_0 \exp[(i\omega_0 - \lambda_0)t_0 + i\phi_0][A(\omega) + i\,D(\omega)]$$

$$= I_0 \exp[-\lambda_0 t_0]\{\cos(\omega_0 t_0 + \phi_0)A(\omega) - \sin(\omega_0 t_0 + \phi_0)\ D(\omega)$$

$$+ i[\sin(\omega_0 t_0 + \phi_0)A(\omega) + \cos(\omega_0 t_0 + \phi_0)\ D(\omega)]\} \quad [3.57]$$

by straightforward application of the time-shifting theorem [3.19]. The real part of the spectrum is seen to be a mixture of absorptive and dispersive lineshapes, as shown in Fig. 3.11. The factor $I_0 \exp[-\lambda_0 t_0]$ in [3.57] affects only the intensity of the resonance signal and is not written explicitly in the following equation. Mathematically, the absorptive and dispersive components of the spectrum can be separated by constructing a new data set by using the following prescription,

$$\begin{aligned} S'(\omega) &= \exp[-i(\omega_0 t_0 + \phi_0)]S(\omega) \\ &= cos(\omega_0 t_0 + \phi_0)\,\mathrm{Re}\{S(\omega)\} + \sin(\omega_0 t_0 + \phi_0)\,\mathrm{Im}\{S(\omega)\} \\ &\quad + i[-\sin(\omega_0 t_0 + \phi_0)\,\mathrm{Re}\{S(\omega)\} + \cos(\omega_0 t_0 + \phi_0)\,\mathrm{Im}\{S(\omega)\}] \\ &= A(\omega) + i\,D(\omega). \end{aligned} \quad [3.58]$$

In practice, [3.58] cannot be used to phase a spectrum containing multiple resonances because ω_0 is different for each resonance. Instead, the phased spectrum is calculated as

$$S'(\omega) = u(\omega) + iv(\omega) \approx A(\omega) + i\,D(\omega), \quad [3.59]$$

in which

$$\begin{aligned} u(\omega) &= \cos[\theta(\omega)]\,\mathrm{Re}\{S(\omega)\} + \sin[\theta(\omega)]\,\mathrm{Im}\{S(\omega)\}, \\ v(\omega) &= -\sin[\theta(\omega)]\,\mathrm{Re}\{S(\omega)\} + \cos[\theta(\omega)]\,\mathrm{Im}\{S(\omega)\}, \end{aligned} \quad [3.60]$$

and $\theta(\omega)$ is a frequency-dependent phase correction function that contains one or more parameters that are adjustable to minimize the phase error in the spectrum. In most processing software, $\theta(\omega) = \theta_0 + \theta_1(\omega - \omega_{\mathrm{pivot}})/(2\pi\ \mathrm{SW})$ is a linear function of frequency, in which θ_0 is called the zero-order phase correction, θ_1 is called the first-order phase correction, and ω_{pivot} is called the pivot frequency. The zero-order phase correction is frequency independent, while the first-order phase correction contributes to a linearly frequency-dependent phase. The frequency-dependent phase correction is zero at ω_{pivot} and has values of $-\theta_1\ [1/2 + \omega_{\mathrm{pivot}}/(2\pi\ \mathrm{SW})]$ and $\theta_1\ [1/2 - \omega_{\mathrm{pivot}}/(2\pi\ SW)]$ at the two edges of the spectrum; thus, the total difference in phase correction from one edge of the spectrum to the other is θ_1. On modern NMR spectrometers, phasing is performed interactively by adjusting θ_0 and θ_1 until the lineshapes in the real part of the spectrum are absorptive. An example of the use of zero- and first-order phase corrections is given in Fig. 3.12.

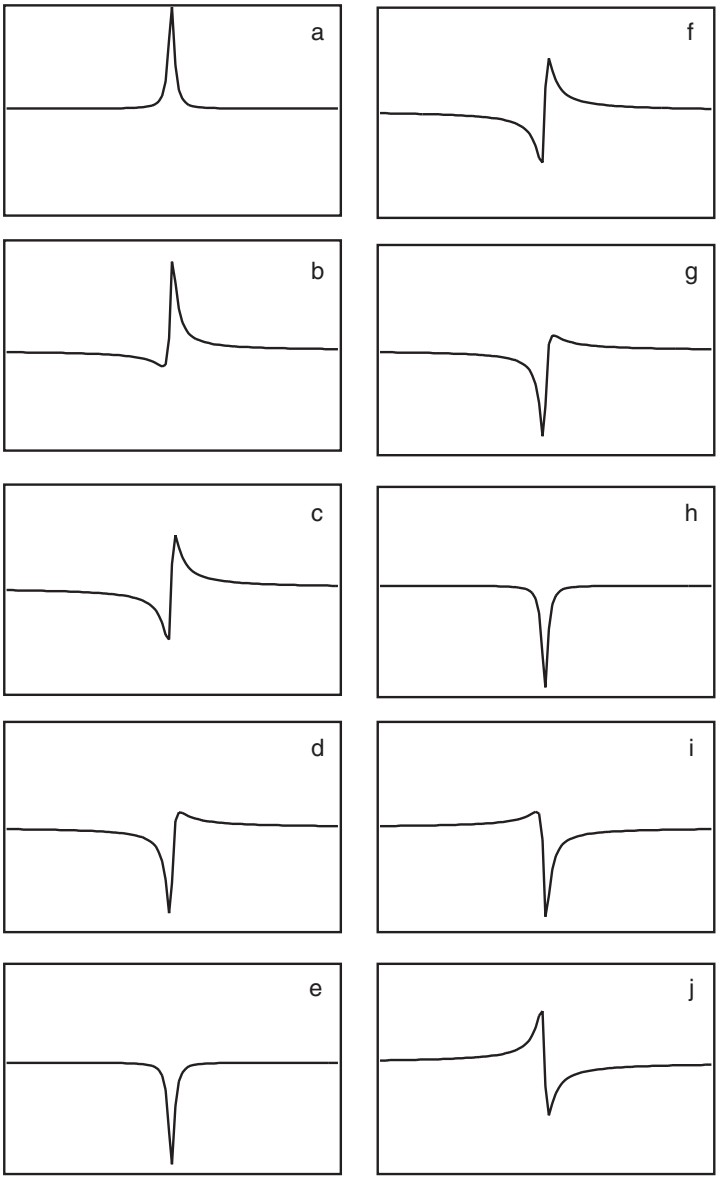

FIGURE 3.11 Phase dependence of lineshapes. Real (a–e) and imaginary (f–j) Lorentzian lineshapes are shown for phases of (a, f) 0°, (b, g) 45°, (c, h) 90°, (d, i) 135°, and (e, j) 180°.

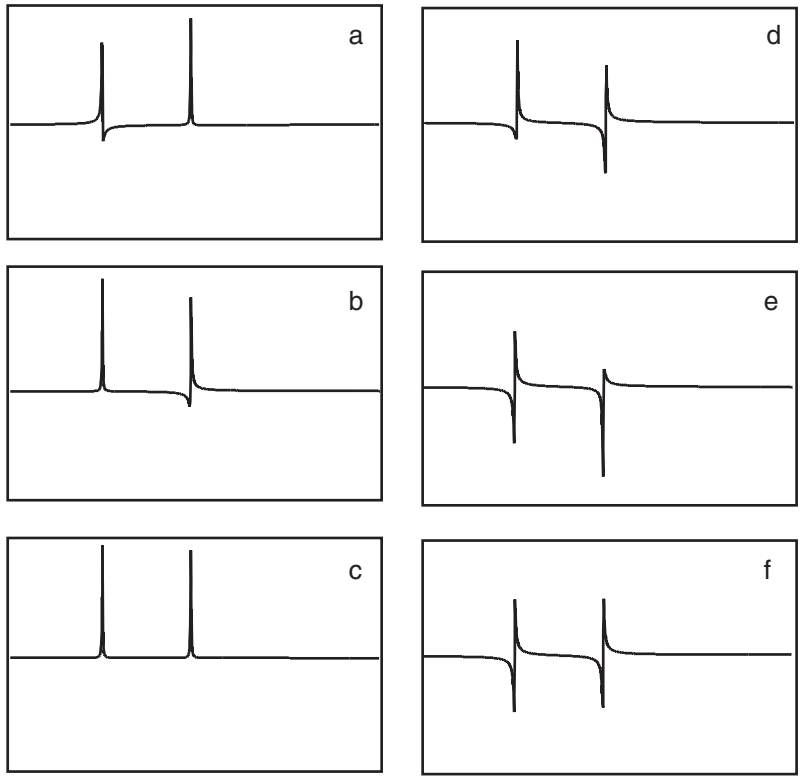

FIGURE 3.12 Phase corrections. Real (a–c) and imaginary (d–f) components of two signals of differing phase are shown. (a, d) The upfield resonance has been phased using a zero-order phase correction; however the downfield resonance has a phase error. (b, e) The downfield resonance has been phased using a zero-order phase correction; however, the upfield resonance has a phase error. (c, f) Both signals have been phased simultaneously by applying zero- and first-order phase corrections.

More detailed analyses of the discrete Fourier transform [3.34] indicate that the baseline of the frequency-domain spectrum displays a nonzero offset and curvature unless the initial signal phase is adjusted to be a multiple of $\pi/2$ and the sampling delay is adjusted such that $t_0 = 0$, $1/(2\mathrm{SW})$ or $1/\mathrm{SW}$ (*21, 22*). For example, if $\phi_0 = 0$ and $t_0 = 0$, and assuming $N\Delta t\lambda 0 \gg 1$, then [3.34] becomes

$$S(\omega_k) = I_0 \frac{1}{1 - \exp[\Delta t(i\omega_0 - i\omega_k - \lambda_0)]}. \qquad [3.61]$$

The exponential function can be expanded to second order to yield:

$$\begin{aligned} S(\omega_k) &\approx -I_0 \frac{1}{\Delta t(i\omega_0 - i\omega_k - \lambda_0) + \Delta t^2(i\omega_0 - i\omega_k - \lambda_0)^2/2} \\ &\approx -I_0 \frac{1}{\Delta t(i\omega_0 - i\omega_k - \lambda_0)[1 + \Delta t(i\omega_0 - i\omega_k - \lambda_0)/2]} \\ &\approx -I_0 \frac{1}{\Delta t(i\omega_0 - i\omega_k - \lambda_0)}[1 - \Delta t(i\omega_0 - i\omega_k - \lambda_0)/2] \\ &\approx \frac{-I_0}{\Delta t} \frac{1}{(i\omega_0 - i\omega_k - \lambda_0)} + \frac{I_0}{2}. \end{aligned} \quad [3.62]$$

Within a constant of proportionality, the first term is identical to the desired Lorentzian lineshape, given by [3.28]. However, the second term contributes a baseline offset that depends on the initial signal intensity, I_0. This offset is eliminated by multiplying the first point of the FID by a factor of 1/2.

As a second important example, if $\phi_0 = 0$ and $t_0 = 1/(2\mathrm{SW}) = \Delta t/2$, and assuming $N\Delta t\lambda_0 \gg 1$, then [3.34] becomes

$$S(\omega_k) = I_0 \frac{\exp[(i\omega_0 - \lambda_0)\Delta t/2]}{1 - \exp[\Delta t(i\omega_0 - i\omega_k - \lambda_0)]}. \quad [3.63]$$

The spectrum described by this expression contains a linear first-order phase error that can be corrected by multiplying by the complex phase factor $\exp(-i\omega_k\Delta t/2)$ to yield

$$\begin{aligned} S(\omega_k) &= I_0 \frac{\exp[(i\omega_0 - i\omega_k - \lambda_0)\Delta t/2]}{1 - \exp[\Delta t(i\omega_0 - i\omega_k - \lambda_0)]} \\ &= -I_0 \frac{1}{2\sinh[(i\omega_0 - i\omega_k - \lambda_0)\Delta t/2]} \\ &\approx \frac{-I_0}{\Delta t} \frac{1}{(i\omega_0 - i\omega_k - \lambda_0)}. \end{aligned} \quad [3.64]$$

The last line of this expression is obtained by expanding $\sinh(x)$ to second order. Within a constant of proportionality, the first term is identical to the desired Lorentzian lineshape, given by [3.28]. The necessary zero- and first-order phase corrections are given by

$$\theta_1 = -2\theta_0 = -360^\circ \qquad t_0\,\mathrm{SW} = -180^\circ, \quad [3.65]$$

in which the pivot is assumed to be set at the downfield edge of the spectrum (*22*). Unlike [3.62], no adjustment of intensity of the first point

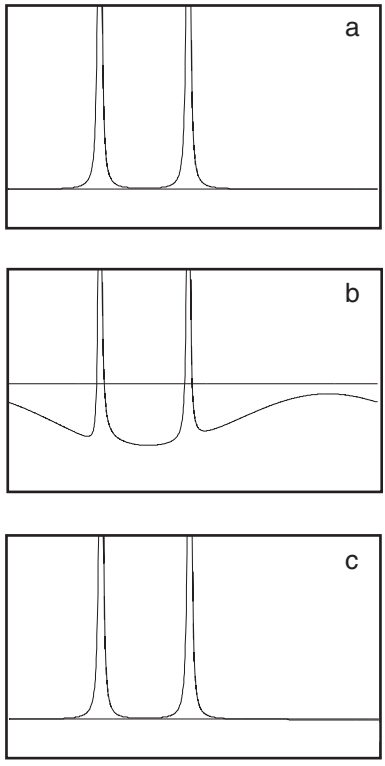

FIGURE 3.13 Baseline distortions from phase corrections. (a) An FID recorded with an initial sampling delay of zero generates a properly phased spectrum without baseline distortions. (b) An FID recorded with an arbitrary nonzero initial sampling delay generates a spectrum with baseline distortions after phase correction. (c) An FID recorded with an initial sampling delay adjusted to one-half of the sampling time generates a spectrum without baseline distortions after phase correction.

of the FID is necessary. An example of the baseline distortions observed if the signal phase is not correctly adjusted is given in Fig. 3.13.

In some cases, baseline distortions may be present even if sampling delays are properly taken into account. These distortions result from corruption of the first few points in the FID. If the receiver gain is set too high, then the magnitude of the analog signal being detected may exceed the dynamic range of the ADC or earlier stages of the signal amplifiers. Invariably, points at the beginning of the FID are affected and all appear with the same maximum value in the ADC. The FID is then said to be

"clipped." Fourier transformation of the FID is essentially the Fourier transformation of the superposition of the uncorrupted FID and a square function. The resulting frequency-domain spectrum exhibits "sinc-wiggles," or truncation artifacts. The second problem, which is referred to as "baseline roll," arises from the transient response of the audio filters to the incoming signal (*12*). The digitized signal is the superposition of the uncorrupted FID and a set of points corresponding to the transient response of the filters. In practice, only the first few points of the FID are affected by clipping or transient filter response. An error or distortion in the first sampled point of the FID gives rise to a constant baseline offset in the frequency-domain spectrum. Distortions in the second and subsequent points give rise to increasingly severe baseline effects. For example, distortion of the second point causes curvature in the baseline. Distortion of the third point results in a baseline with one node and two antinodes that resemble the superposition of the spectrum and a sine wave. Examples of these baseline distortions are shown in Fig. 3.14. Sizable reduction in baseline roll can be achieved by adjusting the time between the observed pulse and the start of sampling so that sampling occurs close the crossing point of the

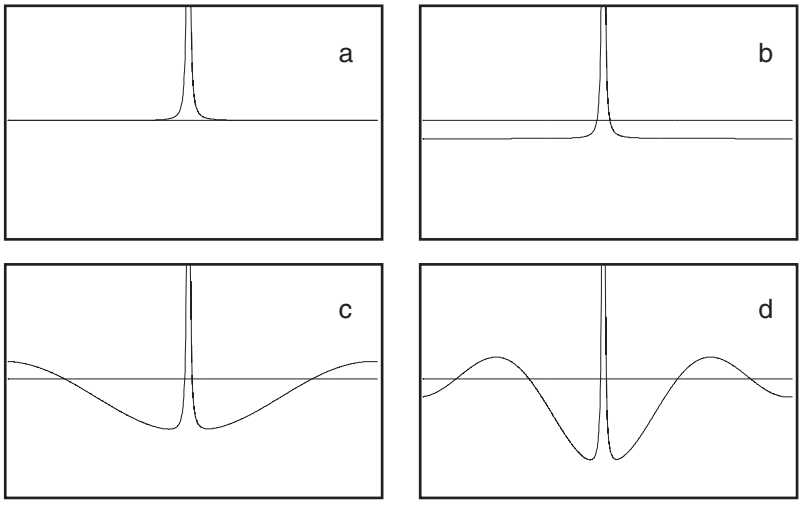

FIGURE 3.14 Baseline distortions from a corrupt FID. (a) An uncorrupted FID generates a spectrum without baseline distortion. Baseline distortions are observed if the (b) first point of the FID, (c) first two points of the FID, and (c) first three points of the FID are corrupted. For this figure, corrupted time-domain data points were set identically to zero.

filter ringing pattern (*12*). The use of a so-called Hahn echo pulse sequence (Section 3.6.4.2) can alleviate many baseline distortions in ^{1}H-detected NMR spectroscopy. Linear prediction algorithms also can be used to correct the first few points of the FID to eliminate baseline distortions (Section 3.3.4).

3.3.3 SIGNAL-TO-NOISE RATIO

The frequency difference between adjacent points in the frequency-domain spectrum following discrete Fourier transformation is $\Delta\nu = 1/(N\Delta t) = 1/t_{\max}$. The digital resolution in the final spectrum depends on the total acquisition time, and not on the sampling interval. Increasing the resolution in a spectrum requires that $t_{\max}$ be increased either by recording additional data points or by increasing Δt. Increasing Δt has the effect of reducing the spectral width, which may not be feasible. Increasing $t_{\max}$ is productive only if the signals of interest have sufficiently long T_2 values. Once the signals have decayed to zero, increasing $t_{\max}$ increases the noise in the spectrum without increasing the resolution between resonance signals.

NMR spectroscopy is an insensitive technique and optimization of the signal-to-noise ratio has long been of concern. The initial impetus for the development of pulsed Fourier transform NMR spectroscopy was its increased sensitivity. For a simple one-pulse experiment, the sensitivity, defined as the signal-to-noise ratio per unit acquisition time, is given by (*10*)

$$\mathscr{S} = \frac{\langle s \cdot h \rangle}{\langle h^2 \rangle^{1/2}} \left(\frac{t_{\max}}{T_c} \right)^{1/2} \frac{1}{\rho}, \qquad [3.66]$$

in which

$$\langle s \cdot h \rangle = \frac{I_0}{t_{\max}} \int_0^{t_{\max}} s_e(t) h(t)\, dt,$$

$$\langle h^2 \rangle = \frac{1}{t_{\max}} \int_0^{t_{\max}} h^2(t)\, dt, \qquad [3.67]$$

where T_c is the total time between acquisitions (acquisition time plus the recycle delay), I_0 is the initial value of the signal, $h(t)$ is the apodization function, and ρ is the square root of the noise power spectral density. As indicated by [3.66], the sensitivity depends on the ratio of the average

weighted signal amplitude and the root-mean-square amplitude of the apodization function. If $h(t)$ is chosen to be equal to the envelope function $s_e(t)$ (see matched filtering in Section 3.3.2.2), then,

$$\mathscr{S} = I_0\left\langle s_e^2\right\rangle^{1/2}(t_{max}/T_c)^{1/2}1/\rho. \qquad [3.68]$$

Optimal sensitivity depends, therefore, upon the root-mean-square amplitude of the resonance signal. Because $I_0 \propto N_s$, and $\rho \propto N_s^{1/2}$, in which N_s is the number of transients that are signal averaged, $\mathscr{S} \propto N_s^{1/2}$. More detailed analyses of the determinants of I_0 and ρ yield the result that (*23*),

$$\mathscr{S} \propto NQ\gamma^{5/2}B_0^{3/2}T_2^{1/2}T^{-3/2}(t_{max}/T_c)^{1/2}, \qquad [3.69]$$

in which N is the number of nuclear spins, T is the temperature, and Q is the quality factor of the probe coil. Not surprisingly, the greatest sensitivity is obtained for nuclei with large values for γ and long T_2 relaxation times.

3.3.4 ALTERNATIVES TO FOURIER TRANSFORMATION

The Fourier transformation is fast, numerically stable, and produces phase-sensitive frequency-domain spectra in a convenient representation. Nonetheless, the Fourier transformation is not without disadvantages; principally, for short data records, the resolution in the frequency-domain spectrum is reduced and truncation artifacts can become large (unless strong window functions are applied, which correspondingly reduces the resolution in the spectrum). As discussed in Chapter 4, the time required to acquire a multidimensional NMR data set is proportional to the number of points acquired in the indirectly detected dimensions. Therefore, data records in the indirectly detected dimensions are almost always truncated, and in the case of three- and four-dimensional data sets, severely so. Accordingly, extensive efforts have been made to develop alternative methods of producing frequency-domain spectra from truncated time-domain interferograms that are more satisfactory than is Fourier transformation. The various methods proposed include linear prediction (*24*), maximum entropy reconstruction (*25*), maximum likelihood (*26*) and Bayesian analysis (*27*); of these, linear prediction and maximum entropy reconstruction are the most frequently utilized. The review by Stephenson provides a detailed

introduction to both linear prediction and maximum entropy methods in NMR spectroscopy (*28*).

3.3.4.1 Linear Prediction Linear prediction algorithms model the time-domain signal (the interferogram) as (*13*)

$$s(k\Delta t) = -\sum_{m=1}^{M} a_m s([k-m]\Delta t) + \varepsilon_m, \qquad [3.70]$$

in which M is the *prediction order* or the number of signal *poles*, ε_m is the prediction error (distinct from the random noise), a_m is the mth linear prediction coefficient, and $k = 0, \ldots, N-1$. In essence, the kth data point is modeled as a linear function of the previous M points. Although [3.70] could be postulated as a description of an arbitrary signal, a close connection exists between [3.70] and the damped sinusoidal signal [3.27]. Linear prediction algorithms attempt to find the set of coefficients a_m that minimizes, in the least-squares sense, the prediction error. Once the linear prediction coefficients have been determined, the frequency domain spectrum can be calculated directly from the prediction coefficients or, more commonly, the linear prediction results can be used to calculate an extension to the interferogram prior to conventional processing by Fourier transformation. Linear prediction algorithms can predict the future behavior of a sinusoid over many periods; in contrast, polynomial expansions frequently fail to extend a sinusoid for more than a period accurately.

Implicit in the formulation of the linear prediction method are a number of important issues:

1. The maximum number of resonance signals that can be modeled is given by the prediction order
2. Linear prediction algorithms generally require $M \leq N/2$.
3. The optimal prediction order is difficult to determine rigorously.
4. Random noise is not incorporated into the linear prediction model. As a consequence, linear prediction methods generally work best for data with relatively high signal-to-noise ratios.
5. The FID usually cannot be extended by more than a factor of two without severely distorting the signal lineshapes.
6. Two- (and higher) dimensional data sets are processed by linearly predicting each (t_1, ω_2) interferogram independently. Differences in numerical results from interferogram to interferogram can distort two-dimensional lineshapes.

The most common use for linear prediction methods is to extend the time-domain data for ^{13}C and ^{15}N resonance signals detected during indirect evolution periods of multidimensional NMR experiments. If all ^{1}H dimensions are Fourier transformed first, then the heteronuclear dimensions generally contain relatively few signals in each interferogram, which simplifies the linear prediction problem.

In some experimental situations, notably constant-time experiments or extremely truncated data, the signal interferogram is undamped by relaxation (limited damping by inhomogeneity broadening can be corrected by multiplication with an increasing exponential). If the phase has been properly adjusted by adjusting the initial value of the evolution period to 0 or 1/(2SW) (Section 3.3.2.3), then the complex signal satisfies the relationship $s(-t) = s^*(t)$, in which the asterisk indicates complex conjugation. This relationship can be used to generate a data sequence of length $2N$ from a sequence of length N in which the data points extend from $-N, -N+1, \ldots, N-1, N$ (if the initial value of t is 0, then the extended sequence contains $2N-1$ points). The longer data sequence can be used as the input for linear prediction, after which the points from $-N$ to -1 are discarded. This technique has been called *mirror image* linear prediction and frequently allows higher resolution estimates of the frequency-domain spectrum to be obtained (*29*).

At the present time, the algorithms based on singular value decomposition, such as the linear predictive and hyperbolic singular value decomposition (LPSVD and HSVD) algorithms, appear to be the most robust (*30*). An example in which the HSVD algorithm was used to linear predict the t_1 interferograms in a two-dimensional constant-time ^{1}H–^{13}C HSQC spectrum of ubiquitin (Chapter 7, Section 7.1.3.1) is shown in Figs. 3.15 and 3.16.

Linear prediction also can be used to correct the magnitude of incorrectly sampled points (for example, the initial points of the FID may be corrupted by pulse breakthrough and filter response; see Section 3.3.2.3). For these applications, computationally less demanding algorithms, such as the Burg or Levinson–Durbin methods, are satisfactory (*28, 31*).

3.3.4.2 Maximum Entropy Reconstruction Maximum entropy methods reconstruct the frequency-domain NMR spectrum directly (no subsequent Fourier transformation is necessary) by determining the spectrum $S[k/(N\Delta t)]$ for $k = 0, 1, \ldots, N-1$ that maximizes the entropy

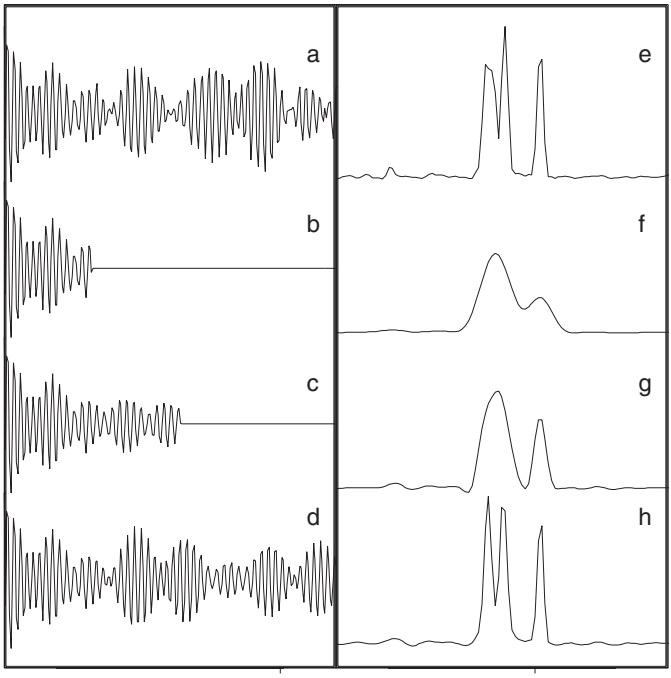

FIGURE 3.15 Linear prediction using the HSVD algorithm. A constant-time ^{1}H–^{13}C HSQC spectrum of ubiquitin was linear predicted in the t_1 (^{13}C) dimension following conventional processing in the acquisition dimension. The t_1 interferogram at an F_2 (^{1}H) shift of 4.52 ppm was used for illustration. Shown are the (a) complete 240-point interferogram, (b) truncated 64-point interferogram, (c) truncated interferogram extended to 128 points by HSVD linear prediction, and (d) truncated interferogram extended to 240 points by mirror-image HSVD linear prediction. The spectra obtained by Fourier transformation of interferograms (a)–(d) are shown in (e)–(h).

function

$$\mathscr{W} = \sum_{k=0}^{N-1} S[k/(N\Delta t)] \ln S[k/(N\Delta t)] \qquad [3.71]$$

subject to the constraint

$$\mathscr{C} = \sum_{j=0}^{M-1} [s(j\Delta t) - \hat{s}(j\Delta t)]^2/\sigma_j^2 = M, \qquad [3.72]$$

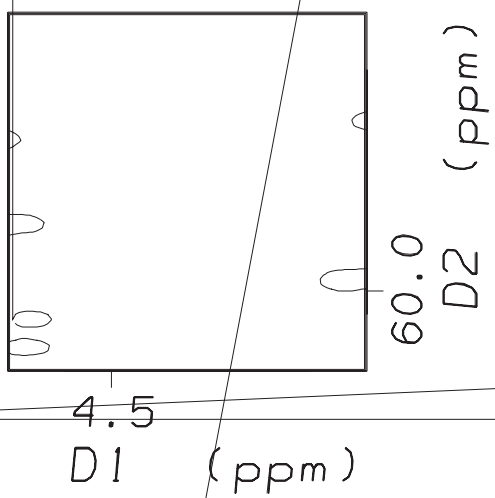

in which M is the number of experimental time domain points, $s(j\Delta t)$ is the jth experimental time domain point, $\hat{s}(j\Delta t) = \mathscr{F}^{-1}\{S[k/(N\Delta t)]\}$ is the inverse Fourier transform of the reconstructed spectrum, and σ_j is the experimental noise level in the time domain data. The entropy and constraint equations can be combined into a single objective or cost

function,

$$\mathcal{V} = \mathcal{W} + \lambda \mathcal{C}, \qquad [3.73]$$

in which λ is a Lagrange multiplier. The objective function is maximized by iteratively refining an initial guess for $S[k/(N\Delta t)]$ using standard numerical algorithms.

In essence, maximum entropy reconstruction amounts to the following prescription: from the (possibly infinite) set of candidate frequency-domain spectra whose time-domain interferograms reproduce the experimental interferogram within experimental uncertainty as described by the constraint function [3.72], select the single spectrum for which the entropy defined by [3.71] is a maximum. The preceding formulations have a number of important corollaries:

1. Unlike linear prediction algorithms, the functional forms of the NMR signals (damped sinusoids) are not assumed *a priori* by the maximum entropy methods; however, experimental uncertainty is considered explicitly by maximum entropy algorithms.
2. The spectral estimates are constrained to be positive by [3.71]. Negative intensity in NMR spectra is treated by representing the spectrum as

$$S[k/(N\Delta t)] = S^{+}[k/(N\Delta t)] - S^{-}[k/(N\Delta t)], \qquad [3.74]$$

   in which $S^{+}[k/(N\Delta t)]$ and $S^{-}[k/(N\Delta t)]$ represent subspectra with positive and negative intensities (*32*).
3. Because M can be less than N, a high-resolution frequency-domain spectrum can be calculated from a limited number of data points.
4. Maximum entropy reconstruction can be performed for multi-dimensional data in straightforward fashion by generalizing [3.71] and [3.72] to include multiple summations (one summation for each dimension).
5. Justification of the use of [3.71] for NMR spectroscopy is not straightforward. Laue et al. discuss the rationale for using [3.73] in spectral reconstruction (*33*).

Maximum entropy reconstruction of the truncated t_1 interferograms in a two dimensional constant-time ^{1}H–^{13}C HSQC spectrum of ubiquitin (Chapter 7, Section 7.1.3.1) is shown in Fig. 3.17. Examination of Figures 3.15–3.17 demonstrate that for severely truncated data, both linear prediction and maximum entropy reconstruction can improve the resolution of the frequency-domain spectrum compared with Fourier

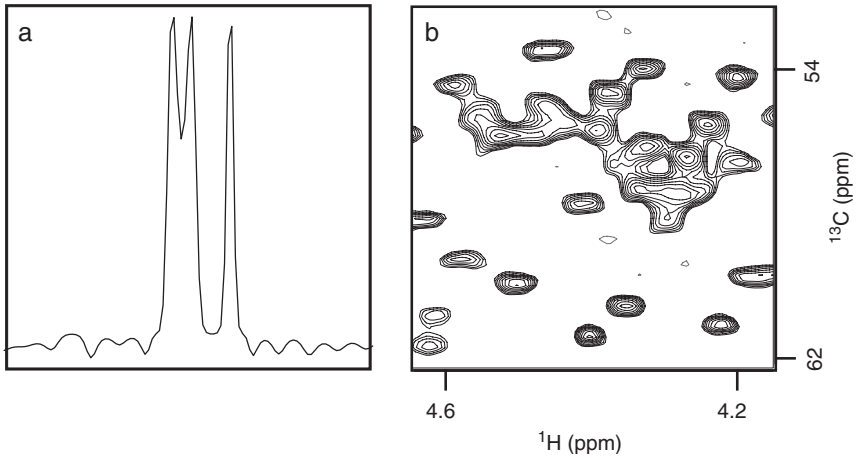

FIGURE 3.17 Maximum entropy reconstruction of an HSQC spectrum. A constant-time ^{1}H–^{13}C HSQC spectrum of ubiquitin was processed by maximum entropy reconstruction in the t_1 (^{13}C) dimension following conventional processing in the acquisition dimension. Reconstruction was based on 64 t_1 points. Shown are (a) a one-dimensional slice at an F_2 shift of 4.52 ppm and (b) the same region of the two-dimensional spectrum shown in Fig. 3.16.

transformation. In neither case are the resulting spectra as highly resolved and distortion-free as is the spectrum obtained by Fourier transformation of the untruncated interferogram.

3.4 Pulse Techniques

Achieving optimal results for NMR spectroscopy of large complex macromolecules requires careful attention to experimental details. An extensive set of techniques has been developed in NMR spectroscopy to compensate for the deficiencies of simple rf pulses and to manipulate spin systems in particular ways. A number of these techniques are described in the following sections.

3.4.1 OFF-RESONANCE EFFECTS

In practical situations, the nuclei in a molecule will possess a range of chemical shifts. Because an rf pulse can be applied at only one frequency (the transmitter frequency, ω_{rf}), some nuclei will have

resonant frequencies that are close to ω_{rf} while other nuclei will have resonant frequencies that are very different from ω_{rf}. Consequently, all nuclei cannot be expected to respond to the effect of an rf pulse in an ideal fashion. Those nuclei on-resonance with the pulse will respond ideally; other nuclei, near resonance with $\omega_0 \approx \omega_{rf}$, will precess around an effective field, B^r, that will be similar to that of B_1. Further and further *off resonance*, where $\omega_0 \neq \omega_{rf}$ and the magnitude of the offset Ω increases, the effective field, B^r, will be very different from B_1. In many cases, the offset of some nuclei may be comparable to the strength of the pulse measured in frequency units ($\omega_1 = -\gamma B_1$). In these circumstances, the effective field is tilted away from the x–y plane toward the z-axis (see Fig. 1.2).

For the off-resonance case, a pulse of y-phase applied to equilibrium z-magnetization yields ([1.34])

$$\begin{aligned} M_x &= M_0 \sin\alpha \sin\theta, \\ M_y &= M_0(1 - \cos\alpha)\sin\theta \cos\theta, \\ M_z &= M_0(\cos^2\theta + \cos\alpha \sin^2\theta), \end{aligned} \qquad [3.75]$$

in which α and θ are defined by [1.23] and [1.21]. In practical terms, two effects must be noted that yield both phase and intensity anomalies for resonance lines that have large offsets from the transmitter frequency. The phase anomalies can be described in terms of a phase shift, β, where

$$\tan\beta = \frac{M_y}{M_x} = \frac{(1 - \cos\alpha)\cos\theta}{\sin\alpha}. \qquad [3.76]$$

Using [1.21],

$$\tan\beta = \frac{(1 - \cos\alpha)\sin\theta}{\sin\alpha} \cdot \frac{\Omega}{\omega_1}. \qquad [3.77]$$

This equation is a convenient form in which to view the phase problems that arise because the dependence on resonance offset is indicated directly. The amplitude of the resonance signal also changes with offset as given by

$$M_{x,y} = \sqrt{M_x^2 + M_y^2}. \qquad [3.78]$$

The magnetization, phase angle, and effective rotation angle for an off-resonance 90° pulse are illustrated in Fig. 3.18; the resulting

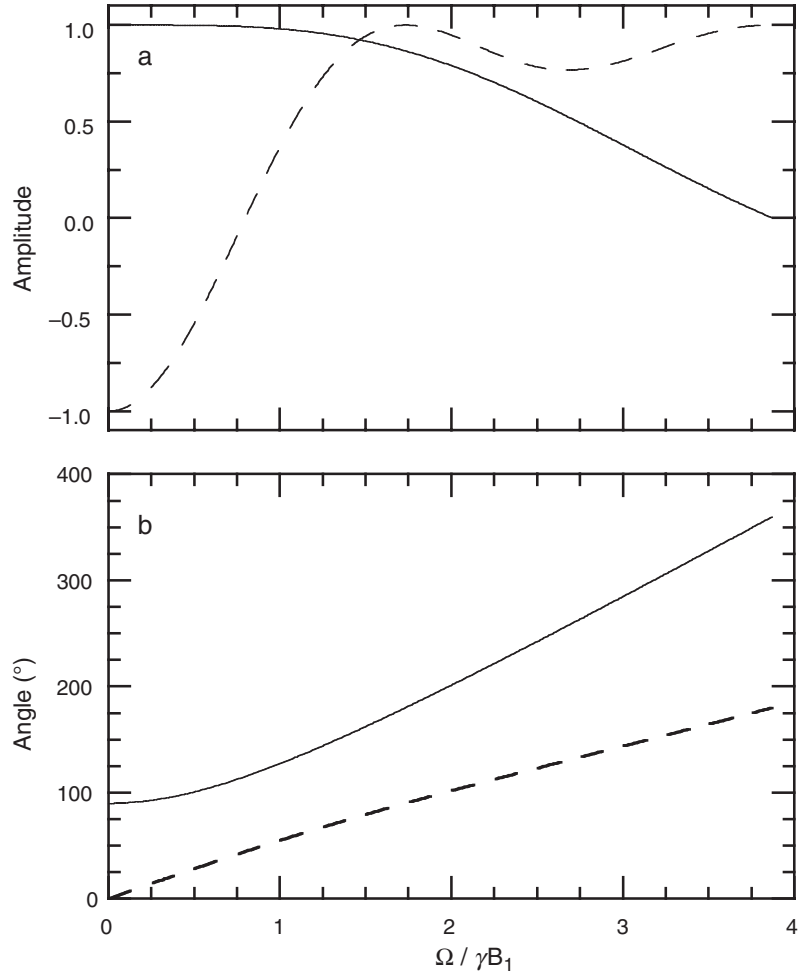

FIGURE 3.18 Off-resonance effects for 90° and 180° pulses. (a) Shown are (—) the magnitude of the transverse magnetization, $M_{x,y} = (M_x^2 + M_y^2)^{1/2}$, following a nominal 90° pulse and (- - -) the M_z magnetization following a nominal 180° pulse. (b) Shown are the (—) effective rotation angle and (- - -) phase of the transverse magnetization following a nominal 90° pulse.

lineshapes are shown in Fig. 3.19. As the offset, Ω, increases, the amplitude of the transverse magnetization remains approximately constant and the phase of the transverse magnetization increases linearly until the offset equals the rf field strength, $\Omega = \omega_1$. At larger offsets,

the signal amplitude decreases until it disappears. At this point, the bulk magnetization vector rotates about the effective field such that it is aligned along the z-axis once more at the end of the pulse. At even larger offsets, the signal amplitude oscillates from positive to negative and the magnitude of the signal decreases.

For offsets $\Omega \leq \omega_1$, nearly ideal results are obtained for a 90° pulse if the linear phase dependence is compensated. Expanding [3.77] in Taylor series about $\Omega = 0$ yields

$$\beta = \Omega/\omega_1 = \tau_{90}/(\omega_1 \tau_{90}) = 2\tau_{90}\Omega/\pi, \qquad [3.79]$$

in which τ_{90} is the length of the on-resonance 90° pulse. Thus, an off-resonance 90° pulse can be treated as an ideal pulse followed by an evolution period given by

$$\tau_{\text{corr}} = 2\tau_{90}/\pi. \qquad [3.80]$$

An alternative derivation of this result begins with [2.120]. For $\Omega > 0$, $\theta = \pi/2 - \zeta$, where $\tan(\zeta) = \Omega/\omega_1$, and $\alpha = \pi/2 + \varepsilon$, where $\varepsilon = \pi(1 - \sin\theta)/(2\sin\theta)$. Using these expressions, the propagator for an

off-resonance pulse with x-phase is

$$\begin{aligned}\mathbf{R}_x(\alpha,\theta) &= \mathbf{R}_y(\theta)\mathbf{R}_z(\alpha)\mathbf{R}_y^{-1}(\theta)\\ &= \mathbf{R}_y(-\zeta)\mathbf{R}_y(\pi/2)\mathbf{R}_z(\pi/2)\mathbf{R}_z(\varepsilon)\mathbf{R}_y^{-1}(\pi/2)\mathbf{R}_y^{-1}(-\zeta)\\ &= \mathbf{R}_y(-\zeta)\mathbf{R}_x(\pi/2)\mathbf{R}_x(\varepsilon)\mathbf{R}_y^{-1}(-\zeta)\\ &= \mathbf{R}_x(\pi/2)\mathbf{R}_z(\zeta)\mathbf{R}_x(\varepsilon)\mathbf{R}_y^{-1}(-\zeta),\end{aligned} \quad [3.81]$$

and the identity [2.121] has been used. If ζ and ε are small, which will be the case if Ω is not too large, then the rotation operators that depend on these values commute with each other. Thus, the order of the operators [3.81] can be rearranged to yield

$$\begin{aligned}\mathbf{R}_x(\alpha,\theta) &= \mathbf{R}_x(\pi/2)\mathbf{R}_z(\zeta)\mathbf{R}_x(\varepsilon)\mathbf{R}_y^{-1}(-\zeta)\\ &\approx \mathbf{R}_x(\pi/2)\mathbf{R}_y^{-1}(-\zeta)\mathbf{R}_x(\varepsilon)\mathbf{R}_z(\zeta)\\ &\approx \mathbf{R}_z(\zeta)\mathbf{R}_x(\pi/2)\mathbf{R}_x(\varepsilon)\mathbf{R}_z(\zeta)\\ &\approx \mathbf{R}_z(\zeta)\mathbf{R}_x(\alpha)\mathbf{R}_z(\zeta).\end{aligned} \quad [3.82]$$

The off-resonance pulse is approximately described as an on-resonance pulse with x-phase and rotation angle α (which will be denoted α_x) preceded and followed by a z-rotation with an angle ζ. The rotation angle $\zeta \approx \Omega/\omega_1 = 2\Omega\tau_{90}/\pi = \tau_{\text{corr}}$. This analysis yields a slightly more general result: the off-resonance pulse is approximated by the sequence τ_{corr}–α_x–τ_{corr}. The magnitude of the z-rotation is seen to be identical to the angular deviation between the effective field and the x-axis.

In contrast, Fig. 3.18 demonstrates that a 180° inversion pulse has a highly nonideal off-resonance excitation profile. Magnetization will not be fully inverted, and a notable amount of transverse magnetization will be generated. Because nonideal effects of 180° pulses cause significant problems in NMR spectra, considerable effort has been devoted to improving the performance of 180° pulses by use of EXORCYCLE phase cycles (Chapter 4, Section 4.3.2.3), composite pulses (Section 3.4.2), and static magnetic field gradients (Chapter 4, Section 4.3.3.2).

The property of being able to create a null in the frequency excitation profile of a pulse can be used to advantage in many experiments, including water suppression methods and in some multidimensional NMR experiments. In some instances one set of spins must be excited while leaving others unperturbed. Using [3.75], a null in the excitation profile for a pulse with on-resonance rotation angle $\alpha = 90°$ is

achieved at an offset from resonance equal to

$$\Omega = \pm\sqrt{15}\omega_1. \quad [3.83]$$

For a 180° pulse, a null is achieved when

$$\Omega = \pm\sqrt{3}\omega_1. \quad [3.84]$$

Significant off-resonance effects can be observed even for nonresonant spins with $\Omega \gg \omega_1$ if rf pulses are applied to coherent states of the density operator, as opposed to thermal equilibrium magnetization. Off-resonance effects can lead to phase errors and frequency shifts in multidimensional NMR experiments, particularly when long, low-amplitude continuous or shaped rf pulses are employed. Off-resonance, or nonresonant, effects, are commonly called Bloch–Siegert shifts. The phrase "Bloch–Siegert shifts" of the second kind is used to distinguish these effects from Bloch–Siegert shifts (of the first kind) arising from the counter-rotating component of the rf field [1.15] (*34*). The phase shift of transverse magnetization during an off-resonance pulse train arises from a z-rotation and is given by (*35, 36*)

$$\theta_{NR} = \langle\omega_1(t)^2\rangle\tau_p/(2\Omega), \quad [3.85]$$

in which the angle brackets represent an average over the pulse train. If τ_p is not a constant, but varies with the evolution period of a multidimensional NMR experiment, then the off-resonance effect is manifested as a frequency shift, ω_{NR}, given by

$$\omega_{NR} = \langle\omega_1(t)^2\rangle/(2\Omega). \quad [3.86]$$

In addition to the nonresonant phase shift, a rotation occurs about the axis along which the rf field is applied and is given by

$$\zeta_{NR} = \theta_{NR}\langle\omega_1(t)\rangle/\Omega. \quad [3.87]$$

The nonresonant rotation is smaller than the phase shift by a factor of at least ω_1/Ω and is eliminated for amplitude- or phase-modulated pulse trains with a net rotation angle of zero [$\langle\omega_1(t)\rangle = 0$], such as decoupling sequences.

Nonresonant effects are common when performing frequency-selective homonuclear decoupling. For example, ^{13}CO and $^{13}C^{\alpha}$ spins can be decoupled by applying a selective 180° pulse to the ^{13}CO or C^{α} spins at the midpoint of the desired evolution period or by applying a frequency-selective decoupling sequence, such as SEDUCE-1, during the

evolution period. These techniques will be illustrated for a $t_1/2$–180°(CO)–$t_1/2$ evolution period for $^{13}C^{\alpha}$ magnetization.

For a weak rectangular 180° pulse applied on-resonance with the ^{13}CO spins, $\langle\omega_1(t)^2\rangle = \omega_1^2$ and the nonresonant phase shift of the aliphatic spins is given by [3.85]

$$\theta_{NR} = \omega_1^2\tau_p/(-2\Omega_\alpha) = -\pi\omega_1/(2\Omega_\alpha) = -\pi/(2\sqrt{3}) = -52^\circ, \qquad [3.88]$$

in which $\omega_1 = \Omega_\alpha/3^{1/2}$, Ω_α is the frequency difference between ^{13}CO and $^{13}C^{\alpha}$ spins [3.84], and the last equality obtains for $\Omega = \Omega_\alpha$. In this special case, the exact nonresonant phase shift can be calculated directly. Transverse $^{13}C^{\alpha}$ magnetization rotates by 2π around the effective field during the off-resonance pulse. Consequently, transverse magnetization does not acquire any additional phase during the τ_p duration of the pulse. If however, the pulse were applied with zero amplitude, transverse magnetization would simply precess around the z-axis and acquire a phase shift $-\Omega_\alpha\tau_p$. The difference between the two results is (*37*)

$$\theta_{NR} = \Omega_\alpha\tau_p = \Omega_\alpha\pi/\omega_1 = \sqrt{3}\pi = -48^\circ. \qquad [3.89]$$

The slight difference between [3.88] and [3.89] arises because the condition [3.84] only minimally satisfies the requirement $\Omega \gg \omega_1$ used to derive [3.85].

Shaped, rather than rectangular, pulses frequently are used in order to further minimize perturbations of the aliphatic ^{13}C spins during the application of 180° pulses to the ^{13}CO spins. A single lobe of the sinc shape most commonly is employed (Section 3.4.4). In this case, the nonresonant phase shift of the aliphatic spins is given by

$$\theta_{NR} = \frac{\langle\omega_1^2(t)\rangle\tau_p}{2(-\Omega_\alpha)} = -\frac{0.4514(\omega_1^{max})^2\tau_p}{2\Omega_\alpha} = -39.8^\circ, \qquad [3.90]$$

in which ω_1^{max} is the peak amplitude of the rf field during the pulse, and the last equality is obtained assuming $\omega_1^{max} = \Omega_\alpha/3^{1/2}$. The sinc pulse has an average field strength $\langle\omega_1(t)\rangle \approx 0.589\omega_1^{max}$; thus, the rf field strength and pulse length of a sinc pulse are calculated by multiplying either the pulse length or the rf field strength of a 180° rectangular pulse by a factor of $1/0.589 = 1.698$.

Four techniques have been proposed for compensating for the consequent nonresonant phase shifts. In the simplest approach, the phase errors are corrected during processing of the acquired spectrum. In the second approach, the phases of the aliphatic ^{13}C pulses subsequent to the evolution period are shifted by θ_{NR} to account for the nonresonant

phase shift of the aliphatic spins. In the third approach, compensatory rf fields are produced by modulating the amplitude of the selective pulse with a cosine function, $\cos(\Omega_\alpha t)$, for $t = 0$ to τ_p (*35*). For a rectangular pulse, the resulting rf field is (assuming x-phase) given by [1.15]

$$\mathbf{B}_{rf}(t) = 2B_1 \cos(\Omega_\alpha t)\cos(\omega_{rf} t)\mathbf{i} = B_1 \cos[(\omega_{rf} + \Omega_\alpha)t]\mathbf{i} + B_1 \cos[(\omega_{rf} - \Omega_\alpha)t]\mathbf{i}, \quad [3.91]$$

in which ω_{rf} is the transmitter frequency of the $^{13}C^\alpha$ spins. Because the cosinusoidal modulation generates two effective rf fields, the amplitude of the B_1 field must be doubled (i.e., $\omega_1 = 2\Omega_\alpha/3^{1/2}$). The component of the field with frequency $\omega_{rf} + \Omega_\alpha$ is resonant with the ^{13}CO spins and generates the 180°(CO) pulse. The component of the field with frequency $\omega_{rf} - \Omega_\alpha$ is not resonant with any spins of interest. The nonresonant phase shifts of the $^{13}C^\alpha$ spins caused by the two field components are equal and opposite; therefore, the net phase shift is zero at the frequency ω_{rf}. Near resonance, the nonlinear off-resonant phase shift [3.85] is converted to a linear phase shift:

$$\theta_{NR} = [\langle \omega_1(t)^2 \rangle \tau_p / \Omega_\alpha^2]\Omega, \quad [3.92]$$

in which Ω is the resonance offset of the $^{13}C^\alpha$ spins.

Because [3.85] depends nonlinearly on the resonance offset, nonresonant phase shifts can be corrected by these three approaches only if the spins of interest resonate in a narrow frequency range near Ω_α. In the fourth approach, compensatory rf pulses are incorporated into the pulse sequence. For example, if the simple $t_1/2$–180°(CO)–$t_1/2$ evolution period is replaced with the sequence

$$t_1/2\text{–}180°(\text{CO})\text{–}t_1/2\text{–}180°(^{13}\text{C})\text{–}\Delta\text{–}180°(\text{CO})\text{–}\Delta, \quad [3.93]$$

in which Δ is a short fixed delay, then the 180°(^{13}C) pulse applied to the aliphatic spins serves to refocus the phase evolution occurring during the two flanking 180°(CO) pulses. This method does not require that the spectral region of interest be narrow and consequently is generally applicable. In addition, the initial sampling delay can be adjusted to zero by setting $t_1(0) = \Delta$ (Section 3.3.2.3).

3.4.2 B_1 INHOMOGENEITY

The *inhomogeneity* of the rf field describes the variation in the amplitude of the B_1 field as a function of position in the sample.

Thus,

$$B_1(\mathbf{r}) = B_1(0) + \Delta B_1(\mathbf{r}), \qquad [3.94]$$

in which $B_1(0)$ is the amplitude of the $\mathbf{B}_1$ field at the center of the sample, and $\Delta B_1(\mathbf{r})$ characterizes the inhomogeneity of the field. The net evolution of the I_z operator during a pulse of length t averaged over the sample volume, V, is given by

$$\begin{aligned}
&I_z \xrightarrow{[-\gamma B_1(\mathbf{r})t]S_y} I_z \int_V \cos(\gamma B_1(\mathbf{r})t)d\mathbf{r}/V + I_x \int_V \sin(\gamma B_1(\mathbf{r})t)d\mathbf{r}/V \\
&= I_z \left\{ \cos(\gamma B_1(0)t) \int_V \cos(\gamma \Delta B_1(\mathbf{r})t)d\mathbf{r} - \sin(\gamma B_1(0)t) \int_V \sin(\gamma \Delta B_1(\mathbf{r})t)d\mathbf{r} \right\} \Big/ V \\
&+ I_x \left\{ \sin(\gamma B_1(0)t) \int_V \cos(\gamma \Delta B_1(\mathbf{r})t)d\mathbf{r} + \cos(\gamma B_1(0)t) \int_V \sin(\gamma \Delta B_1(\mathbf{r})t)d\mathbf{r} \right\} \Big/ V \\
&= \left\{ I_z \cos(\gamma B_1(0)t) + I_x \sin(\gamma B_1(0)t) \right\} \int_V \cos(\gamma \Delta B_1(\mathbf{r})t)d\mathbf{r}/V \\
&- \left\{ I_z \sin(\gamma B_1(0)t) - I_x \cos(\gamma B_1(0)t) \right\} \int_V \sin(\gamma \Delta B_1(\mathbf{r})t)d\mathbf{r}/V. \qquad [3.95]
\end{aligned}$$

Because the cosine and sine functions are oscillatory, the integrals in [3.95] tend to zero, provided that $\Delta B_1(\mathbf{r})$ is nonuniform throughout the sample and t is sufficiently long to ensure that $\gamma \Delta B_1(\mathbf{r})t$ is spatially randomized between 0 and 2π. For modern NMR probes, $|\Delta B_1(\mathbf{r})/B_1(0)| \approx 10$–$20\%$ and significant dephasing of a signal can be achieved in a few milliseconds.

Spin lock purge pulses dephase coherences orthogonal to the rf field (I_y or I_z coherences) while preserving the coherence locked along the rf field (I_x coherence). Purge pulses can be used to eliminate artifacts in NMR spectra arising from undesired operators orthogonal to the operator of interest (see Section 7.2.4.3 for an example). However, product operators containing two spin operators orthogonal to the rf field (e.g., homonuclear $2I_{1z}I_{2z}$ or $2I_{1z}I_{2y}$ operators) contain components that behave as zero-quantum coherences in the tilted rotating reference frame of the rf field (see Sections 5.2.3 and 5.4.3 for additional discussion

of tilted rotating reference frames) and consequently are dephased inefficiently by the inhomogeneous rf field (*38, 39*).

3.4.3 COMPOSITE PULSES

The usual goal of applying an rf pulse to the sample is to achieve a rotation of coherences around a defined axis by a specified angle. The actual performance of an rf pulse can be degraded by any number of factors, including finite rise times of the pulse, amplitude droop during the pulse, phase instability during the pulse, spatial inhomogeneity of the rf field across the sample, resonance offset effects, or relaxation during the pulse. Certain of these effects are minimized by improvements in NMR spectrometer hardware, such as digital frequency synthesis. Some of these effects can be reduced by phase cycling and signal averaging. Other effects can be compensated by replacement of a single rf pulse by an extended pulse train that is designed to achieve the same ideal rotation as the single pulse, but which is more resistant to nonideal influences. These pulse trains are called composite pulses and have been extensively developed for reduction of the effects of rf field inhomogeneity and resonance offset. While composite pulses have been designed to meet a large number of objectives, for multidimensional NMR spectroscopy of biomolecules, three objectives are of the most relevance: 90° rotation of z-magnetization into the transverse plane, inversion of z-magnetization, and refocusing of transverse magnetization. In general, the design of composite pulses that compensate for both rf inhomogeneity and resonance offset effects is more difficult than is the design of composite pulses that compensate for one of the two effects individually. Shorter composite pulse trains generally give less satisfactory compensation; however, long composite pulse trains may be impractical (due to amplifier droop and evolution of the spin system during the extended pulse sequence). The initial state of the magnetization is important to the design of the composite pulse; a composite 180° pulse that produces accurate inversion of z-magnetization may not necessarily produce accurate refocusing of transverse magnetization. The detailed mathematical derivations of composite pulses will not be presented in this section; the interested reader is referred to the comprehensive review by Levitt (*40*). The design of composite pulses is closely related to the design of spin decoupling techniques discussed in Section 3.4.5.

Numerous composite pulses have been developed for effecting 90° and 180° rotations. Composite 180° pulses are utilized in multidimensional NMR spectroscopy much more frequently than are

composite 90° pulses because of the nearly ideal performance of a 90° pulse (Fig. 3.18). The most successful composite pulses are designed to invert z-magnetization and refocus scalar coupling evolution. Composite pulses often do not perform appreciably better than a single 180° pulse for refocusing chemical shift evolution because many composite pulses introduce offset-dependent phase shifts of the refocused coherences that are difficult to compensate in multidimensional NMR experiments (*40*). Early efforts at designing composite pulses relied on some combination of guesswork/insight, average Hamiltonian theory, Fourier analysis, and numerical integration of the Bloch equations. Increasingly, new composite pulse sequences are obtained by computer optimization of initial trial pulse sequences generated by the aforementioned techniques. Calculating the performance of a particular composite pulse is considerably simpler than is designing the pulse sequence. A windowless composite pulse consisting of a series of N consecutive pulses without intervening delays is described by

$$\tilde{P}_{\phi}(\alpha) = \prod_{i=1}^{N} P_{\phi_i}(\alpha_i), \qquad [3.96]$$

in which ϕ_i, and α_i are the pulse phase and nominal (on-resonance) rotation angle of the ith pulse, respectively. The net rotation induced by the composite pulse is given by

$$\mathbf{R}_{\phi}(\alpha) = \prod_{i=1}^{N} \mathbf{R}_z(\phi_i)\mathbf{R}_y(\theta_i)\mathbf{R}_z(\alpha_i)\mathbf{R}_y(-\theta_i)\mathbf{R}_z(-\phi_i), \qquad [3.97]$$

in which ϕ_i, θ_i, and α_i represent the values of the phase, tilt angle, and effective rotation angle for the ith pulse element. The rotation matrices are given by [1.35]. The effective rotation angle and tilt angle are described by [1.23] and [1.21]. The magnetization following the composite pulse is

$$\mathbf{M}(0_+) = \mathbf{R}_{\phi}(\alpha)\mathbf{M}(0_-), \qquad [3.98]$$

in which $\mathbf{M}(0_-)$ and $\mathbf{M}(0_+)$ are the magnetizations before and after the pulse, respectively. Various strategies have been devised to develop composite pulses that have reduced sensitivity to off-resonance effects, but this normally comes at the expense of poorer performance in the presence of rf inhomogeneity. The inverse is also true: composite pulses optimized for tolerance to rf inhomogeneity generally exhibit increased sensitivity to resonance offset.

As an example, product operator calculations indicate that the z-magnetization obtained from a simple, on-resonance pulse of length $2\alpha \approx 180^\circ$ is

$$\begin{aligned} I_z &\xrightarrow{2\alpha_x} -I_y \sin 2\alpha + I_z \cos 2\alpha \\ &= -I_y \sin 2\alpha - I_z(1 - 2\cos^2\alpha). \end{aligned} \quad [3.99]$$

The pulse sequence $\alpha_x(2\alpha)_y\alpha_x$ with $2\alpha \approx 180^\circ$ is a commonly used composite 180° pulse. The evolution of I_z is given by,

$$\begin{aligned} I_z &\xrightarrow{\alpha_x} -I_y \sin\alpha + I_z \cos\alpha \\ &\xrightarrow{2\alpha_y} I_x \cos\alpha \sin 2\alpha - I_y \sin\alpha + I_z \cos\alpha \cos 2\alpha \\ &\xrightarrow{\alpha_x} I_x \cos\alpha \sin 2\alpha - I_y \sin 2\alpha(1 + \cos 2\alpha)/2 - I_z(\sin^2\alpha - \cos^2\alpha \cos 2\alpha) \\ &= 2I_x \cos^2\alpha \sin\alpha - 2I_y \cos^3\alpha \sin\alpha - I_z(1 - 2\cos^4\alpha). \end{aligned} \quad [3.100]$$

Because $|\cos\alpha| < 1$, $\cos^4\alpha < \cos^2\alpha$ and the composite pulse sequence yields more accurate inversion of I_z than does a simple pulse with rotation angle $2\alpha \approx 180^\circ$. Therefore, the composite pulse is compensated for rf inhomogeneity or "mis-setting" of the pulse lengths.

An approach similar to that used in deriving [3.81] is useful in deriving a propagator for the composite pulse. The present calculation assumes resonance offsets are negligible and considers only variation in B_1. The rotation angle $\alpha = \pi/2 + \varepsilon$, in which $\varepsilon = (\pi/2)(\omega_1/\omega_1^0 - 1)$, and ω_1^0 is the nominal value of the rf field strength corresponding to a $\pi/2$ rotation. The propagator for the composite pulse is first premultiplied by $\mathbf{U}_0\mathbf{U}_0^{-1}$, where $\mathbf{U}_0$ is the propagator for the ideal $(\pi/2)_x(\pi)_y(\pi/2)_x$ rotation:

$$\begin{aligned} \mathbf{U} &= \mathbf{R}_x(\alpha)\mathbf{R}_y(2\alpha)\mathbf{R}_x(\alpha) \\ &= \mathbf{U}_0\mathbf{U}_0^{-1}\mathbf{R}_x(\alpha)\mathbf{R}_y(2\alpha)\mathbf{R}_x(\alpha) \\ &= \mathbf{R}_x(\pi/2)\mathbf{R}_y(\pi)\mathbf{R}_x(\pi/2)\mathbf{R}_x(-\pi/2)\mathbf{R}_y(-\pi)\mathbf{R}_x(-\pi/2)\mathbf{R}_x(\alpha)\mathbf{R}_y(2\alpha)\mathbf{R}_x(\alpha) \\ &= \mathbf{R}_x(\pi/2)\mathbf{R}_y(\pi)\mathbf{R}_x(\pi/2)\mathbf{R}_x(-\pi/2)\mathbf{R}_y(-\pi)\mathbf{R}_x(-\pi/2) \\ &\quad \times \mathbf{R}_x(\pi/2)\mathbf{R}_x(\varepsilon)\mathbf{R}_y(\pi)\mathbf{R}_y(2\varepsilon)\mathbf{R}_x(\pi/2)\mathbf{R}_x(\varepsilon) \\ &= \mathbf{R}_x(\pi/2)\mathbf{R}_y(\pi)\mathbf{R}_x(\pi/2)\mathbf{R}_x(-\varepsilon)\mathbf{R}_y(-2\varepsilon)\mathbf{R}_x(\varepsilon) \\ &= \mathbf{R}_x(\pi)\mathbf{R}_z(-\pi)\mathbf{R}_x(-\varepsilon)\mathbf{R}_y(-2\varepsilon)\mathbf{R}_x(\varepsilon). \end{aligned} \quad [3.101]$$

When ε is small, then the rotation operators that depend on ε commute with each other and

$$\begin{aligned}\mathbf{U} &\approx \mathbf{R}_x(\pi)\,\mathbf{R}_z(-\pi - 2\varepsilon)\\ &\approx \mathbf{R}_x(\pi)\mathbf{R}_z\left(-\pi\omega_1/\omega_1^0\right)\\ &\approx \mathbf{R}_z\left(\pi\omega_1/2\omega_1^0\right)\mathbf{R}_x(\pi)\mathbf{R}_z\left(-\pi\omega_1/2\omega_1^0\right)\\ &\approx \mathbf{R}_z\left(\pi\omega_1/\omega_1^0\right)\mathbf{R}_x(\pi).\end{aligned} \qquad [3.102]$$

The penultimate line demonstrates that, for small variations in the B_1 field strength, the composite pulse acts like an ideal π pulse applied with phase $\pi\omega_1/2\omega_1^0$ The last line demonstrates that the composite pulse acts like an ideal π pulse applied with x-phase followed by a z-rotation with a rotation angle of $\pi\omega_1/\omega_1^0$. The result that the composite pulse represents an ideal rotation around a phase-shifted rotation axis is a property shared by all time-symmetric composite π pulses (*41*). As already noted, the z-rotation is unimportant for inversion of longitudinal magnetization, but results in phase shifts when used to refocus transverse magnetization.

The quarternion formalism also is useful in analyzing the performance of composite pulses by iterative application of [1.37]. Using this approach, the effective rotation angle, α_{eff}, of a time-symmetric composite pulse consisting of three pulses, $\alpha_0\alpha'_\phi\alpha_0$, is given by

$$\cos(\alpha_{\text{eff}}) = 2(\cos\alpha\cos(\alpha'/2) - \cos\phi\sin\alpha\sin(\alpha'/2)^2 - 1, \qquad [3.103]$$

and inversion of I_z magnetization is described by

$$I_z \xrightarrow{\alpha_{\text{eff}}} I_z\cos(\alpha_{\text{eff}}). \qquad [3.104]$$

For the composite pulse $\alpha_x(2\alpha)_y\alpha_x$,

$$\cos(\alpha_{\text{eff}}) = 2\cos^4\alpha - 1 = 2\cos^4\left(\pi\omega_1/2\omega_1^0\right) - 1, \qquad [3.105]$$

which is identical to the product operator calculation of [3.100].

For more detailed analysis, numerical calculations of the performance of a composite pulse are more convenient. Plots showing the theoretical performance of some selected composite pulses are shown in Fig. 3.20. Design of a composite 180° pulse that improves inversion of z-magnetization is considerably easier than is design of a composite 180° pulse for refocusing transverse magnetization. Inclusion of the composite pulse (most commonly, $90_x180_y90_x$ or $90_x240_y90_x$) into a pulse sequence whenever inversion of a z-operator is required frequently will improve the performance of the pulse sequence. In addition, composite

pulses are more useful for ^{13}C and ^{15}N than for ^{1}H because the larger chemical shift dispersion of the heteronuclei, relative to available rf field strengths, results in larger off-resonance effects. Amplifier droop, sample heating, and other instrumental imperfections may limit the total number or overall duration of composite pulses that can be included in a particular pulse sequence. Determination of which 180° pulses can be replaced profitably by composite pulses in a particular sequence frequently is an empirical process.

The development of composite pulses, particularly for broadband inversion and excitation applications, continues to be an active area of research. The continuing development of higher field magnets puts an ever-increasing demand on the broadband performance of inversion and excitation pulses. While intuition has historically played an important role in the design of composite pulses, increasing reliance is now made on sophisticated computer optimization methods and formalisms such as optimal control theory. Examples of the current state-of-the-art are found in the work of Shaka and co-workers regarding broadband inversion pulses (BIPs) (*42*) and in the work of Khaneja, Luy, Glaser, and co-workers on composite pulses designed by optimal control theory [(*43*) and references cited therein].

3.4.4 SELECTIVE PULSES

One of the original objectives in the development of pulsed NMR spectroscopy was to replace the time-consuming swept selective excitation of continuous-wave spectroscopy by broadband excitation using strong rf pulses. As spectrometer hardware has become more sophisticated and as the experimental systems studied have become more complex, the incorporation of selective pulses that excite resonances within a narrow frequency range into otherwise broadband pulse sequences has been shown to have some advantages: selective excitation of the solvent resonance can improve solvent suppression, spins with moderately different Larmor frequencies can be manipulated independently (i.e., carbonyl and C^{α} carbon spins), and the digitization requirements for multidimensional spectroscopy can be reduced (*44, 45*).

The simplest selective pulse is obtained by reducing the amplitude and lengthening the duration of a rectangular pulse, i.e., an rf field of constant amplitude, B_1, that is turned on at a time t and turned off at time $t + \tau_p$. As shown by [3.75], a rectangular pulse produces excitation over the range $-2\omega_1 \leq \Omega \leq 2\omega_1$. Such a simple approach is unsatisfactory because the excitation profile has lobes that extend over an extensive

frequency range, the phase of the transverse magnetization varies strongly with offset, and the excitation profile is not uniform in the neighborhood of the rf carrier frequency. The performance of selective (or soft) rectangular pulses can be improved by utilizing more complex amplitude or phase modulation of the rf field. Just as for composite pulses, integration of the Bloch equations to ascertain the excitation profile of a given selective pulse shape is straightforward. The inverse problem, determining the necessary pulse shape from the desired excitation profile, is much more difficult because of the nonlinear character of the Bloch equations. Accordingly, many selective pulses have been developed initially using approximate techniques (such as Fourier analysis of the desired excitation profile) and subsequently refined. The development of selective excitation pulses and their incorporation into multidimensional pulse sequences remain active areas of research and significant future progress can be expected.

The following characteristics of a selective pulse are desirable:

1. Uniform excitation or inversion profile over the desired frequency range.
2. Minimal perturbation of resonances outside the desired frequency range.
3. Phase of the transverse magnetization generated by excitation pulses should be a smooth (preferably linear) function of offset.
4. The pulse should have a short duration to minimize relaxation effects and phase evolution during the pulse.
5. The pulse modulation scheme should be simple to implement experimentally.

These objectives are not satisfied simultaneously for known pulse shapes. For example, some selective pulses that yield uniform excitation profiles include short high-power pulse segments; these pulse waveforms can be difficult to implement without special rf transmitters. Consequently, an optimal selective pulse cannot be determined without reference to the particular application.

For the purpose of calculations (and for implementation in spectrometer hardware), the continuous selective pulse shape is approximated by a large number, N, of rectangular pulses of length Δt. The amplitudes and phases of the rectangular pulses are adjusted to mimic the desired shape. Thus, the total duration of the selective pulse is $\tau_p = N\Delta t$,

$$\tilde{P}(\tau_p) = \prod_{i=1}^{N} P_{\phi_i}(\alpha_i). \qquad [3.106]$$

The net rotation induced by the selective pulse is given by

$$\mathbf{R}(\tau_p) = \prod_{i=1}^{N} \mathbf{R}_z(\phi_i)\mathbf{R}_y(\theta_i)\mathbf{R}_z(\alpha_i)\mathbf{R}_y(-\theta_i)\mathbf{R}_z(-\phi_i), \qquad [3.107]$$

in which ϕ_i, θ_i, and α_i represent the values of the phase, tilt angle, and effective rotation angle for the ith period Δt. The rotation matrices are given by [1.35]. The effective rotation angle and tilt angle are described by [1.23] and [1.21]. The magnetization following the selective pulse is

$$\mathbf{M}(0_+) = \mathbf{R}(\tau_p)\mathbf{M}(0_-), \qquad [3.108]$$

in which $\mathbf{M}(0_-)$ and $\mathbf{M}(0_+)$ are the magnetization vectors before and after the pulse, respectively. In contrast to [3.98], the duration τ_p for a selective pulse may not be short relative to either relaxation or evolution of scalar coupling interactions; accordingly, [3.108] describes the effect of a selective pulse on an uncoupled, isolated spin in the absence of relaxation effects.

The pulse shapes and excitation profiles for some common selective pulses are shown in Figs. 3.21–3.23. The most common, and simplest, applications of selective pulses in protein NMR spectroscopy are (*i*) decoupling of carbonyl and $^{13}C^{\alpha}$ spins by using selective 180° pulses (Chapter 7, Section 7.1.2.2) and (*ii*) selective excitation of the solvent resonance to obtain solvent suppression without deleterious effects of presaturation (Section 3.5.1). More sophisticated uses of selective pulses in multidimensional NMR spectroscopy are described by Kessler et al. (*45*).

3.4.5 PHASE-MODULATED PULSES

Many NMR experiments require that rf pulses be applied at more than one frequency, for a given nuclear species, during the course of a pulse sequence. One of the most common situations in protein NMR spectroscopy in which multiple-frequency irradiation is employed is in the implementation of triple-resonance (^1H, ^{13}C, ^{15}N) experiments. These experiments often require the ^{13}C transmitter frequency to be centered in different spectral regions at various times during the pulse sequence, such as when a selective 180° pulse is applied in the carbonyl region for decoupling purposes during an aliphatic carbon evolution period. Another common example requiring variable-frequency capability is the implementation of frequency sweeps during adiabatic pulses. In a typical spectrometer configuration, only one transmitter channel

is dedicated fo
therefore requ
multifrequency

Although r
for automatica
transmitter out

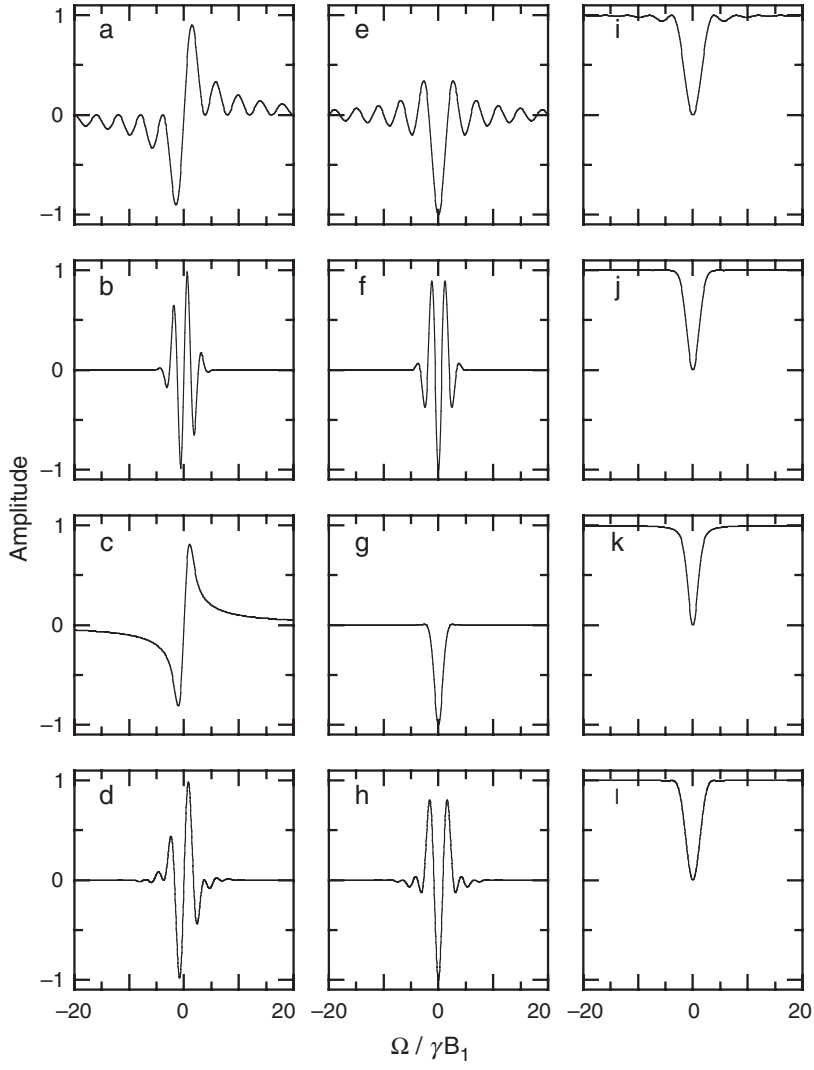

FIGURE 3.22 Selective 90° pulses. Resulting (a–d) M_x, (e–h) M_y, and (i–l) M_z magnetization components obtained following application of (a, e, i) rectangular, (b, f, j) Gaussian, (c, g, k) half-Gaussian 90°, and (d, h, l) SEDUCE-1 pulses to equilibrium M_z magnetization. Simulations used a peak field strength of $\omega_1/2\pi = 9.5\,\text{kHz}$, corresponding to pulse lengths of 26.2, 52.5, 52.5, and 56.9 μs for rectangular, Gaussian, half-Gaussian, and SEDUCE-1, respectively. All pulses have x-phase.

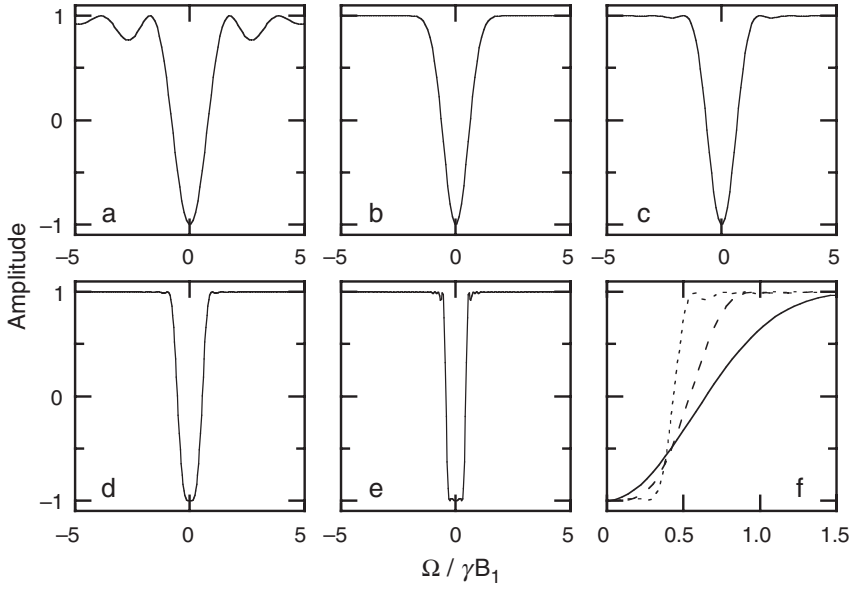

FIGURE 3.23 Selective 180° pulses. Resulting M_z magnetization obtained following application of (a) rectangular, (b) Gaussian, (c) sinc, (d) R-SNOB, and (e) RE-BURP 180° pulses to equilibrium M_z magnetization. Simulations used a peak field strength of $\omega_1/2\pi = 9.5\,\text{kHz}$, corresponding to pulse lengths of 52.5, 105, 89, and 246 μs, and 659 μs for rectangular, Gaussian, sinc, R-SNOB, and RE-BURP pulses, respectively. (f) The excitation profiles for (solid) Gaussian, (dashed) R-SNOB, and (dotted) RE-BURP pulse are superposed and expanded to more clearly indicate the transition band of the pulse.

nuclear species, this capability is not commonly used. Under suitable conditions, multifrequency excitation can be achieved using a single rf channel simply by appropriate shifts of the transmitter frequency during the pulse sequence. Most modern NMR spectrometers have the capability to shift a transmitter frequency under pulse sequence control within a few microseconds. In many experimental situations, frequency shifts must be done phase-coherently. A phase-coherent frequency shift means that no phase step occurs at the instant when the frequency transition occurs. Phase-coherent frequency shifts can be obtained with modern frequency synthesizers, at least for the limited size of frequency jumps that would normally be desired. One obvious limitation of employing explicit frequency shifts is that at any point in the pulse

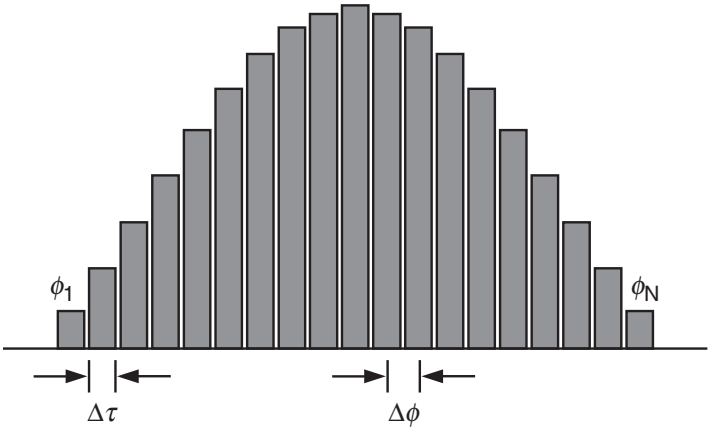

FIGURE 3.24 Phase-modulated pulse. Each rectangular element of the shaped pulse has duration $\Delta\tau$; the phase shift between rectangular elements is $\Delta\phi$. The initial and final phases, ϕ_1 and ϕ_N, respectively, are given by [3.110].

sequence, only a single transmitter frequency is obtainable for a given nuclear species. For example, simultaneous selective irradiation of the carbonyl and aliphatic ^{13}C resonances would not be possible.

An alternative method for achieving frequency agility of a transmitter channel is the use of phase-modulated pulses (*46, 47*). The concept is based on the fundamental equation $\omega = d\phi/dt$: a shift in the effective frequency is achieved by modulating the phase ϕ of the reference rf. In practice, a phase-modulated pulse, also referred to as a phase-incremented pulse (PIP) or a shifted laminar pulse (SLP), is implemented as a windowless series of short rectangular pulses, as illustrated in Fig. 3.24. Each component pulse has a constant phase and amplitude, and typically a constant duration $\Delta\tau$. The phase of the rf is incremented between each adjacent pair of pulses. For a fixed frequency shift, the phase increment is a constant, given by

$$\Delta\phi = (2\pi\Delta f)(\Delta\tau) \qquad [3.109]$$

where Δf is the desired frequency shift (in Hertz) and $\Delta\tau$ is the duration of the component pulses. Thus, the phase of a component pulse is specified by a linear phase ramp for a fixed frequency shift, and is given by

$$\begin{aligned} \phi_i &= \phi_0 + \Delta\phi/2 + \Delta\phi(i-1), \ldots \quad 1 \le i \le N \\ &= \phi_0 + \Delta\phi(i-1/2), \end{aligned} \qquad [3.110]$$

in which ϕ_0 is a constant that determines the phase of the initial component pulse, and the entire pulse consists of N elements of equal duration $\Delta\tau$. The term $\Delta\phi/2$ in the first line of [3.110] is referred to as the universal phase shift (*48*) and arises due to the quantized nature of the phase ramp. The value of the phase constant ϕ_0 must be determined from the specific nature of the phase-modulated pulse and the context in which it is employed; rules for choosing ϕ_0 are discussed below. Phase-modulated pulses of the type depicted in Fig. 3.24 give rise to multiple, asymmetric excitation sidebands in addition to the central excitation frequency band. The sidebands are located at frequencies (in Hertz) of $j/\Delta\tau$ in which j is a nonzero integer, relative to the centerband (*48*); typical choices for the value of $\Delta\tau$ place all sidebands well outside the spectral range of interest. A detailed analysis (*48, 49*) of the propagator for the phase-modulated pulse indicates that the effective rf field for the centerband excitation is scaled by the factor λ:

$$\lambda = \sqrt{2[1 - \cos(\Delta\phi)]}/|\Delta\phi|. \qquad [3.111]$$

As stated previously, the value of the initial phase ϕ_0 for the phase ramp given by [3.110] is determined by the specific characteristics of the overall pulse and the context in which the pulse is to be used. Several of the most commonly encountered situations are discussed here. If the phase-modulated pulse is intended to achieve an inversion of Iz magnetization, then the choice of ϕ_0 is unrestricted. For a 90° pulse intended to transform $I_\alpha \rightarrow I_z$, where I_α lies in the x–y plane (i.e., $\alpha = 0$ specifies I_x and $\alpha = \pi/2$ specifies I_y magnetization), $\phi_0 = \alpha - \pi/2$. Intuitively, this requirement is rationalized by realizing that, for example, a $I_y \rightarrow I_z$ transformation requires the initial component pulse must be a rotation about the x-axis in the rotating frame. For a 90° pulse intended to transform $I_z \rightarrow -I_y$, $\phi_0 = -(N-1)\Delta\phi$; in this case, the last component pulse must be a rotation about the x-axis in the rotating frame in order to leave the final magnetization along the $-y$-axis. For a 180° refocusing pulse that uses a time-symmetric amplitude modulation, such as the RE-BURP (*50*) or R-SNOB (*51*) pulses, the value of $\phi_0 = -N\Delta\phi/2$ must be chosen such that the middle element of the overall pulse has zero phase, assuming an effective rotation about the x-axis in the rotating frame is desired. This result can be arrived at via the following analysis (*41*). Let **A** and **B** represent the propagators for the first and second halves, respectively, of the time-symmetric refocusing pulse, with **A** being generated from the propagator for the ith component

pulse, $\mathbf{A}_i$:

$$\mathbf{A} = \prod_{i=1}^{N} \mathbf{A}_i = \mathbf{A}_1\mathbf{A}_2\mathbf{A}_3 \cdots \mathbf{A}_N. \qquad [3.112]$$

By definition of a time symmetric pulse, the propagator $\mathbf{B}$ can be expressed as:

$$\begin{aligned}\mathbf{B} &= \mathbf{A}_N \cdots \mathbf{A}_3\mathbf{A}_2\mathbf{A}_1 \\ &= \exp\{-i\pi I_z\}\mathbf{A}_N^{-1} \cdots \mathbf{A}_3^{-1}\mathbf{A}_2^{-1}\mathbf{A}_1^{-1} \exp\{i\pi I_z\} \\ &= \exp\{-i\pi I_z\}\mathbf{A}^{-1} \exp\{i\pi I_z\}. \qquad [3.113]\end{aligned}$$

The second line of [3.113] is obtained because the rotation axes of the component pulses of $\mathbf{A}$ lie in the x–y plane, in the absence of off-resonance effects. By definition, an 180° refocusing pulse applied along the x-axis will invert the y-component of the magnetization. Using [3.113], the result is obtained that

$$\begin{aligned}\left(\mathbf{B}^{-1}\mathbf{A}^{-1}\right)I_y(\mathbf{AB}) &= -I_y \\ \mathbf{A}^{-1}I_y\mathbf{A} &= -\mathbf{B}I_y\mathbf{B}^{-1} \\ &= -\exp\{-i\pi I_z\}\mathbf{A}^{-1} \exp\{i\pi I_z\}I_y \exp\{-i\pi I_z\}\mathbf{A} \exp\{i\pi I_z\} \\ &= \exp\{-i\pi I_z\}\left(\mathbf{A}^{-1}I_y\mathbf{A}\right) \exp\{i\pi I_z\}. \qquad [3.114]\end{aligned}$$

The last line of [3.114] indicates that the transformed vector $\mathbf{A}^{-1}I_y\mathbf{A}$ is unaffected by a 180° rotation about the z-axis. Therefore, the transformed vector must lie along the z-axis. Thus, the composite pulse represented by $\mathbf{A}$ will rotate an arbitrary vector from the transverse plane into the x–z plane. Intuitively, the last component pulse of $\mathbf{A}$ must be applied along the x-axis for the previous statement to be true. Applying a phase ramp to shift the excitation frequency does not alter this analysis; consequently, as previously stated, the center element of a time-symmetric refocusing pulse must have x-phase, assuming the desired net result is a rotation about the x-axis in the rotating frame.

To complete the discussion of the choice of the phase constant ϕ_0, the final example considers the case that multiple, phase-modulated pulses are combined to achieve some desired result, such as a frequency-shifted composite pulse. In this situation, the phase constant ϕ_0 for each

element of the composite pulse must take into account an inherited phase from the immediately preceding element (*49*).

For a frequency-swept rf pulse that is generated using phase modulation, the phase increment between adjacent component pulses can be variable. Once the time dependence of the frequency sweep is specified, the phase modulation function is determined from the fundamental relationship:

$$\phi(t) = \int_0^t \omega_{\text{sweep}}(\tau)\, d\tau, \qquad [3.115]$$

where $\omega_{\text{sweep}}(t)$ is the functional form of the desired frequency sweep. For example, if a linear frequency sweep is desired, $\omega_{\text{sweep}}(t) = kt$, and the phase modulation function will be

$$\phi(t) = \phi_0 + \frac{1}{2}kt^2 \qquad [3.116]$$

and the phase constant ϕ_0 is chosen using the principles discussed previously. The frequency-swept pulse is generated by subdividing the pulse into a series of component pulses, typically of constant duration $\Delta\tau$, with phases calculated according to [3.115]; amplitude modulation is achieved simply by scaling the amplitudes of the component pulses according to the time dependence of the amplitude profile.

A few comments are made here to facilitate the practical implementation of phase-modulated pulses. The sign of the phase increment $\Delta\phi$ in [3.109] and the sign of the calculated phase modulation function in [3.116] will depend on the convention employed in the spectrometer operating software. This is due to the fact that, relative to the effects of an rf pulse stipulated to be x-phase, a y pulse on a spectrometer from one manufacturer may correspond to a $-y$ pulse on a spectrometer from another manufacturer. The appropriate sign of $\Delta\phi$ for a given sign of Δf can be ascertained by examining an example waveform, which is usually a text file containing a list of pulse amplitudes and phases, or by performing an appropriate experiment using a simple phase-modulated pulse to empirically determine the sign convention. The sign convention determined by either approach is applicable for the construction of all other phase-modulated pulses on that spectrometer. Software programs, such as the Pulsetool program provided by Varian, Inc., that allow the simulation of spin dynamics using the Bloch equations are very useful for testing and optimizing phase-modulated pulses.

Generally speaking, an absolute requirement for generating a phase-modulated pulse is that the spectrometer hardware be capable of rapidly (i.e., <1 μs) executing small-angle phase shifts of the rf frequency. In generating the phase modulation, the exact phases stipulated by [3.111] or [3.115] can only be approximated, due to the finite phase resolution of the hardware; however, modern commercial spectrometers typically have a minimum phase step of 0.25° or less and the resulting quantization error is usually negligible. Although not an absolute requirement, the duration of the component pulses of a phase-modulated pulse is usually a constant, $\Delta\tau$. In choosing a value for $\Delta\tau$, the upper limit is determined by the desire to keep sideband excitation frequencies outside the spectral region of interest (*vide supra*). The value chosen for $\Delta\tau$ also should be an integer multiple of the minimum step size of the hardware unit that generates the pulses.

Frequency-shifted pulses generated using phase modulation have the desirable property that the frequency shifts are achieved phase coherently; depending on the spectrometer hardware, explicit frequency shifts using the rf frequency synthesizer may or may not be perfectly phase coherent. In addition, phase modulation can be used to generate multiple excitation frequencies simultaneously. If the individual frequency-selective pulses are represented by histograms of N component pulses, each with a prescribed phase and amplitude (as shown in Fig. 3.25), then the simultaneous excitation pulse profile is generated simply by calculating the vector sum of the individual waveforms at each time segment (*52*).

3.4.6 ADIABATIC PULSES

The rf pulses discussed up to this point have been employed to effect a specific rotation of a magnetization vector about the axis of the effective field $\mathbf{B}_{\text{eff}}$ in the rotating frame. If the pulse is applied on-resonance, then the angle between the effective field and the magnetization vector is 90°. Another possibility for manipulating magnetization that has several advantages is an adiabatic pulse (*53*). In such a pulse, $\mathbf{B}_{\text{eff}}$ initially is aligned approximately with the magnetization vector, and subsequently the axis of $\mathbf{B}_{\text{eff}}$ is caused to rotate adiabatically during the pulse. Under these conditions, the magnetization vector follows the same trajectory as $\mathbf{B}_{\text{eff}}$ to some desired endpoint. Essentially, the magnetization is locked along the direction of $\mathbf{B}_{\text{eff}}$ and caused to undergo the desired reorientation via tight control of the effective field direction during the course of the adiabatic pulse. Manipulating magnetization in such a fashion is commonly referred to as adiabatic following, or

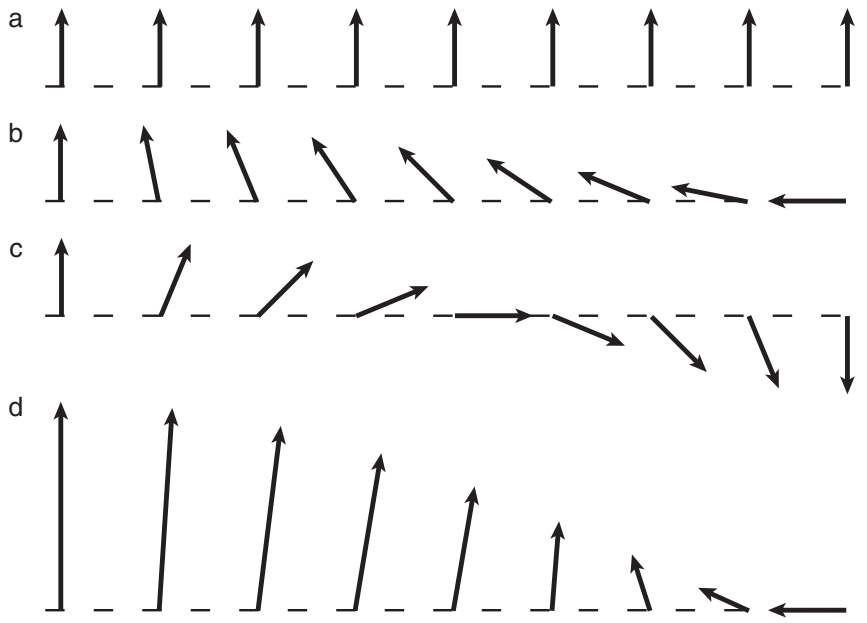

FIGURE 3.25 Vector representations of individual rf pulse elements comprising three separate phase-modulated pulses (a–c), and their combination to form a single composite pulse (d). The length of the vectors represents the rf pulse amplitude while the rotation from vertical represents the rf phase of each element. Waveform (a) represents a non-phase-modulated pulse, while waveforms (b, c) have phase modulations to generate frequency shifts. Each element of the composite pulse (d) is generated by addition of the corresponding vectors from each of the component elements in (a–c).

adiabatic rapid passage, where the term ''rapid'' refers to the fact that the adiabatic pulse should be executed in a time that is short relative to the relaxation time constants T_1 and T_2. The conditions required for such a pulse can be determined from the following analysis. For simplicity, the treatment considers uncoupled spins.

Under the influence of an arbitrary effective field $\mathbf{B}_{\text{eff}}$, the rate of change of the squared amplitude of a magnetization vector is given by

$$\frac{d}{dt}\left(M^2\right) = 2\mathbf{M}\cdot\frac{d\mathbf{M}}{dt} = 0. \qquad [3.117]$$

The right-hand equality is obtained because $\mathbf{M}$ and $d\mathbf{M}/dt$ are orthogonal, according to [1.10]. Thus, the amplitude of the

magnetization vector is unchanged under the influence of an arbitrary effective field, ignoring relaxation and scalar coupling effects. Consequently, the magnetization vector can be reoriented, but not changed in size. Therefore, the question arises as to how the relative orientation of the magnetization vector and the effective field axis will change as a function of time. If the effective field is fixed, independent of time in the rotating frame, then the analysis in Chapter 1 demonstrates that the magnetization vector precesses around the effective field while maintaining a fixed angle with respect to the effective field axis. If the effective field is time dependent, then the time dependence of the angle between $\mathbf{M}$ and $\mathbf{B}_{\text{eff}}$, denoted as $\angle(\mathbf{M}, \mathbf{B}_{\text{eff}})$, can be examined by considering the second derivative of $\mathbf{M}$, starting from [1.10]:

$$\frac{d^2\mathbf{M}}{dt^2} = \gamma^2(\mathbf{M} \times \mathbf{B}_{\text{eff}}) \times \mathbf{B}_{\text{eff}} + \gamma\mathbf{M} \times \frac{d\mathbf{B}_{\text{eff}}}{dt}. \qquad [3.118]$$

This equation differs from the case where $\mathbf{B}_{\text{eff}}$ is time independent (and hence $\angle(\mathbf{M}, \mathbf{B}_{\text{eff}})$ is a constant) by the addition of the second term on the right. Thus, if the following condition is true,

$$\left|\mathbf{M} \times \frac{d\mathbf{B}_{\text{eff}}}{dt}\right| \ll \left|\gamma(\mathbf{M} \times \mathbf{B}_{\text{eff}}) \times \mathbf{B}_{\text{eff}}\right|, \qquad [3.119]$$

then $\angle(\mathbf{M}, \mathbf{B}_{\text{eff}})$ will be approximately conserved. Any arbitrary vectors $\mathbf{u}$ and $\mathbf{v}$ satisfy the condition $|\mathbf{u} \times \mathbf{v}| \leq |\mathbf{u}||\mathbf{v}|$; therefore, the inequality expressed in [3.119] will be satisfied if

$$|\mathbf{M}|\left|\frac{d\mathbf{B}_{\text{eff}}}{dt}\right| \ll \left|\gamma(\mathbf{M} \times \mathbf{B}_{\text{eff}}) \times \mathbf{B}_{\text{eff}}\right| \leq \left|\gamma\right||\mathbf{M}||\mathbf{B}_{\text{eff}}|^2. \qquad [3.120]$$

Using the definition $\omega_{\text{eff}} = -\gamma|\mathbf{B}_{\text{eff}}|$, the inequality [3.120] simplifies to

$$\left|\frac{d\omega_{\text{eff}}}{dt}\right| \ll \omega_{\text{eff}}^2. \qquad [3.121]$$

An additional condition that must be met in order for a magnetization vector to undergo adiabatic passage is obtained by considering the following analysis. In the frame of reference rotating at the instantaneous frequency of the applied rf field $\mathbf{B}_1$, which is sometimes referred to as the frequency modulation (FM) frame, the effective field is given by $\mathbf{B}_{\text{eff}} = B_1(t)\mathbf{i} + (\Omega(t)/\gamma)\mathbf{k}$, in which the rf field is assumed to be applied along the x-axis in the FM frame. The effective field makes an angle θ with respect to the z-axis of the FM frame, so that $\tan\theta = \gamma B_1(t)/\Omega(t)$. A second rotating frame is defined with axes (x^{r}, y^{r}, z^{r}), where the x^{r}-axis

is collinear with the effective field $\mathbf{B}_{\text{eff}}$, the y^{r}-axis is collinear with the y-axis of the FM frame, and the rotation is about the y-, y^{r}-axis. The rotation of this second frame represents the motion of the effective field in the FM frame, and thus the angular velocity is given by $d\theta/dt$. Following the rotating coordinates procedure (*54*) that leads to [1.13], the effective field in the second rotating frame is given by $\mathbf{B}^{\text{r}}_{\text{eff}} = B_{\text{eff}}\mathbf{i}^{\text{r}} + (1/\gamma)(d\theta/dt)\mathbf{j}^{\text{r}}$. The magnetization vector will precess about the axis defined by $\mathbf{B}^{\text{r}}_{\text{eff}}$. For the magnetization vector to approximately preserve its orientation with respect to $\mathbf{B}_{\text{eff}}$, $\mathbf{B}^{\text{r}}_{\text{eff}}$ must be approximately collinear with the x^{r}-axis, which requires that

$$\begin{aligned} \left|\frac{1}{\gamma}\frac{d\theta}{dt}\right| &\ll |B_{\text{eff}}|, \\ \left|\frac{d\theta}{dt}\right| &\ll |\gamma B_{\text{eff}}| := \omega_{\text{eff}}. \end{aligned} \qquad [3.122]$$

Equation [3.122] is commonly referred to as the *adiabatic condition*, and indicates that for a magnetization vector to remain approximately aligned with the effective field, the rate of change in the direction of the effective field must be much slower than the precession frequency of the magnetization vector around the instantaneous effective field direction.

To further illustrate the physical basis for an adiabatic sweep, the sweep is considered to consist of n discrete pulses of equal duration Δt, which is, of course, how an adiabatic sweep normally is implemented on an NMR spectrometer. The ith pulse is defined by the values of θ_i and $\Delta\phi_i = \omega_{\text{eff},i}\,\Delta t$, in which θ_i is the tilt angle, $\omega_{\text{eff},i}$ is the magnitude of the effective field, and $\Delta\phi_i$ is the net rotation angle around the axis defined by the effective field during Δt. By construction, Δt is chosen short enough that $\Delta\phi_i$ is small. For mathematical convenience in the following discussion, the first pulse is defined as the first pulse element with $\omega_1 > 0$ and the nth pulse is defined as a pulse with $\omega_1 = 0$; consequently, $\theta_1 > 0$ and $\theta_n = \pi$.

Using [1.34], evolution during the initial time period Δt is described by

$$\mathbf{M}(\Delta t) = R_y(\theta_1)R_z(\Delta\phi_1)R_y(-\theta_1)\mathbf{M}_0. \qquad [3.123]$$

The evolution during the second time period Δt is described by

$$\begin{aligned} \mathbf{M}(2\Delta t) &= R_y(\theta_2)R_z(\Delta\phi_2)R_y(-\theta_2)\mathbf{M}(\Delta t) \\ &= R_y(\theta_2)R_z(\Delta\phi_2)R_y(-\theta_2)R_y(\theta_1)R_z(\Delta\phi_1)R_y(-\theta_1)\mathbf{M}_0 \\ &= R_y(\theta_2)R_z(\Delta\phi_2)R_y(-\Delta\theta_2)R_z(\Delta\phi_1)R_y(-\Delta\theta_1)\mathbf{M}_0, \end{aligned} \qquad [3.124]$$

in which $\Delta\theta_i = \theta_i - \theta_{i-1}$ and $\theta_0 \equiv 0$. Continuing this process leads to the result

$$\begin{aligned}\mathbf{M}(n\Delta t) &= R_y(\pi)\left\{\prod_{i=1}^{n} R_z(\Delta\phi_i)R_y(-\Delta\theta_i)\right\}\mathbf{M}_0 \\ &= \left\{\prod_{i=1}^{n} R_z(-\Delta\phi_i)R_y(-\Delta\theta_i)\right\}R_y(\pi)\mathbf{M}_0. \end{aligned} \quad [3.125]$$

If the average values of $\Delta\theta_i$ and $\Delta\phi_i$ are defined as $\overline{\Delta\theta}$ and $\overline{\Delta\phi}$, respectively, then $\Delta\theta_i = \overline{\Delta\theta} + \delta\theta_i$ and $\phi_i = \overline{\Delta\phi} + \delta\phi_i$. Using these expressions,

$$\begin{aligned}\mathbf{M}(n\Delta t) &= \left\{\prod_{i=1}^{n} R_z(-\overline{\Delta\phi})R_z(-\delta\phi_i)R_y(-\overline{\Delta\theta})R_y(-\delta\theta_i)\right\}R_y(\pi)\mathbf{M}_0 \\ &= \left\{\prod_{i=1}^{n} R_z(-\overline{\Delta\phi})R_y(-\overline{\Delta\theta})\right\}R_y(\pi)\mathbf{M}_0 \\ &= \left[R_z(-\overline{\Delta\phi})R_y(-\overline{\Delta\theta})\right]^n R_y(\pi)\mathbf{M}_0, \end{aligned} \quad [3.126]$$

in which the second line is obtained by assuming all the rotations in the curly braces are small enough to commute with each other and noting that $\sum \delta\theta_i = \sum \delta\phi_i = 0$. The product rotation in the square brackets on the final line of [3.126] can be expressed as a single rotation of angle α around an axis $\hat{\mathbf{n}}$ by using [1.37], in which

$$\begin{aligned}\cos\left(\frac{\alpha}{2}\right) &= \cos\left(\frac{\overline{\Delta\theta}}{2}\right)\cos\left(\frac{\overline{\Delta\phi}}{2}\right), \\ \sin\left(\frac{\alpha}{2}\right)\hat{\mathbf{n}} &= -\sin\left(\frac{\overline{\Delta\theta}}{2}\right)\sin\left(\frac{\overline{\Delta\phi}}{2}\right)\mathbf{i} - \sin\left(\frac{\overline{\Delta\theta}}{2}\right)\cos\left(\frac{\overline{\Delta\phi}}{2}\right)\mathbf{j} \\ &\quad - \cos\left(\frac{\overline{\Delta\theta}}{2}\right)\sin\left(\frac{\overline{\Delta\phi}}{2}\right)\mathbf{k}. \end{aligned} \quad [3.127]$$

Using this result,

$$\mathbf{M}(n\Delta t) = R_{\hat{\mathbf{n}}}(n\alpha)R_y(\pi)\mathbf{M}_0. \quad [3.128]$$

The angle between the $-z$-axis and $\hat{\mathbf{n}}$ is given by

$$\zeta = \tan^{-1}\left(\frac{\sin\left(\overline{\Delta\theta}/2\right)}{\cos\left(\overline{\Delta\theta}/2\right)\ \sin\left(\overline{\Delta\phi}/2\right)}\right) \approx \frac{\overline{\Delta\theta}}{\overline{\Delta\phi}} \quad [3.129]$$

in which the second equality is obtained because $\overline{\Delta\theta}$ and $\overline{\Delta\phi}$ are small. Thus, the adiabatic sweep is modeled theoretically by an initial ideal

inversion around the y-axis followed by a rotation around the axis $\hat{\mathbf{n}}$ by an angle $n\alpha$. An ideal inversion occurs if ζ is sufficiently small, because then the magnetization never precesses significantly away from the $-z$-axis, regardless of the value of α: 2ζ is the maximum deviation between the magnetization vector and the $-z$-axis. Assuming that $\zeta \ll 1$ is sufficient to ensure ideal inversion yields:

$$\overline{\Delta\theta} \ll \overline{\Delta\phi}, \quad \frac{\overline{\Delta\theta}}{\Delta t} \ll \frac{\overline{\Delta\phi}}{\Delta t}, \qquad \left|\left\langle \frac{d\theta}{dt} \right\rangle\right| \ll \langle\omega_{\text{eff}}\rangle, \tag{3.130}$$

in which $\langle\omega_{\text{eff}}\rangle = \overline{\Delta\phi}/\Delta t$. Thus, the condition for an ideal inversion derived from this approach is equivalent to the adiabatic condition derived in [3.122]. Using [3.129] and [3.128], the angle ζ, which determines the departure of the final state of the magnetization from an ideal inversion, also is given by

$$\zeta = \left[\langle\omega_{\text{eff}}\rangle \Big/ \left|\left\langle \frac{d\theta}{dt} \right\rangle\right| \right]^{-1}. \tag{3.131}$$

The quantity inside the square brackets is closely related to the adiabaticity factor, which plays an important role in determining the quality of adiabatic pulses. The adiabaticity factor is discussed more fully later.

A pictorial model for the evolution of magnetization during an adiabatic sweep is provided by the following simplified case: the orientation of the effective field makes n instantaneous jumps of equal angular increments, $\Delta\theta$, in the y–z plane of the FM reference frame at equally spaced time intervals, Δt; the effective field is assumed to be of constant amplitude, ω_{eff}; the magnetization precesses about the current direction of the effective field by an equal angle $\Delta\varphi = \omega_{\text{eff}}\Delta t$ during each time interval; and the magnetization vector is initially taken to be collinear with the starting position of the effective field along the $+z$-axis. A graphical representation of this simple model is provided by the gnomonic projection diagram in Fig. 3.26a, as originally presented by Powles (*55*). The horizontal line in Fig. 3.26a represents the great circle trajectory of the intersection point of the effective field vector on a sphere of radius M, where M is the amplitude of the magnetization vector. This diagram shows that the deviation of the magnetization vector from the effective field direction is constrained. In the arbitrarily chosen case for $\Delta\phi = 0.7$ radians (40°), the maximum deviation of the tip of the magnetization vector is $y_{\max} \approx 2.9M|\Delta\theta|$. The maximum angular deviation, defined as α, of the magnetization vector from the effective field direction satisfies the relation $\tan\alpha = y_{\max}/M$. Therefore,

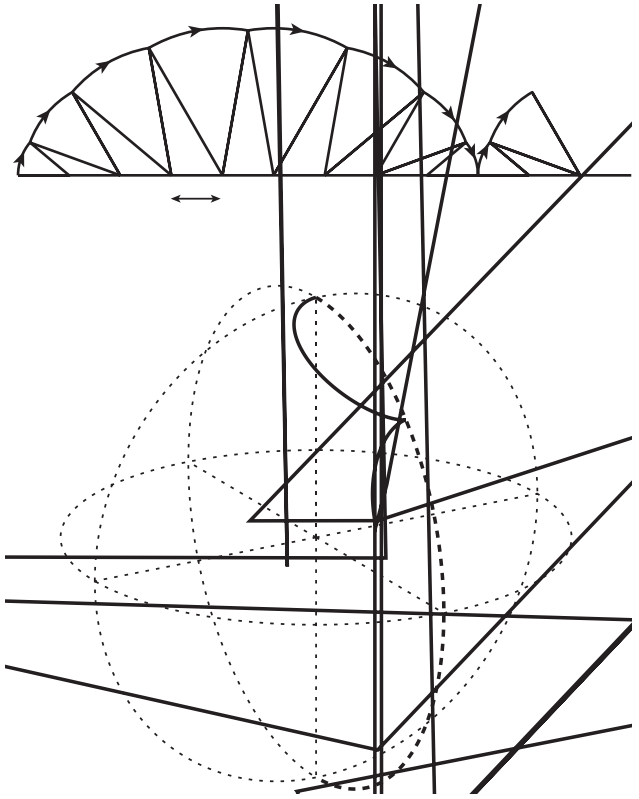

for α to remain very small, the condition $y_{max} \ll M$ must be satisfied, which requires $|\Delta\theta| \ll 0.3$ radians. Because $\Delta\phi = 0.7$ radians, the condition for α to remain very small can be written as $|\Delta\theta| \ll \Delta\phi$, or equivalently, $|d\theta/dt| \ll (d\phi/dt) = \omega_{eff}$, which is the result given by the second adiabatic condition, [3.122]. Inspection of Fig. 3.26a demonstrates that the adiabatic condition would result regardless of the choice of the scale $M\Delta\theta$ and the precession angle $\Delta\phi$.

A physically more accurate picture of the evolution of magnetization during an adiabatic sweep is shown in Fig. 3.26b. This figure provides a perspective view of the trajectories of the effective field and the magnetization vector, calculated via a numerical simulation of the Bloch equations (ignoring relaxation effects). The trajectory of the tip of the precessing magnetization trajectory is shown as a solid line on the unit sphere; the pathway followed by the effective field (the FM frame) is shown as a heavy dashed line. For the simulation, the amplitude of the effective field is assumed constant, the directory of the effective field vector is assumed to rotate in the y–z plane at a constant angular velocity $d\theta/dt$, and the precession frequency ω_e of the magnetization vector about the effective field is set to $\omega_e = 8d\theta/dt$. Under these conditions, the magnetization vector follows the effective field, as expected.

The adiabatic condition, [3.122], limits the rate of change of the effective field, but otherwise does not specify the exact manner in which the effective field should be controlled in order to accomplish the desired result. The effective field is specified by the applied rf field ω_1 $(= -\gamma B_1)$ and the resonance offset Ω; thus, the amplitude and orientation of the effective field are modulated by the time dependences of ω_1 and Ω. Determining optimal modulation functions for the amplitude and frequency of the applied rf field has been an active area of research. A parameter for characterizing the adiabaticity of a pulse that has proved to be useful in design efforts is the dimensionless quantity Q (*56*):

$$Q = \frac{\omega_{eff}}{|d\theta/dt|}, \qquad [3.132]$$

which is referred to as the adiabaticity factor. To strictly satisfy the adiabatic condition, [3.122], Q should be much greater than one. Using the relationship $\tan\theta = \omega_1/\Omega$, [3.132] becomes

$$Q = \frac{\left(\omega_1^2 + \Omega^2\right)^{3/2}}{\left|\omega_1 \dfrac{d\Omega}{dt} - \Omega \dfrac{d\omega_1}{dt}\right|}. \qquad [3.133]$$

A critical point in an adiabatic pulse occurs when the rf field sweeps through the resonance frequency, i.e., when $\Omega = 0$, because at this point the adiabaticity factor reaches a minimum:

$$Q_0 = \frac{\omega_1^2}{|d\Omega/dt|_{\Omega=0}}. \qquad [3.134]$$

One of the principal applications of an adiabatic pulse is to perform broadband inversion, whereby magnetization is rotated from the $+z$-axis (in the laboratory frame) to the $-z$-axis, or *vice versa*. In an adiabatic inversion pulse, the frequency of the rf field is far off-resonance at the beginning of the pulse, is swept through a frequency band of interest, and is far off-resonance on the other side of the frequency band at the end of the pulse. If the adiabatic condition [3.122] is maintained, i.e., if the rate of change of the effective field axis is significantly smaller than is the size of the effective field at all points during the frequency sweep, then the nuclear magnetization vector will track the effective field vector. If the nuclear magnetization vector is aligned with the effective field at the beginning of the sweep, then the magnetization vector will be inverted at the end of the sweep. A principal advantage of an adiabatic pulse is its insensitivity to B_1 inhomogeneity. As long as ω_1 is sufficiently large to satisfy the adiabatic condition $Q_0 \gg 1$, the magnetization vector remains nearly collinear with the effective field (in common terminology, the magnetization is said to be spin-locked to the effective field). This insensitivity to B_1 inhomogeneity has made adiabatic pulses particularly valuable in *in vivo* spectroscopy and imaging applications, where the nature of the rf transmitter coils inherently results in poor rf homogeneity. Adiabatic pulses also have superior performance with respect to off-resonance effects, compared to conventional pulses or composite pulses.

The orientation of the effective field $\mathbf{B}_{\text{eff}}$ is determined by the amplitude and frequency of the rf field. The adiabatic sweep can therefore be accomplished by a suitable modulation of either or both of these parameters. Design criteria include maximum rf field amplitude, desired bandwidth, frequency selectivity, total pulse width, power efficiency, and sensitivity to rf inhomogeneity; in the case of coupled spins, the size of the scalar couplings should also be taken into account. The simplest scheme is the so-called CHIRP pulse that utilizes a linear frequency sweep with a constant rf amplitude. The main drawback of the CHIRP scheme is that sudden switching on (off) of the rf field at the beginning (end) of the pulse can cause a violation of the adiabatic condition. A modulation scheme in which the rf

amplitude has a sine dependence and the frequency sweep has a cosine dependence on time yields an effective field with constant amplitude. A popular adiabatic pulse, the hyperbolic secant or sech/tanh pulse, uses the modulation scheme (*56, 57*)

$$\begin{aligned} B_1(t) &= B_1^0 \,\mathrm{sech}(\beta t), \\ \Omega(t) &= -\mu\beta \,\tanh(\beta t), \end{aligned} \qquad [3.135]$$

in which β and μ are real constants. The hyperbolic pulse exhibits a sharp transition between the regions where the magnetization vector experiences an inversion and the regions where the magnetization vector is unaffected. Thus, the hyperbolic secant pulse has the attractive properties of broad bandwidth and high selectivity. This pulse also exhibits constant adiabaticity over its bandwidth, allowing rf power to be used most efficiently. A potential drawback to the hyperbolic secant pulse is the high peak rf power required to achieve a broad bandwidth, which can be detrimental to the probe.

To minimize the rf peak power, the so-called WURST scheme has proved to be quite effective (*58*). The WURST family of adiabatic pulses is closely related to CHIRP, in the sense that a linear frequency sweep is employed. To eliminate the violations of the adiabatic condition at the beginning and end of the CHIRP pulse, the WURST scheme provides for a smooth transition to and from the peak rf field using an amplitude modulation given by the function

$$\omega_1(t) = \omega_1^{\max}\left\{1 - \left|\sin(\beta t)\right|^n\right\}, \qquad [3.136]$$

where $\omega_1^{\max}$ is the peak rf field strength, βt is the orientation of the effective field at time t ($-\pi/2 \le \beta t \le \pi/2$), and n is an index that determines the steepness of the rounding function at the beginning and end of the frequency sweep. The index n typically is chosen using the rule of thumb $n \approx \tau_p \Delta F/2$, where ΔF is the total sweep range (in Hertz) and τ_p is the duration of the sweep. The linear frequency sweep rate is given by $d\Omega/dt = 2\pi\Delta F/\tau_p$. The root-mean-square field strength of a WURST pulse is determined by the index n according to the function

$$\omega_1^{\mathrm{rms}} = \omega_1^{\max}\left\{1 - 2\left[\frac{(n-1)!!}{n!!}\right] + \left[\frac{(2n-1)!!}{(2n)!!}\right]\right\}^{1/2}, \qquad n \text{ even}, \quad n \neq 0,$$

$$\omega_1^{\mathrm{rms}} = \omega_1^{\max}\left\{1 - \frac{4}{\pi}\left[\frac{(\mathrm{n}-1)!!}{\mathrm{n}!!}\right] + \left[\frac{(2\mathrm{n}-1)!!}{(2\mathrm{n})!!}\right]\right\}^{1/2}, \qquad \mathrm{n} \text{ odd}, \quad \mathrm{n} \neq 1, \qquad [3.137]$$

where the expression $n!!$ refers to the double factorial

$$n!! \equiv \begin{cases} n(n-2)\cdots \times 5 \times 3 \times 1, & n > 0 \text{ odd} \\ n(n-2)\cdots \times 6 \times 4 \times 2, & n > 0 \text{ even} \\ 1, & n = -1, 0. \end{cases} \quad [3.138]$$

The index n is also related to the bandwidth of the inversion profile of a WURST pulse: the higher the value of n, the broader the bandwidth. The on-resonance adiabicity factor Q_0, [3.122], can be rearranged to give

$$\Delta F = \frac{\left(\omega_1^{\max}\right)^2 \tau_p}{2\pi Q_0}. \quad [3.139]$$

Adiabatic pulses are generally straightforward to implement on modern NMR spectrometers. Such instruments are normally equipped with hardware for performing the necessary amplitude modulation of the rf pulse. The only caveat here is that if the peak rf amplitude drives the rf power amplifier into its nonlinear region of operation, the shape function must be appropriately modified in order to obtain the desired output. The frequency sweep is normally achieved by a corresponding phase modulation, as described in Section 3.4.5. Thus, an adiabatic pulse is normally implemented by concatenating a series of individual rectangular pulses with the prescribed amplitudes and phases. The number of incremental pulses, N, should satisfy $N \geq \Delta F \tau_p$ to avoid aliasing.

An example of the amplitude and frequency modulation functions and the inversion profile for a WURST pulse with $n = 20$ and $Q_0 = 5$ is shown in Fig. 3.27. Unlike the plots shown for composite pulses, Fig. 3.20, the inversion performance of the WURST sequence is plotted as a function of the absolute resonance offset frequency, instead of a relative offset, because a simple linear relationship between the inversion bandwidth and the rf field strength γB_1 does not exist.

In the form just described, adiabatic pulses are most often used to effect the inversion transformation $M_z \leftrightarrow -M_z$; in this case, the pulse is referred to as adiabatic full passage (AFP). In an adiabatic half-passage (AHP), the pulse is terminated at the point where the magnetization crosses the transverse plane. Because the point in time at which the magnetization vector passes through the transverse plane is dependent on when the frequency sweep passes through a given resonance, an AHP pulse will have a narrow bandwidth when used as a 90° excitation pulse. The simple AHP pulse has proved to be very useful in rotating-frame relaxation experiments for orienting the magnetization vector along a local effective field direction at the beginning of spin lock period, and

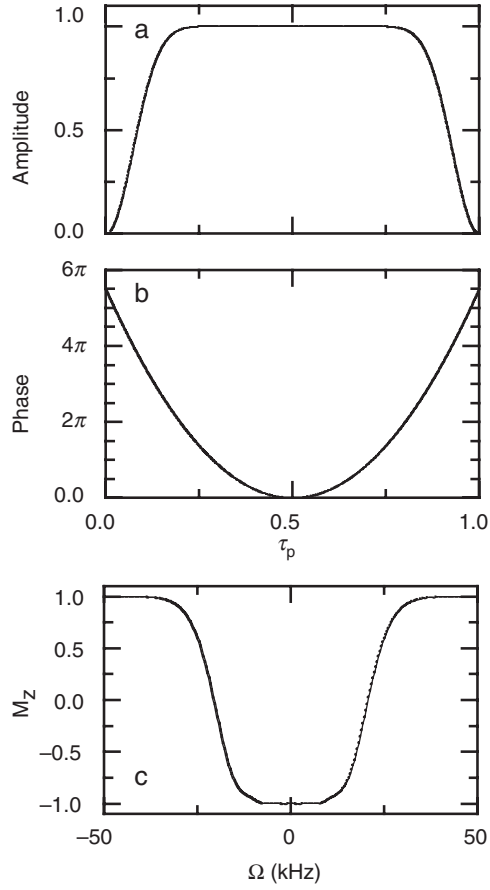

FIGURE 3.27 Pulse shape and excitation profile for a WURST-20 adiabatic sweep. (a) The amplitude profile calculated using $\omega_1^{\max}/2\pi = 9512$ Hz and $n = 20$ is shown. (b) The time dependence of the pulse phase, used to generate the linear frequency sweep, is shown. A 50,000-Hz frequency sweep and pulse length of 440 μs were assumed. In practical implementation on an NMR spectrometer, the phases shown would be converted to the range $-\pi$ to π. (c) The inversion profile for M_z magnetization is shown.

for restoring the magnetization to the z-axis after the spin lock period (*59*). The mode of action of simple adiabatic pulses means that plane rotations cannot be achieved. A plane rotation transforms all magnetization vectors, regardless of initial orientation, through the same angle about a single rotation axis. Thus, the simplest forms of an adiabatic pulse

are not useful as refocusing 180° pulses. However, schemes have been invented to create composite adiabatic pulses that accomplish all of the rotations possible with conventional pulses (*60, 61*). Pairs of adiabatic pulses also are useful for refocusing magnetization (*53*).

In the preceding discussion involving geometrical pictures of adiabatic following, scalar couplings were assumed to be negligible. In fact, most of this analysis remains valid so long as the rf field (in frequency units) is much larger, compared to the scalar couplings. Elegant treatments of the effects of adiabatic pulses on coupled spin systems have been presented (*62–64*).

3.5 Spin Decoupling

As has been discussed extensively in Chapter 2, if two spin-1/2 nuclei I and S are scalar coupled with a coupling constant J_{IS}, evolution of transverse magnetization of the I spin leads to splitting of the resonance signal into two multiplet components at frequencies $\omega_I + \pi J_{IS}$ and $\omega_I - \pi J_{IS}$ ($\nu_I + J_{IS}/2$ and $\nu_I - J_{IS}/2$, in Hertz). Removing the resonance splitting caused by the scalar coupling to the S spin when recording the FID for the I spin, a procedure called spin decoupling, increases the signal intensity and simplifies the I spin spectrum. Product operator calculations demonstrate that if a series of 180° pulses are applied selectively at the frequency of the S spin, then the effect of the scalar coupling interaction is refocused and the net evolution of the I spin yields a single resonance signal at ω_I. In the limit that the pulse spacing approaches zero, decoupling is obtained by applying a continuous rf field at the resonance frequency of the S spin while observing the I spin.

3.5.1 SPIN DECOUPLING THEORY

This simple picture of spin decoupling suffers from the defect that pulses are assumed to be infinitely short, so that evolution under the scalar coupling and Zeeman Hamiltonians may be ignored, when applying the product operator formalism. This assumption is not valid if an rf field is applied for an extended period of time. Furthermore, as discussed in Section 3.4.1, the performance of a nominal 180° pulse in inverting magnetization is a strong function of resonance offset and rf inhomogeneity. These effects are arduous to analyze for multiple pulse sequences using the product operator formalism. A more sophisticated theoretical approach is necessary to design and evaluate methods for spin decoupling. The principles of the modern theory of spin decoupling

were developed by Waugh (*65*), extending the work of other pioneers in the field. The theory of spin decoupling has been reviewed elegantly by Shaka and Keeler (*66*), and only a brief description of the basic concepts is presented here.

Reference to the energy level diagram for a weakly coupled *IS* spin-1/2 system (Fig. 1.7) provides some insight into the principles upon which modern decoupling theory is based. The NMR spectrum that would result from the transitions indicated by the arrows in Figure 1.7b is shown in Fig. 1.7d. From the energy levels shown in Fig. 1.7b, the frequencies of the four single-quantum transitions in the absence of spin decoupling are [1.58]

$$\begin{aligned} f(I_1) &= \omega_{13} = \omega_I - \pi J_{IS}, \quad f(I_2) = \omega_{24} = \omega_I + \pi J_{IS}, \\ f(S_1) &= \omega_{12} = \omega_S - \pi J_{IS}, \quad f(S_2) = \omega_{34} = \omega_S + \pi J_{IS}, \end{aligned} \tag{3.140}$$

in which the four observable transitions are labeled I_1, I_2, S_1, and S_2. By observation, a frequency sum rule is seen to exist:

$$f(I_1) + f(S_2) = f(I_2) + f(S_1). \tag{3.141}$$

This sum rule is obeyed even if a spin decoupling pulse sequence is being applied to one of the spins. Equation [3.141] can be rearranged to give

$$g(I_1) - g(I_2) = g(S_1) - g(S_2), \tag{3.142}$$

where the change of symbol $f \rightarrow g$ is simply meant to indicate that the transition frequencies in the presence of a decoupling sequence applied to spin S will not necessarily be the same as for the undecoupled case [3.140]. By definition, the goal of spin decoupling is to achieve the result that $g(I_1) \approx g(I_2)$; in order to do so, [3.142] indicates that the decoupling sequence applied to the S spins must force the two components of the S spin doublet to precess at the same frequency, so that $g(S_1) \approx g(S_2)$.

In principle, even a coherent, continuous-wave (cw) rf field applied to the S spins can result in good decoupling, as long as the rf field strength is sufficiently strong and the rf frequency is set close to the S spin resonance. However, cw decoupling is very inefficient for achieving broadband decoupling, because the rf field strength would need to be increased to impractical levels in order to overcome the effect of resonance offset. The challenge for achieving efficient (i.e., minimal rf power) broadband decoupling performance is to design a pulse sequence that results in the two S spin transition frequencies being essentially equal over as wide a chemical shift range as possible. The decoupling condition, that the two S spin vectors be forced to have the same precession frequency, does not impose a requirement for any particular

trajectory under the influence of the decoupling pulse sequence. However, in practice, imposing the condition of cyclicity greatly facilitates the design of broadband decoupling sequences. A pulse sequence element is cyclic if a spin vector evolves such that it returns to its initial orientation at the end of the pulse sequence element. The simplest pulse sequence element that is cyclic is a 360° pulse. If the S spin is subjected to a decoupling sequence that causes the two component S spin vectors to return to their initial position after each application of the primitive pulse sequence element, then the condition $g(S_1) \approx g(S_2)$ will be achieved. For broadband decoupling performance, the combination of two optimized 180° pulses, each referred to here as an R element, to give a net 360° pulse sequence RR, exploits the extensive efforts that have been made to design broadband inversion (i.e., 180°) pulses. This strategy, pioneered by Levitt and Freeman, is generally referred to as *composite pulse decoupling*, where the decoupling sequence is composed of a continuous series of composite 180° pulses.

A limitation implied in the preceding presentation is that the I spin FID is sampled stroboscopically with the cyclic perturbations of the S spin magnetization. In practice however, the FID must be sampled more rapidly. As a result, sampling points will occur at times when the trajectories of the two S spin magnetizations have diverged, which leads to small-amplitude modulations of the I spin FID. These modulations result in the appearance of cycling sidebands symmetrically located about the I spin resonance in the frequency spectrum. These sidebands occur at the cycling frequency and its harmonics. Although cycling sidebands are typically small in amplitude, their presence can significantly degrade the quality of an NMR spectrum in a high dynamic range situation, where weaker peaks of interest can be difficult to identify amid sideband peaks associated with nearby stronger resonances. The exact pattern and amplitude of cycling sidebands are strongly dependent on the details of the decoupling pulse sequence, and can be a significant factor in the choice of decoupling sequences for particular applications. Cycling sidebands can be attenuated by various techniques, such as applying the decoupling sequence in an asynchronous manner, meaning that the relationship between the start of the acquisition period and the decoupling cycle is not fixed.

Optimizing the efficiency of spin decoupling sequences is very important for studies of biomolecules, due to the need to decouple over ever-widening frequency bandwidths as magnetic field strengths increase. Most commonly in the NMR spectroscopy of proteins, the ^{1}H signal is recorded and the heteronuclear spins are decoupled; therefore, the broad chemical shift range of species such as ^{13}C also

presents a significant challenge. The situation is exacerbated by the solution conditions required for studies of the biomolecules, because lossy buffers (e.g., composed of a high concentration of ionic or polar species) make samples very susceptible to dielectric heating from the electric field component of the rf irradiation. This heating effect becomes worse at higher frequencies. In composite pulse decoupling, optimization of decoupling performance is generally approached by developing improved broadband 180° pulse sequence elements and finding a prescription for concatenating such elements to minimize the effects of their imperfections. In the following section, an outline of the principles used to develop improved spin decoupling sequences is presented.

One measure of the efficiency of a decoupling sequence is the ratio of the scalar coupling observed in the decoupled NMR spectrum versus that in the undecoupled spectrum as a function of the resonance offset Ω and rf field strength γB_1. Using this ratio, designated $\lambda_c(\Omega)$, with the so-called λ-approximation, gives (*66*)

$$\lambda_c(\Omega) = \frac{1}{t_s}\left|\frac{\partial\beta}{\partial\Omega}\right|, \qquad [3.143]$$

where β is the net rotation angle experienced by a spin vector under the influence of one complete cycle of the decoupling sequence, calculated as a function of the offset frequency Ω, and t_s is the duration of a complete cycle. For continuous rf irradiation, the scaling factor is

$$\lambda_c(\Omega) = \cos\theta = \frac{\Omega}{\sqrt{(\gamma B_1)^2+\Omega^2}}, \qquad [3.144]$$

which simply reflects the projection of the scalar coupling Hamiltonian into the tilted reference frame of the effective field for the S spin. Perfect decoupling, $\lambda_c(\Omega) = 0$, is obtained only for on-resonance irradiation. For off-resonance irradiation, effective decoupling requires that $\gamma B_1 \gg \Omega$, which is a condition that is extremely difficult to achieve experimentally. For example, if $|\Omega/(\gamma B_1)| = 1$, then $\lambda_c(\Omega) = 0.707$, which provides marginal reduction in the coupling constant.

3.5.2 COMPOSITE PULSE DECOUPLING

The preceding discussion suggested that efficient spin decoupling can be achieved by applying a series of composite 180° pulses. In the limit that the pulse spacing approaches zero, a phase-modulated rf field is obtained that can be described as the repetition of some

phase-modulated sequence R representing the composite 180° pulse. Coherent averaging theory (*65*) demonstrates that this approach in fact improves decoupling and also leads to the conclusion that, given a sequence element R, improved sequence elements can be developed by recursive expansion of R into supercycles. For example, if R is a composite 180° pulse and $\bar{R}$ is obtained by inverting the phases of the pulses comprising R, then the cyclic supercycles

$$\begin{gathered} R\bar{R}\bar{R}\bar{R} \\ R\bar{R}\bar{R}\ \bar{R}R\bar{R}\bar{R} \\ R\bar{R}\bar{R}\ \bar{R}R\bar{R}\ \bar{R}\bar{R}R\bar{R}\ R\bar{R}\bar{R}R \end{gathered} \tag{3.145}$$

yield progressively better decoupling performance. In addition, if R is a composite pulse sequence, then $R_{\mathrm{p}}\bar{R}_{\mathrm{p}}$ performs better than R. The element R_{p} is obtained by cyclically permuting a 90° pulse with the element R. For example, if R is

$$R = 90_x 180_{-x} 270_x = 1\bar{2}3, \tag{3.146}$$

then

$$R\bar{R}\bar{R}\bar{R} = 1\bar{2}3\ 1\bar{2}3\ \bar{1}2\bar{3}\ \bar{1}2\bar{3} \tag{3.147}$$

improves upon R. If this element is cyclically permuted from left to right,

$$\begin{aligned} R_{\mathrm{p}} &= \bar{2}3\ 1\bar{2}3\ \bar{1}2\bar{3}\ \bar{1}2\bar{3}\ 1 \\ &= \bar{2}4\bar{2}3\bar{1}2\bar{4}2\bar{3}1 \end{aligned} \tag{3.148}$$

and

$$R_{\mathrm{p}}\bar{R}_{\mathrm{p}} = \bar{2}4\bar{2}3\bar{1}2\bar{4}2\bar{3}1\bar{2}4\bar{2}3\bar{1}2\bar{4}2\bar{3}\bar{1}. \tag{3.149}$$

The composite pulse given in [3.146] is the primitive element for the WALTZ family of decoupling sequences (*67*). Equation [3.147] is the WALTZ-4 sequence and [3.149] is the WALTZ-8 sequence. The WALTZ-16 sequence is obtained by a cyclic permutation of [3.149] from right to left,

$$R\bar{R}\bar{R}R = \bar{3}4\bar{2}3\bar{1}2\bar{4}2\bar{3}\ 3\bar{4}2\bar{3}1\bar{2}4\bar{2}3\ 3\bar{4}2\bar{3}1\bar{2}4\bar{2}3\ \bar{3}4\bar{2}3\bar{1}2\bar{4}2\bar{3}. \tag{3.150}$$

Each expansion of the basic element results in an improvement in the decoupling efficiency by approximately an order of magnitude. Even though the expanded sequences are significantly longer in duration than is the primitive element, fortunately the basic condition for decoupling

requires only that the primitive element be repeated rapidly compared to the coupling constant J_{IS}. The decoupling scaling factors for the WALTZ family of decoupling sequences are shown in Fig. 3.28. WALTZ-16 yields $\lambda_c < 0.0006$ for resonance offsets $|\Omega/(\gamma B_1)| \leq 1$, an improvement of three orders of magnitude compared with continuous-wave decoupling.

The search for new decoupling sequences at present is heavily dependent on computer optimization. An early example of this approach led to the GARP-1 decoupling sequence (*68*), $RR\bar{R}\bar{R}$, in which the element R is given by

$$R = 30.5\ \overline{55.2}\ 257.8\ \overline{268.3}\ 69.3\ \overline{62.2}\ 85.0\ \overline{91.8}\ 134.5\ \overline{256.1}\ 66.4\ \overline{45.9}\ 25.5$$
$$\overline{72.7}\ 119.5\ \overline{138.2}\ 258.4\ \overline{64.9}\ 70.9\ \overline{77.2}\ 98.2\ \overline{133.6}\ 255.9\ \overline{65.5}\ 53.4. \quad [3.151]$$

The pulse lengths are given in degrees and overbars indicate 180° phase shifts. GARP-1 yields $\lambda_c < 0.002$ for resonance offsets $|\Omega/(\gamma B_1)| \leq 2.5$. The decoupling scaling factor for the GARP-1 decoupling sequence is shown in Fig. 3.29a.

The WALTZ-16 and GARP-1 sequences are two of the most commonly used techniques for spin decoupling in macromolecules. However, the design of decoupling sequences has been an active area of development, and a number of alternatives have been proposed. For example, in the SUSAN-1 sequence (*69*), the composite pulse element R is given by

$$R = 27.7\ \ \overline{59.7}\ \ 37.6\ \ \overline{17.7}\ \ 41.1\ \ \overline{80.0}\ \ 43.7\ \ \overline{34.3}\ \ 68.1\ \ \overline{81.7}\ \ 60.5$$
$$\overline{49.3}\ \ 0.1\ \ \overline{37.1}\ \ 110.3\ \ \overline{163.4}\ \ 66.2\ \ \overline{110.5}\ \ 0.81\ \ \overline{145.5}\ \ 148.0, \quad [3.152]$$

and it, along with its phase-inverted counterpart $\bar{R}$, is incorporated into the MLEV-16 supercycle $\{RR\bar{R}\bar{R}\ \bar{R}RR\bar{R}\ \bar{R}\bar{R}RR\ R\bar{R}\bar{R}R\}$. The scaling factor for SUSAN-1 is shown in Fig. 3.29b, where it exhibits a somewhat broader bandwidth compared to GARP-1; SUSAN-1 provides a scaling factor $\lambda_c < 0.007$ for $|\Omega/(\gamma B_1)| \leq 3.1$, and is compensated for rf inhomogeneity over a range of $\pm 0.1(\gamma B_1)$.

When comparing scaling factors for various decoupling sequences, the results depend heavily on the type and length of the supercycles employed. In addition to the MLEV-type supercycles described here, another scheme that has proved to be very effective is the five-step cycle

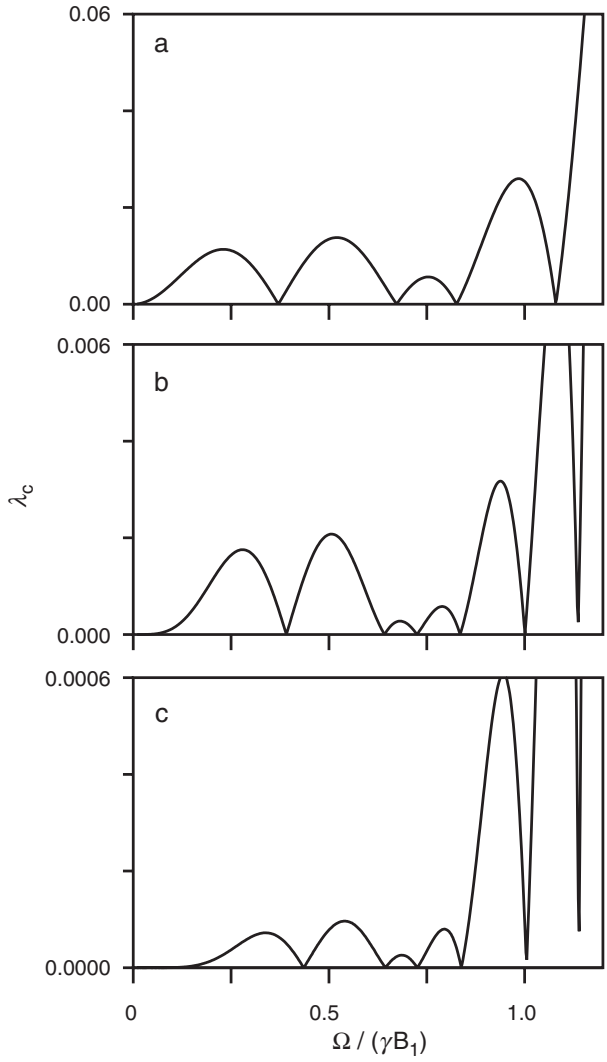

FIGURE 3.28 Scalar coupling scaling factor for (a) WALTZ-4, (b) WALTZ-8, and (c) WALTZ-16 decoupling sequences.

of the general form $[0, \phi_2, 2\phi_2 + 120^\circ, 3\phi_2 + 60^\circ, 4\phi_2 + 120^\circ]$ (*70*). The composite pulse sequence consists of the concatenation of five primitive R pulse sequence elements, with the phases of all pulses in the second element being incremented by an amount ϕ_2, the third element

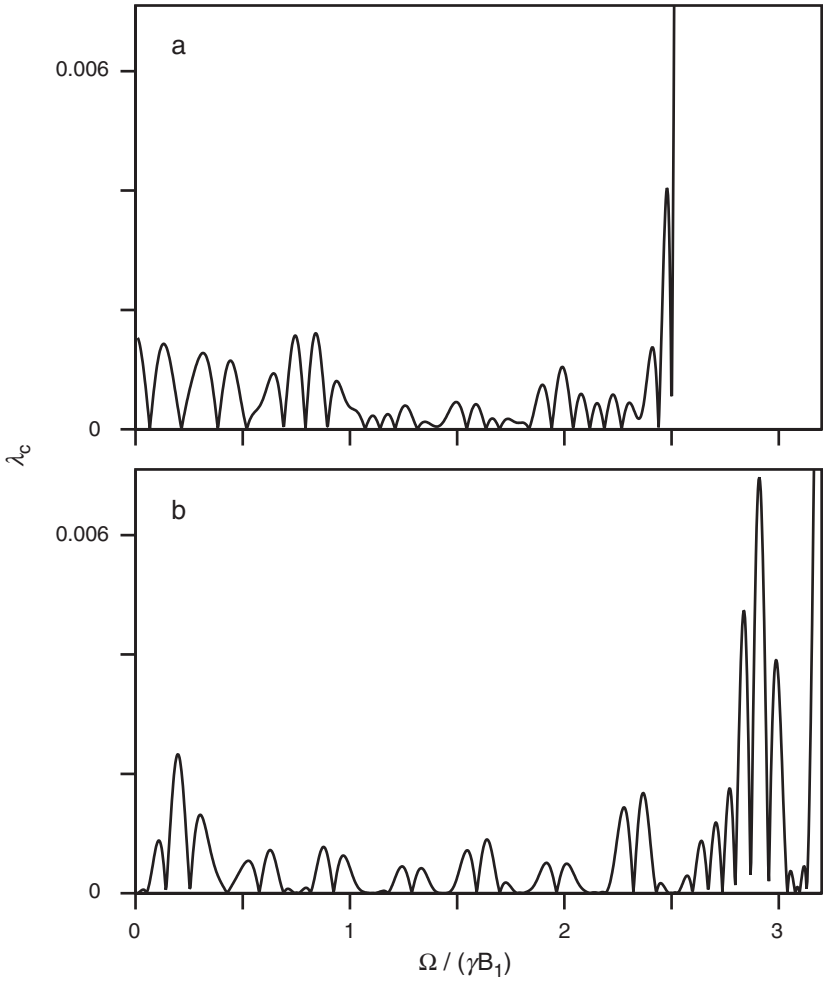

FIGURE 3.29 Scalar coupling scaling factor for (a) GARP-1 and (b) SUSAN-1 decoupling sequences.

incremented by $2\phi_2 + 120^\circ$, and so on. A specific set of phases commonly employed in practice is [0°, 150°, 60°, 150°, 0°], called the Tycko 5-step phase cycle. This phase cycle works well to improve the inversion performance of composite 180° pulses. Very often, a combination of the Tycko 5-step cycling with the MLEV-type cycling leads to improved decoupling performance, where the 5-step cycle is applied first and then the MLEV cycling is applied subsequently; this

is sometimes referred to as a T5M4 supercycle, in the case where MLEV-4 cycling ($RR\bar{R}\bar{R}$) is employed.

An example of the use of the T5M4-type phase cycling for improving decoupling performance is the MPF family of sequences (*71*), where M refers to the MLEV supercycle, P to the 5-step Tycko cycle, and F to frequency-switched pulses. A distinctive design feature of this family is the use of coherent frequency switching in the optimization of broadband inversion composite pulses. For example, one family member consists of composite pulses containing seven rectangular pulses, with flip angles of 168°, 190°, 192°, 174°, 192°, 190°, and 168°, applied at offset frequencies of −4.27, −2.71, −1.37, 0.0, 1.37, 2.71, and 4.27, respectively, in units of γB_1, the rf field strength of the pulses. The inversion performance of this sequence is improved significantly by application of the Tycko 5-step phase cycle. Adding a 4-step MLEV cycle leads to a decoupling sequence with a notable improvement in bandwidth, $|\Omega/(\gamma B_1)| \leq 4.6$, compared to WALTZ-16, GARP-1, and SUSAN-1. This decoupling sequence is referred to as MPF7 (7 refers to the number of pulses in the primitive sequence). The scaling factor for MPF7 is shown in Fig. 3.30a. Another member of the MPF family of sequences is MPF9, which employs nine pulses in the primitive element; the improvement in bandwidth is shown in Fig. 3.30b.

3.5.3 ADIABATIC SPIN DECOUPLING

As developments in magnet technology have allowed progressively higher NMR resonance frequencies to be achieved, the demands on the performance of spin decoupling sequences have also increased. For example, increasing the ^{1}H resonance frequency from 500 to 900 MHz results in the requirement for an increase in rf power of a factor of $(900/500)^2 = 3.24$ to maintain equivalent decoupling performance using any of the sequences previously described. Sample heating becomes an increasingly serious problem at high magnetic fields and the conventional hard-pulse methods approach their practical limits. Decoupling sequences that are based on adiabatic inversion pulses are an approach to overcome this limitation. Adiabatic rapid passage represents a way to achieve spin inversion completely different from the composite pulse techniques employed in the WALTZ, GARP, and other conventional spin decoupling sequences, and allows rf power to be used more efficiently. Once a suitable, adiabatic inversion pulse has been chosen, a broadband decoupling sequence can be constructed via the use of the same phase cycles and supercycles already presented.

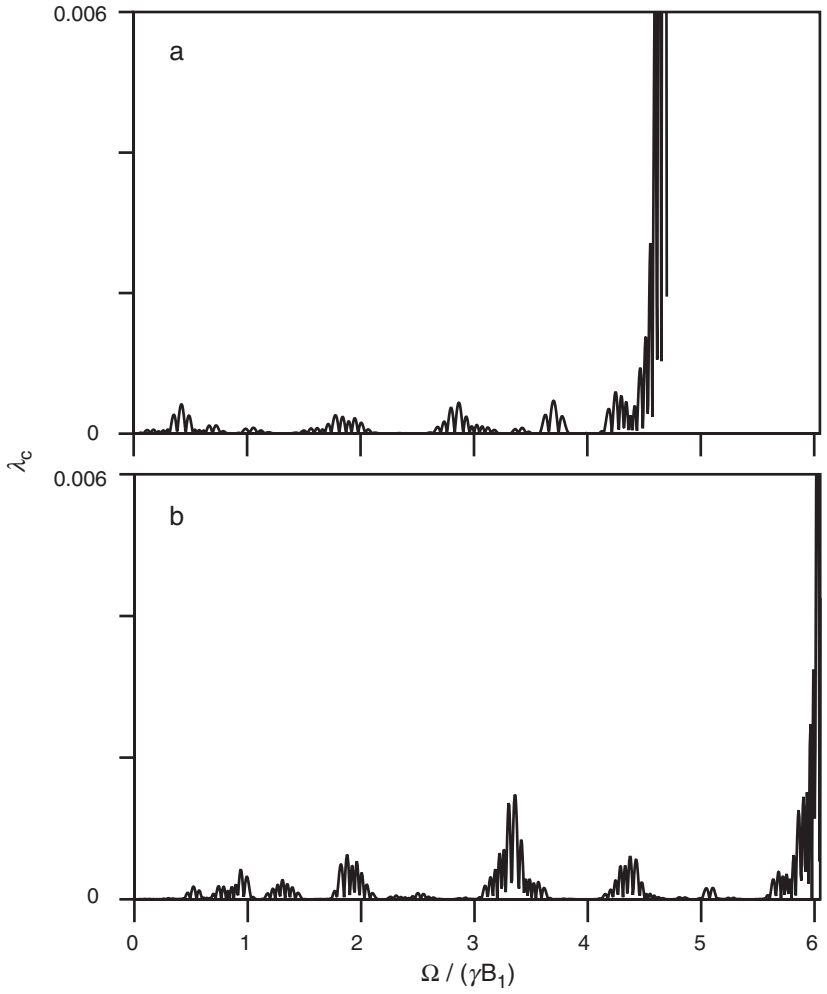

FIGURE 3.30 Scalar coupling scaling factor for (a) MPF-7 and (b) MPF-9 decoupling sequences.

Several different decoupling schemes based on different adiabatic inversion pulses have been described. The simplest sequence uses the CHIRP pulse, which consists simply of a linear frequency sweep of the decoupling rf field. An effective decoupling sequence based on this simple pulse is known as CHIRP-95 (*72*). The adiabatic condition [3.122] typically is violated at the beginning and end of the CHIRP pulse, because sudden switching of the rf field on or off means that the nuclear

magnetization vector does not begin or end in perfect alignment with the effective field. An 80-step phase cycle (5-step Tycko sequence × 16-step MLEV supercycle) is quite effective in minimizing the deleterious effects caused by violations of the adiabatic condition. A more complex alternative to the CHIRP pulse is the so-called hyperbolic secant pulse, in which the pulse amplitude and frequency modulation functions are given by [3.135]. Such a pulse is attractive due to its excellent inversion profile. A prominent decoupling sequence based on the hyperbolic secant pulse [3.135] is known as STUD (*73*). A significant drawback to this approach is the very high peak rf field amplitude necessary for the hyperbolic secant pulse, which leads to a risk in causing arcing in probe circuitry, especially with cryogenically cooled probes.

The so-called WURST decoupling sequences provide a popular and practical compromise approach (*58*). The WURST adiabatic pulse uses a linear frequency sweep and an amplitude modulation function given in [3.136]. The effective decoupling bandwidth, ΔF^*, of a WURST sequence is related to the sweep width by the quality factor ξ, where $\xi = \Delta F^*/\Delta F$; the value of ξ is dependent on the index n in the WURST shape function, and typically is in the range 0.6–0.9, as determined from theoretical simulations. Inserting the quality factor into [3.139] results in the following expression for the effective decoupling bandwidth

$$\Delta F^* = \frac{\xi(\gamma B_1)^2 \tau_p}{2\pi Q_0}. \qquad [3.153]$$

This equation shows the key result that the effective bandwidth of an adiabatic decoupling sequence is proportional to the *square* of the applied rf field strength, as opposed to the linear relationship that holds for other methods, such as composite pulse decoupling. The quadratic dependence on the rf field strength is the reason for the high efficiency of adiabatic decoupling sequences. The bandwidth also depends inversely on the adiabaticity factor Q_0, and linearly on the primitive pulse length τ_p. Increased bandwidths can be obtained by pushing the lower limit of $Q_0 = 1$ and lengthening the pulse duration. However, effective decoupling also requires $\tau_p < 1/J_{IS}$, where J_{IS} is the size of the relevant scalar coupling, and minimizing τ_p also is important for reducing cycling sidebands. As with all decoupling sequences, the use of phase cycles and supercycles significantly enhances the decoupling performance of WURST-based sequences. The Tycko 5-step cycle nested inside an MLEV-4 cycle works well.

Unlike composite pulse decoupling sequences, in which the only adjustable experimental parameter is the value of the rf field strength B_1,

the decoupling performance of a WURST sequence will depend on the choice of experimental parameters $\{Q_0, \tau_p, n, B_1, \Delta F\}$, and can be tailored to satisfy the requirements of a particular application. For example, extremely wide decoupling bandwidths can be achieved by minimizing Q_0 and maximizing τ_p and B_1 within practical limits, at the expense of increased cycling sidebands; alternatively, cycling sidebands can be minimized by shortening the pulse length τ_p, at the expense of reduced bandwidth. Based on the maximum value of the scalar coupling constant J_{IS} of interest, the pulse duration is chosen to satisfy the condition $\tau_p < 1/J_{IS}$. Increasing the factor $\left(\tau_p J_{IS}\right)^{-1}$ reduces the size of the cycling sidebands, while reducing this factor, by maximizing τ_p, increases the decoupling bandwidth. After choosing the adiabaticity factor Q_0 and rf field strength, ΔF is determined using [3.139] and the index n is chosen using the rule of thumb $n = \tau_p \Delta F/2$. The linear frequency sweep is conveniently generated by a phase modulation of the WURST pulse, as discussed in Section 3.4.5, and the amplitude is modulated according to [3.136].

Plots of the scaling factors for a typical WURST decoupling sequence are shown in Fig. 3.31; the parameters defining the WURST sequence are given in the figure caption. Unlike the plots of scaling factors shown in Figures 3.28–3.30, the scaling factors for the WURST sequence are plotted as a function of the absolute, rather than relative, resonance offset frequency, because the relationship between the decoupling bandwidth and the rf field strength γB_1 is not simply linear for adiabatic decoupling. The scaling factor shown in Fig. 3.31a corresponds to a WURST sequence generated using an adiabaticity factor $Q_0 = 1.2$, near the limit at which the sequence can be considered to be adiabatic. By increasing the rf field strength modestly, such that $Q_0 = 1.5$, the scaling factor is significantly improved, as shown in Fig. 3.31b. These results appear to suggest that, if only a modest bandwidth needs to be decoupled, an adiabatic sequence could be used with a very low rf field strength to minimize rf heating. However, this scheme does not work, because the adiabatic condition cannot be maintained with arbitrarily weak rf fields. The practical limit corresponds roughly to a 2-kHz rf field: above this, adiabatic sequences work well, while below this boundary, composite pulse schemes are advisable.

3.5.4 CYCLING SIDEBANDS

Although the achievable bandwidth for a given decoupler rf field strength is an important criterion in choosing a decoupling sequence, all decoupling sequences generate cycling sidebands, due to

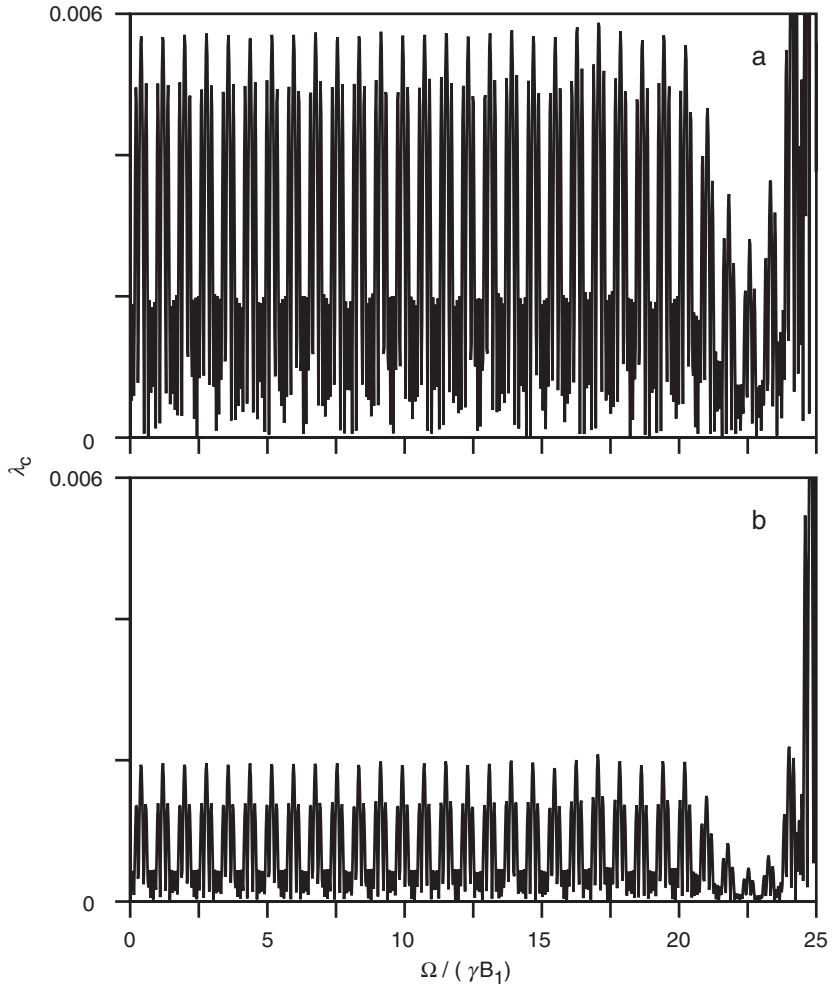

FIGURE 3.31 Scalar coupling scaling factors for a WURST-40 decoupling sequence, composed of a WURST pulse calculated with a pulse length of 1.25 ms and a frequency sweep of 64 kHz, and assembled into a T5M4 supercycle. (a) The rf field strength of 3.127 kHz, corresponding to an adiabicity factor $Q_0 = 1.2$. (b) The rf field strength of 3.5 kHz, corresponding to $Q_0 = 1.5$.

nonstroboscopic sampling of the FID relative to the decoupling sequence, and minimizing cycling sidebands also is an important criterion. Figures 3.32–3.34 show typical cycling sideband patterns for the decoupling sequences discussed in the preceding sections. Over its

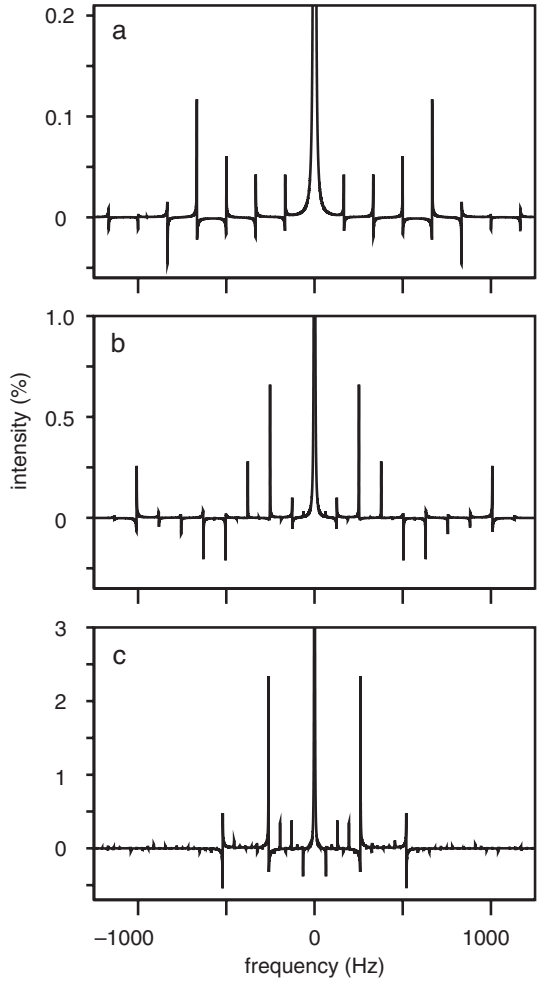

FIGURE 3.32 Numerical simulations showing the cycling sidebands for (a) WALTZ-16, (b) GARP-1, and (c) SUSAN-1 decoupling sequences. In each case, the rf field strength was $\omega_1/2\pi = 2$ kHz and the decoupler transmitter was placed 500 Hz away from the heteronuclear resonance frequency. The simulations were performed for an *IS* spin system and a scalar coupling of $J_{IS} = 221$ Hz, using the COMPUTE procedure (*122*).

bandwidth, WALTZ-16 clearly provides the minimum sideband intensity. Comparison of GARP-1 versus SUSAN-1, shown in Fig. 3.32, indicates that the increase in bandwidth of SUSAN-1 over GARP-1 comes at the expense of a significant increase in sideband

intensity. As a general rule, shorter decoupling sequences generate smaller cycling sidebands. This principle is illustrated in Fig. 3.33, where Fig. 3.33a shows the cycling pattern for MPF7 using a 2-kHz rf field,

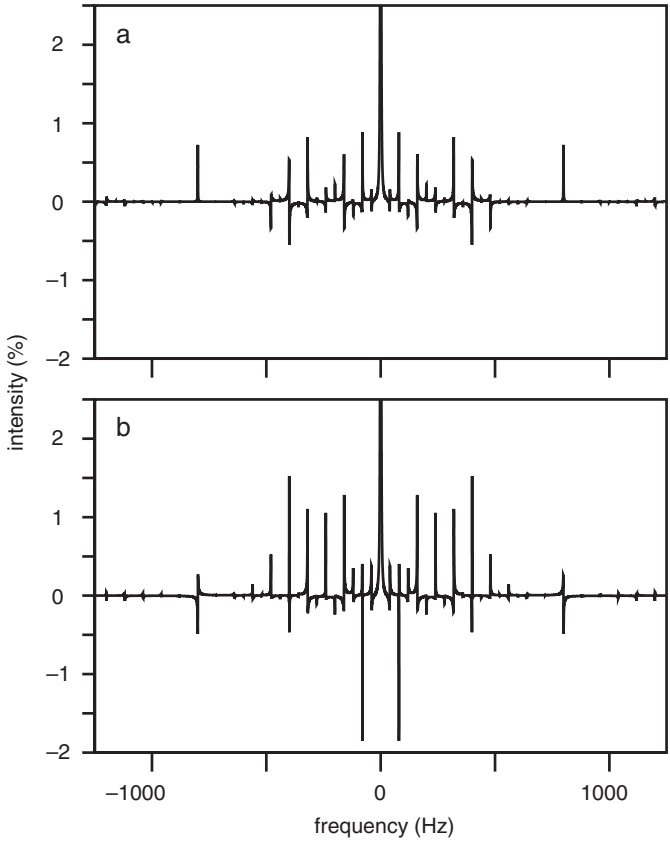

FIGURE 3.34 Cycling sidebands are shown for (a) WURST decoupling with a root-mean-square (rms) field strength of $\omega_1/2\pi = 2.0\,\text{kHz}$ and a resonance offset of 500 Hz, and (b) WURST decoupling with an rms field strength of $\omega_1/2\pi = 2.0\,\text{kHz}$ and a resonance offset of 20 kHz.

offset is demonstrated by comparing Figs. 3.34a, calculated for a resonance offset of 500 Hz, and 3.34b, calculated for a resonance offset of 20 kHz.

3.5.5 RECOMMENDATIONS FOR SPIN DECOUPLING

A general conclusion of the decoupling discussion is that no "best" spin decoupling sequence exists; rather, decoupling sequences should be chosen to match the requirements of a given application. For example,

for the modest bandwidth of backbone ^{15}N nuclei in proteins, the WALTZ-16 or GARP-1 sequence is perfectly suitable, even on 900-MHz spectrometers. GARP-1 is also quite useful for decoupling ^{13}C if minimizing cycling sidebands over a limited range of the full ^{13}C bandwidth is desired. For broader decoupling requirements, selection of an adiabatic sequence is appropriate, with the compromise between bandwidth and sideband intensity being taken into account when choosing the parameters for the adiabatic sequence.

Some applications require good decoupling performance over a specified frequency bandwidth with minimal perturbation of spins resonating outside the chosen range. Decoupling ^{13}CO and $^{13}C^{\alpha}$ spins from each other is the most common application in protein NMR spectroscopy. Suitable families of decoupling sequences have been developed in which the rf field is windowed or in which the amplitude and phase of the rf field are modulated to obtain the desired selectivity. For example, the SEDUCE-1 selective decoupling sequence is obtained by replacing each rectangular pulse in the WALTZ-16 pulse sequence with the SEDUCE-1 amplitude-modulated selective pulse, described in Section 3.4.4 (*74*).

Incidentally, spin decoupling is somewhat related to the problem of obtaining an isotropic effective Hamiltonian for generating Total Correlation Spectroscopy (TOCSY) coherence transfer via strong coupling. These applications are discussed in Section 4.2.1.2.

3.6 B_0 Field Gradients

The development of actively shielded probes that can produce high-power field gradient pulses has resulted in new classes of experiments that utilize field gradients for coherence selection, for water suppression, and for mitigation of radiation damping effects. For many years, the disadvantage of using field gradient pulses was that the strong field gradients required disturbed the field frequency lock. However, with the advent of gradient coils that are actively shielded and with advances in lock blanking methods, these problems have been overcome. This section describes basic aspects of field gradient pulses. Applications in solvent suppression are discussed in Section 3.5. Applications in coherence selection, artifact suppression, and frequency discrimination are described in Section 4.3.3.

A field gradient pulse is a time period during which the B_0 field is made deliberately inhomogeneous. In the simplest and most common application, the B_0 field is varied linearly in the z-direction.

Conceptually, the NMR sample can be envisaged as a column of thin slices (called *isochromats*) along the z-direction. The spins in each slice experience different magnetic fields and thus different Larmor resonance frequencies. Initially, the spins in each isochromat are phase coherent. As the gradient is applied, the phase coherence between slices is lost due to Larmor precession. After a sufficiently long time, complete dephasing occurs and the net magnetization of the sample becomes zero. The dephasing process caused by the gradient pulse results because the coherences acquire *spatially dependent phase*. However, the coherence can be refocused by another appropriately applied gradient to generate gradient echoes (*75*).

More formally, the magnetic field produced by the gradient pulse, $B_g(z)$ varies linearly along the z-axis, and can be written

$$B_g(z) = zG_z, \qquad [3.154]$$

where G_z is the gradient strength given in T/m or, more usually, G/cm. With the origin of the z-axis being taken as the center of the sample, the Larmor frequency at any point in the sample, $\omega(z)$, is given by

$$\omega(z) = -\gamma\big[B_0 + B_g(z)\big] = -\gamma[B_0 + zG_z] = \omega_0 - \gamma z G_z. \qquad [3.155]$$

In the rotating frame, the ω_0 term vanishes. If the gradient is applied for a time t, then the *spatially dependent phase* at any position in the sample, $\phi(z)$, is given by

$$\phi(z) = \gamma z G_z t. \qquad [3.156]$$

Consider the case of applying a gradient pulse of strength G_z for a time t to a system consisting of in-phase single-quantum coherence, e.g., I_x. At any point in the sample the evolution of I_x is given by

$$I_x \xrightarrow{-\gamma z G_z t I_z} \cos(\gamma z G_z t) I_x - \sin(\gamma z G_z t) I_y. \qquad [3.157]$$

The net x-magnetization across the whole sample is determined by summing (integrating) over all the slices through the sample:

$$M_x(t) = \frac{1}{r_{\max}} \int_{-r_{\max/2}}^{r_{\max/2}} \cos(\gamma z G_z t)\, dz = \frac{2\sin(\gamma G_z t r_{\max}/2)}{\gamma G_z t r_{\max}} = \operatorname{sinc}(\gamma G_z t r_{\max}/2), \qquad [3.158]$$

where the sample extends over a region $\pm r_{\max}/2$. This equation represents the decay of the x-magnetization oscillations during the

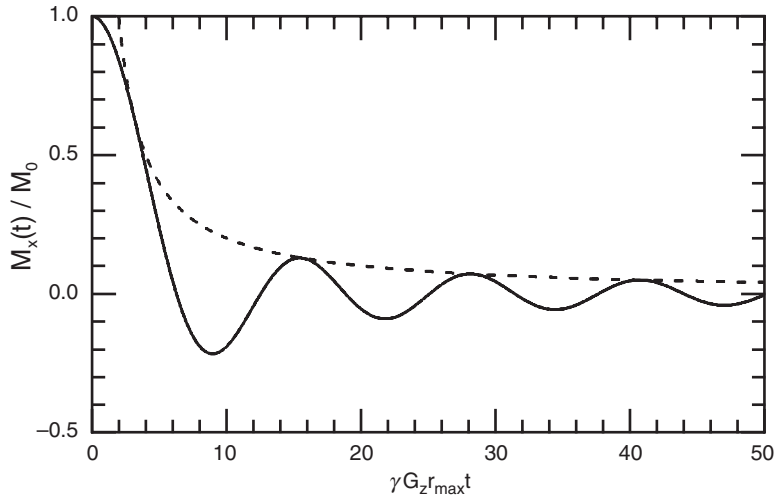

FIGURE 3.35 Dephasing of transverse magnetization by pulsed field gradients. The relative amplitude of transverse magnetization is plotted versus $\gamma G r_{\max} t$ to show the effect of applying a pulsed field gradient in the z-direction to transverse magnetization. The solid line represents decay of the oscillatory signal according to [3.158]. The dotted line shows the asymptotic decay $M_x(t)/M_0 = 2/(\gamma G r_{\max} t)$.

gradient pulse. First and most obviously, [3.158] demonstrates that application of a stronger gradient causes the magnetization to decay at a faster rate. Second, [3.158] shows that magnetization from nuclei with higher magnetogyric ratios decays faster. In addition, the strengths of gradients required to suppress coherences to a defined level can be estimated. Figure 3.35 shows a plot of $M_x(t)$ versus $\gamma G r_{\max} t$ for this equation. The overall decay for long times is given by $2/(\gamma G r_{\max} t)$. For example, in the case just noted, the amount of x-magnetization will have decayed to a fraction α of its initial value after a time of the order $2/(\gamma G r_{\max} \alpha)$. Consequently, if the requirement was to suppress ^{1}H x-magnetization to 1/1000th of its original value, then a gradient pulse of 2.5 ms with strength 30 G/cm (0.3 T/m) over a sample region $r_{\max} = 1$ cm would be sufficient. Of course, this is an idealized calculation and, in practice, fine tuning of the duration and the gradient strength is always required.

Practically, field gradients can be generated in two ways. First, the shim coils can be used to produce a spatially inhomogeneous field, but this method only produces gradient amplitudes of $\sim$1 G/cm.

Gradients produced with the shim coils are called *homospoil pulses*. Second, and much more preferable, specialized actively shielded gradient coils can be built directly into a high-resolution NMR probe. Gradients of the strengths previously noted are easily obtainable by this setup. Probe manufacturers now also offer the option of three-axis gradient systems containing three coils that can apply simultaneous gradients along the *x*-, *y*-, and *z*-directions. Importantly, an *x*- or *y*-gradient refers to a magnetic field in the *z*-direction whose magnitude depends linearly on the *x*- or *y*-position in the sample. Dephasing of magnetization by three orthogonal gradients is more rapid than for a single *z*-gradient, although the efficacy of the orthogonal gradients depends on the sample geometry. For a rectangular solid geometry, dephasing depends on the function $1/(\gamma^3 G_x G_y G_z V t^3)$, where G_i is the strength of the gradient in direction i and V is the sample volume. Other sample geometries and nonideal effects not considered in this text have been discussed by Kingsley (*76*).

Field gradient pulses also can be applied with an amplitude envelope that is a smooth function of time, rather than rectangular. A rectangular field gradient pulse has infinite slope at time zero and induces currents that generate torque on the gradient coils. If the gradient pulse is strong enough, then the gradient coils can be damaged physically. Shaped field gradient pulses reduce the induced currents and torques on the gradient coils. Generalizing the preceding discussion to include shaped three-axis field gradient pulses, the spatially dependent phase generated by a shaped gradient pulse of duration t applied to a (possibly multiple-spin heteronuclear) coherence is

$$\phi(r, t) = sB_g(r)t \sum_i p_i \gamma_i, \qquad [3.159]$$

in which γ_i, and p_i are the gyromagnetic ratios and coherence level of each nuclear species, i, contributing to the coherence. The shape factor, s, is defined as

$$s = \frac{1}{t} \int_0^t A(t)\, dt, \qquad [3.160]$$

in which the amplitude profile of the gradient pulse is given by $|A(t)| \leq 1$. Opposing gradients, i.e., those that either increase or decrease as the *z*-coordinate increases, have values of s that are opposite in sign. The overall amplitude of the gradient at a point $\boldsymbol{r} = (x, y, z)$ is represented

by $B_g(\boldsymbol{r})$. For convenience, the dependence of ϕ on ($\boldsymbol{r}$, t) and B_g on $\boldsymbol{r}$ will be implied in the following discussion.

A magic-angle gradient pulse has gradient strengths adjusted such that $G_z^2 = (G_x^2 + G_y^2)/2$ and the effective gradient direction makes an angle with respect to the z-axis of $\theta = 54.7^\circ$, the magic angle. Such gradients are useful in suppressing effects of the dipolar demagnetizing field, which result from the interaction between the strong water magnetization and the B_0 field (*77, 78*), and provide superior water suppression in certain NMR experiments (*79, 80*). The multiple-quantum echo (also called the multiple-spin echo) signal is observable in a sample prepared in H_2O using the pulse sequence

$$90^\circ_x - G_1 - 90^\circ_x - G_2 - \text{acquire}, \qquad [3.161]$$

in which $G_{2\zeta} = 2G_{1\zeta}$ for $\zeta = \{x, y, z\}$ and the total gradient strength is given by $G_a = (G_{ax}^2 + G_{ay}^2 + G_{ax}^2)^{1/2}$ for $a = \{1, 2\}$. The intensity of the multiple-quantum echo signal obtained from this sequence is proportional to $(3\cos^2\theta - 1)/2$. Thus, a magic-angle gradient can be calibrated by using this same pulse sequence (*80*). An initial spectrum is acquired with G_1 and G_2 set to the desired values, but with the z-gradients equal to zero. Normally, the x- and y-gradients are set nominally equal to each other for convenience, although this is not essential. Next the magnitudes of the x-, y-, and z-gradients are adjusted, while keeping the total gradient strengths G_1 and G_2 constant, until the multiple-quantum signal is nulled. The resulting values of the gradients satisfy the magic-angle condition. This procedure also provides a simple method for calibrating the z-axis gradient strength relative to the x- or y-gradient strength (*80*).

3.7 Water Suppression Techniques

An overwhelming majority of the studies of biological macromolecules using high-resolution NMR spectroscopy are performed in aqueous solutions. The concentration of ^1H nuclei in water is approximately 110 M, in contrast to typical concentrations of macromolecules of 0.1–2 mM. Thus, the equilibrium magnetization of the water ^1H spins is approximately 10^4–10^5 greater than is the equilibrium magnetization of a single ^1H spin in a macromolecule. Detection of the solute signal in the presence of the solvent signal presents a difficult problem because, inevitably, the dynamic range of the electronic components of the spectrometer is limited. If, for example, the signal

from a 1 mM protein solution is to be digitized with 4-bit precision utilizing a 16-bit analog-to-digital converter, then the water signal must be reduced by at least a factor of 50 prior to acquisition to avoid overflowing the receiver ADC. In addition, even if the water and solute signal are digitized adequately, the solute resonances may be obscured by the tails of the large, broad solvent peak. This problem is particularly severe for multidimensional spectra in which changes in the phase of the solvent signal from experiment to experiment lead to severe distortions of the final spectrum.

NMR spectroscopy in aqueous solution also suffers from *radiation damping* of the solvent signal (*81, 82*). Following an rf pulse, the water magnetization precesses in the transverse plane and induces a time-varying oscillating current in the coil. The current, in turn, induces an electromagnetic field of the same frequency that acts to rotate the water magnetization back toward the $+z$-axis. Following a 90° pulse, the time constant for radiation damping is given approximately by (*81*)

$$\tau_{RD} = (2\pi M_0 Q\gamma)^{-1}. \qquad [3.162]$$

Thus, radiation damping is important for the water magnetization, and not directly for the solute magnetization, because the (unsuppressed) solvent magnetization is orders of magnitude larger. Although water ^{1}H spins have T_1 relaxation times of seconds, for a typical high-Q NMR probe, radiation damping following a 90° pulse will return the transverse magnetization to the $+z$-axis in tens of milliseconds or less. Radiation damping is even more severe in cryogenic probes, in which the ^{1}H coil and preamplifier are cooled to low temperatures to increase sensitivity (and thereby increase Q). Radiation damping severely interferes with the expected evolution of the water magnetization through a pulse sequence.

A straightforward method of reducing the resonance signal from H_2O is to use D_2O as the solvent. Deuterium oxide with a deuteron content of up to 99.999% is commercially available and offers theoretical reduction in the water ^{1}H signal by a factor of 10^5. The main limitation to this approach is that signals from exchangeable ^{1}H nuclei in the macromolecule are reduced as well. For example, signals from the amide groups in proteins usually are absent in spectra acquired using D_2O solutions. Because scalar coupling and dipolar interactions of the backbone amide $^1H^N$ spins with amide ^{15}N spins and with $^1H^\alpha$ spins are critical for backbone resonance assignments and secondary structure analyses (Chapter 9), at least some protein spectra must be acquired in H_2O rather than D_2O solution. A secondary problem is that inevitable

differences in sample conditions between samples in H_2O and D_2O (principally, pH differences or isotope effects) can complicate comparisons of data acquired in the two solvents. The usual course of action will be to acquire a series of experiments from H_2O solution initially (with 5–10% D_2O present for the field frequency lock system), and then to transfer the sample to D_2O for a second series of experiments. Even in D_2O solution, the HDO resonance resulting from residual ^1H spins frequently is further suppressed by one of the techniques described in the following discussions.

The general subject of solvent suppression techniques can be divided into three stages: (1) techniques for reducing the solvent signal detected during a single transient acquisition to within the dynamic range of the spectrometer, (2) techniques for further reduction of the solvent signal that results from a single, signal-averaged, experiment, and (3) postacquisition digital signal processing to improve the solvent suppression. The commonly used methods for solvent suppression (dynamic range reduction) in biological samples are (1) presaturation of the solvent resonance during the recycle delay between transient acquisitions, (2) (semi) selective excitation of macromolecule resonances, and (3) dephasing of the solvent magnetization using rf or field-spoiling pulses. Experimental techniques for solvent suppression have been reviewed (*83, 84*) and are discussed briefly in the following sections.

3.7.1 PRESATURATION

The most commonly used solvent suppression technique is presaturation of the solvent signal during the recycle delay using a weak rf field. Presaturation is very simple to implement and is very effective. The main disadvantages are that signals that resonate very close to the solvent signal (principally the $^1H^{\alpha}$ spins in proteins) may be partially saturated by the rf field and that saturation transfer may partially saturate exchangeable ^1H spins. As shown in Fig. 3.36, the rates of exchange between $^1H^N$ spins in proteins and water ^1H spins is pH dependent; accordingly, saturation transfer to the $^1H^N$ spins in proteins is particularly deleterious above pH 7. The quality of the water suppression obtained by presaturation depends very critically on the homogeneity of the magnetic field and hence on the quality of the shimming. Solvent signals originating outside of the main sample volume also degrade solvent suppression; consequently, modern probes designed for use with water solutions have rf coils with shielded leads.

Irradiation times on the order of 1–2 s using rf fields with amplitudes of approximately 50 Hz usually provide adequate water suppression.

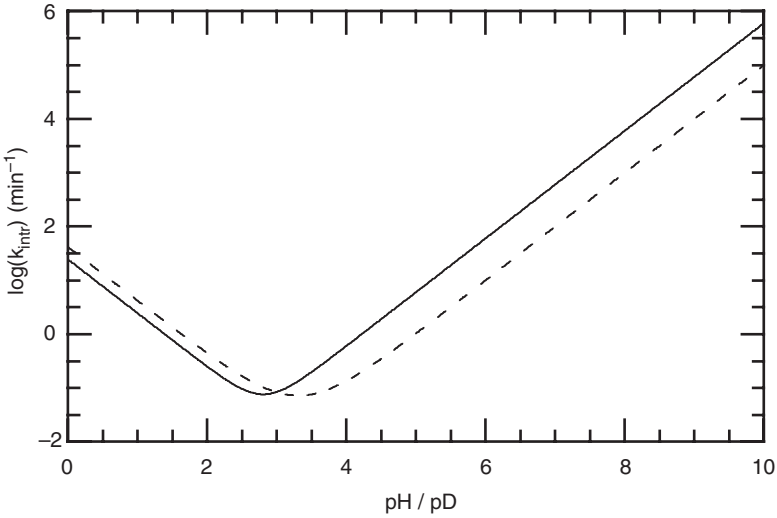

FIGURE 3.36 Intrinsic backbone H^N exchange rates (*123*). The intrinsic exchange rate, k_{intr}, is shown for exchange of a backbone H^N with (—) H_2O or (- - -) D_2O as a function of pH or pD. The pD values are corrected for isotope effects; uncorrected pH meter readings would be 0.4 units smaller.

Short irradiation times minimize the effects of saturation transfer, but require higher power rf fields and worsen saturation of signals resonating near the irradiation frequency. For each new sample, the shimming, irradiation frequency, and irradiation power must be adjusted to optimize water suppression.

3.7.2 JUMP–RETURN AND BINOMIAL SEQUENCES

A variety of techniques have been developed that selectively excite the resonances from the solute while leaving equilibrium magnetization of the water ^1H spins relatively undisturbed. Of these techniques, only the $1\text{–}\bar{1}$ "jump–return" and $1\text{–}\bar{3}\text{–}3\text{–}\bar{1}$ binomial sequence have achieved much popularity for protein NMR spectroscopy (*85, 86*). These techniques can be incorporated into Nuclear Overhauser Effect Spectroscopy (NOESY) pulse sequences in order to observe cross-relaxation between ^1H nuclei that exchange rapidly with solvent.

In the jump–return technique, the final read pulse in a pulse sequence is replaced by the pulse element $90_x\text{–}\tau\text{–}90_{-x}$. The carrier is

placed on the solvent resonance and $\tau = 1/(4\Delta\nu_{\max})$, in which $\Delta\nu_{\max}$ is the offset from the carrier at which excitation is maximized. Jump–return and binomial sequences provide nice illustrations of the technique of [2.121] in the analysis of propagators. For the jump–return sequence, the propagator is given by

$$\begin{aligned}\mathbf{U} &= \exp[i(\pi/2)I_x]\ \exp[-i\Omega\tau I_z]\ \exp[-i(\pi/2)I_x] \\ &= \exp\left[-i\Omega\tau e^{i(\pi/2)I_x} I_z e^{-i(\pi/2)I_x}\right] \\ &= \exp\left[-i\Omega\tau I_y\right],\end{aligned}$$

in which the final two lines are obtained by applying [2.121]. Evolution during the jump–return element is given by

$$I_z \xrightarrow{\Omega\tau I_y} I_z\cos(\Omega\tau) + I_x\sin(\Omega\tau). \qquad [3.164]$$

The resonance offset of the solvent ^{1}H spins is zero because the rf carrier is placed on the solvent resonance. No transverse solvent magnetization is generated and, in theory, complete suppression of the solvent signal is obtained. The amplitude of the detected signal for coherences that are not resonant with the rf carrier is proportional to I_x and depends upon the delay τ through the factor $\sin(\Omega\tau)$. The spectrum that results has opposite phase above and below the carrier position because the sine is an odd function; however, no linear phase correction is required.

In the $1-\bar{3}-3-\bar{1}$ technique, the read pulse is replaced by the pulse element $\alpha_x-\tau-3\alpha_{-x}-\tau-3\alpha_x-\tau-\alpha_{-x}$, in which $8\alpha = 90^\circ$ and $\tau = 1/(2\Delta\nu_{\max})$. The propagator is

$$\begin{aligned}\mathbf{U} = {} & \exp[i\alpha I_x]\exp[-i\Omega\tau I_z]\exp[-i3\alpha I_x]\exp[-i\Omega\tau I_z]\exp[i3\alpha I_x] \\ & \times \exp[-i\Omega\tau I_z]\exp[-i\alpha I_x].\end{aligned} \qquad [3.165]$$

Clearly, for $\Omega = 0$, $\mathbf{U} = \mathbf{E}$ and no transverse magnetization is generated. The $1-\bar{3}-3-\bar{1}$ sequence offers better theoretical suppression of the solvent resonance than the jump–return sequence. The evolution of the density operator for coherences that are not resonant with the rf carrier is quite complicated; for simplicity, consider only the offset at which maximum excitation occurs. In this case, $\Omega\tau = \pi$ and the propagator is

given by

$$\begin{aligned}\mathbf{U} &= \exp[i\alpha I_x]\exp[-i\pi I_z]\exp[-i3\alpha I_x]\exp[-i\pi I_z]\exp[i3\alpha I_x] \\ &\quad \times \exp[-i\pi I_z]\exp[-i\alpha I_x] \\ &= \exp[i\alpha I_x]\exp\left[-i3\alpha e^{-i\pi I_z} I_x e^{i\pi I_z}\right]\exp\left[i3\alpha e^{-i2\pi I_z} I_x e^{i2\pi I_z}\right] \\ &\quad \times \exp\left[-i\alpha e^{-i3\pi I_z} I_x e^{i3\pi I_z}\right]\exp[-i3\pi I_z] \\ &= \exp[i\alpha I_x]\exp[i3\alpha I_x]\exp[i3\alpha I_x]\exp[i\alpha I_x]\exp[-i3\pi I_z] \\ &= \exp[i8\alpha I_x]\exp[-i3\pi I_z] \\ &= \exp[i(\pi/2)I_x]\exp[-i\pi I_z], \end{aligned} \qquad [3.166]$$

in which the last four lines are obtained by applying [2.121]. The evolution of the equilibrium density operator is given by

$$I_z \xrightarrow{\pi I_z} I_z \xrightarrow{-(\pi/2)I_x} I_y. \qquad [3.167]$$

Unfortunately, for other offsets, the amplitude of the detected signal depends upon the delay τ and a strong linear phase gradient exists across the spectrum. The linear phase gradient leads to baseline distortions that are a particular problem in multidimensional NMR spectroscopy. Consequently, the jump–return sequence has been much more widely applied in multidimensional NMR spectroscopy. Excitation profiles for the jump–return and binomial sequences are shown in Fig. 3.37.

Jump–return and binomial pulse sequences are sensitive to pulse and phase imperfections. Optimal water suppression requires careful adjustment of the spectrometer. Pulse lengths and phases usually are adjusted slightly around the theoretical values to maximize water suppression (typically by 0.1–0.3 μs and 1–3°). In practice, suppression factors of 50–100 are generally obtained and are adequate when combined with postacquisition signal processing techniques. These sequences are most successful when used as the read pulses for relatively simple experiments with few pulses and no extended rf mixing sequences, such as NOESY and Heteronuclear Multiple-Quantum Coherence (HMQC) experiments. These sequences have an advantage over presaturation and the techniques described in the following sections in that the net excitation of the water signal is zero, or nearly so. Because the water signal remains nearly at equilibrium, saturation transfer from the water to the solute is minimized.

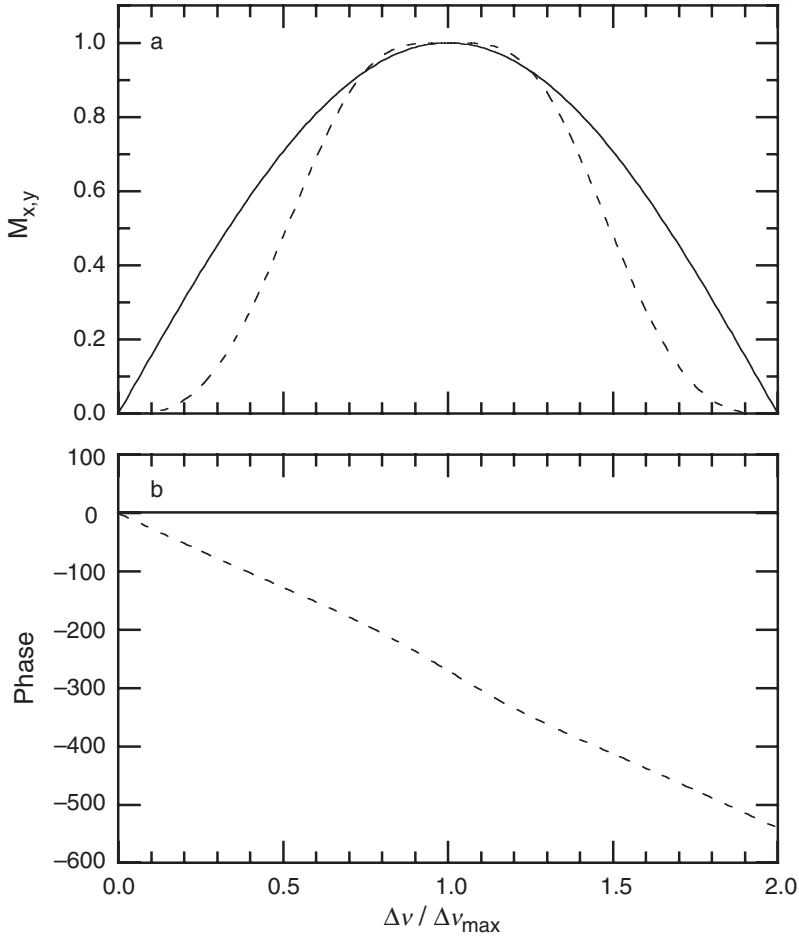

FIGURE 3.37 Binomial excitation profiles. (a) Magnitude and (b) phase of the transverse magnetization, $M_{x,y} = (M_x^2 + M_y^2)^{1/2}$ excited by the (—) jump–return and (- - -) 1 $\bar{3}$ 3 $\bar{1}$ pulse sequences are plotted as function of resonance offset. Resonances on opposite sides of the carrier have inverted phases (not shown).

3.7.3 SPIN LOCK AND FIELD GRADIENT PULSES

Recent technological advances in NMR spectrometer hardware have resulted in the development of new methods of solvent suppression using combinations of selective pulses, spin lock purge pulses, and field gradient pulses. These techniques can generate nearly ideal excitation

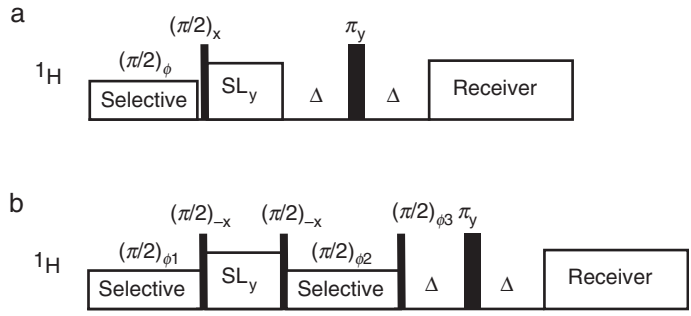

FIGURE 3.38 Water suppression using spin lock (SL) purge pulses incorporated into Hahn echo pulse sequences. Rectangular or shaped selective pulses are applied to the solvent magnetization and minimally perturb the solute magnetization. Thin and thick solid bars represent 90° and 180° nonselective pulses, respectively. SL represents a spin lock purge pulse of 1–2 ms duration. Delays (Δ) are adjusted as described in Section 3.6.4.2 for the basic Hahn echo experiment. The phase cycles are (a) $\phi = (x, -x)$, receiver $= (x, x)$; (b) $\phi_1 = (x, -x, x, -x)$, $\phi_2 = (x, x, -x, -x)$, $\phi_3 = (-x, -x, x, x)$, receiver $= (x, x, -x, -x)$. Basic phase cycles can be elaborated using CYCLOPS and EXORCYCLE as described for the Hahn echo pulse sequence in Section 3.6.4.2.

profiles with high degrees of water suppression. Large linear phase gradients are avoided and the techniques can be implemented into nearly all NMR experiments. Using these methods, the water signal can be saturated within a few milliseconds. Saturation transfer effects are much smaller than for presaturation; however, unless the recycle delay is very long, some attenuation of the water resonance and consequent saturation transfer to the solute molecule is unavoidable. In addition, techniques have been developed that attempt to maintain the water magnetization close to its equilibrium value and avoid presaturation effects as completely as possible (*87, 88*). For illustrative purposes, a variety of these water suppression techniques have been incorporated into homonuclear Hahn echo pulse sequences (Section 3.6.4.2) in Figs. 3.38 and 3.39.

For probes that lack capability to apply field gradient pulses, water suppression must be achieved using only spin lock purge pulses. In these applications, the water signal is saturated by dephasing due to B_1 rf inhomogeneity (Section 3.4.6). In the simplest approach, shown in Fig. 3.38a, a selective 90° pulse is used to rotate the water magnetization into the transverse plane. A hard (nonselective) 90° pulse rotates solute

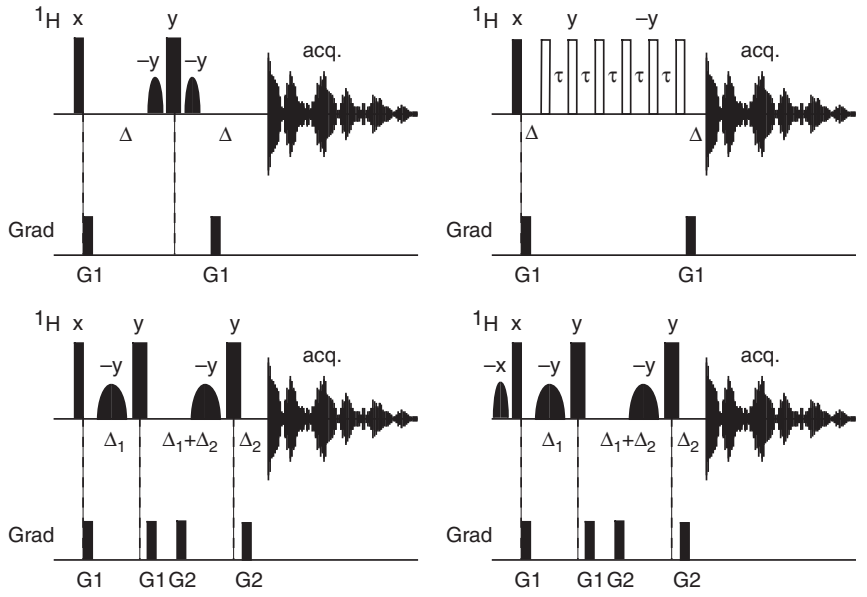

FIGURE 3.39 Water suppression using field gradient pulses incorporated into Hahn echo pulse sequences. Thin and thick solid rectangular bars represent 90° and 180° nonselective pulses, respectively. Thin and thick solid rounded bars represent 90° and 180° selective pulses of 1–2 ms duration, respectively. Selective pulses are applied to the solvent magnetization and minimally perturb the solute magnetization. Open rectangular bars are the 3–9–19 pulse element $3\alpha_x$–τ–$9\alpha_x$–τ–$19\alpha_x$–τ–$19\alpha_{-x}$–τ–$9\alpha_{-x}$–τ–$3\alpha_{-x}$, in which $13\alpha = 90°$ and $\tau = 1/(2\Delta\nu_{\max})$. Delays ($\Delta$) are long enough to permit recovery following gradient pulses. Delays Δ_1 and Δ_2 are adjusted as described in Section 3.6.4.2 for the basic Hahn echo experiment and must be long enough to permit recovery following gradient pulses. Basic phase cycles can be elaborated using CYCLOPS and EXORCYCLE as described for the Hahn echo pulse sequence in Section 3.6.4.2.

magnetization into the transverse plane and rotates the water magnetization back to the longitudinal axis. Finally, a long spin lock purge pulse is applied phase shifted by 90° relative to the other pulses. Assuming that the selective and nonselective 90° pulses are applied with x-phase, the solute magnetization is described by an operator $-I_y$, and the solvent magnetization is described by an operator $-S_z$ prior to the purge pulse. If the purge pulse is applied with y-phase, then the solute operator commutes with the rotation operator for the pulse

and no evolution occurs (other than relaxation). Solute magnetization is said to be *spin locked* by the pulse. However, solvent magnetization is orthogonal to the spin lock pulse and is dephased by the inhomogeneity of the rf field as described in Section 3.4.6 (hence the name "spin lock" purge pulse). The original implementation of this technique used a rectangular soft pulse for the selective 90° pulse; subsequent elaborations of the principle have used shaped selective pulses and have extended the sequence as shown in Fig. 3.38b to improve the water suppression (*89*).

If the probe is capable of applying field gradient pulses, then additional control over and manipulation of the solvent signal are possible. Commonly utilized experimental techniques for solvent suppression fall into two categories. The first approach is similar in spirit to the spin lock purge pulse techniques in that a strong field gradient pulse is used to preferentially dephase the solvent signal (*90*). The second approach is similar in spirit to jump–return and binomial sequences in that the water magnetization is returned to the z-axis prior to acquisition (*88*).

An example of the former technique, which has been designated WATERGATE (*90*), is illustrated in Fig. 3.39a. Following the initial nonselective pulse, a strong gradient pulse dephases both solvent and solute magnetization. Solute magnetization is unaffected by the selective pulses (assuming the solute resonances of interest are outside the bandwidth of the selective pulses). The nonselective 180° pulse inverts the coherence order of the solute magnetization; therefore, the second gradient pulse rephases the solute magnetization to form a spin echo. In contrast, the combination of the selective 90° pulses and the nonselective 180° pulse leaves the coherence order of the solvent magnetization unchanged; therefore, the second gradient pulse continues to dephase the solvent magnetization and no echo is formed. The "soft–hard–soft" pulse sequence element can be replaced by a binomial 180° pulse; this has the advantage that the selective 90° pulse does not need to be calibrated. The sequence shown in Fig. 3.39b uses the "3–9–19" pulse for this purpose. The 3–9–19 pulse element is $3\alpha_x$–τ–$9\alpha_x$–τ–$19\alpha_x$–τ–$19\alpha_{-x}$–τ–$9\alpha_{-x}$–τ–$3\alpha_{-x}$, in which $13\alpha = 90°$ and $\tau = 1/(2\Delta\nu_{max})$. The excitation profiles for the two pulse sequence elements are shown in Fig. 3.40. The periodicity of the excitation profile of the binomial sequence often results in reduced amplitude of downfield $^1H^N$ or Trp $^1H^{\varepsilon 1}$ resonances in proteins. Superior water suppression is obtained using a double-gradient echo technique called "excitation sculpting" (*91*). A pulse sequence for this experiment is shown in Fig. 3.39c.

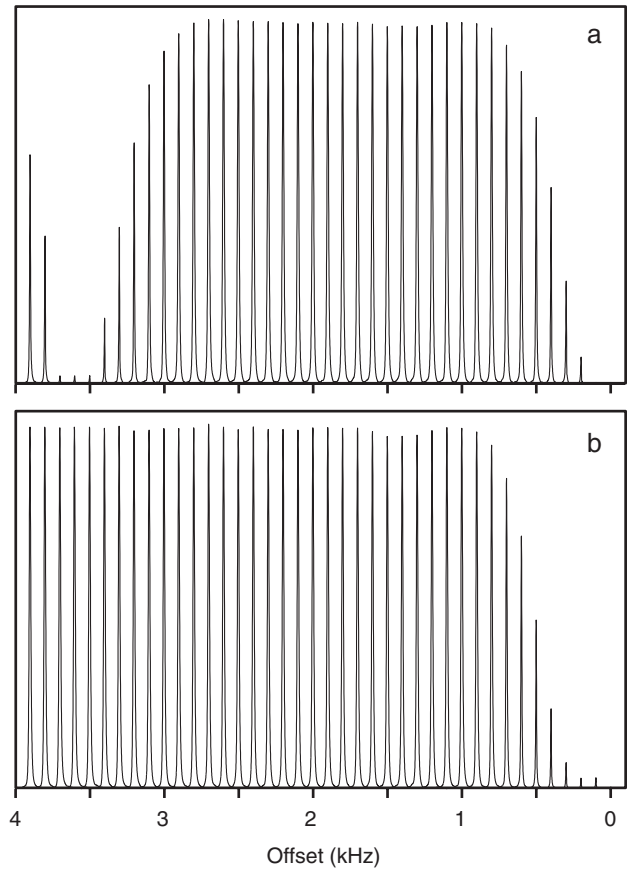

FIGURE 3.40 Water pulse excitation profiles shown for the (a) 3–9–19 pulse and (b) soft–hard–soft 90°_{-x}–180°_{x}–90°_{-x} pulse sandwich. The 3–9–19 pulse used a delay $\tau = 278$ μs and the soft 90° pulses had a length of 1 ms. Data were acquired on a 500 MHz NMR spectrometer.

An example of the second technique, which has been called "water flip-back" (*88*), is shown in Fig. 3.39d. The sequence is similar to the sequence of Fig. 3.39c except that a selective 90° pulse is inserted prior to the initial nonselective 90° pulse. Similar modifications are possible for the pulse sequences of Figs 3.39a and 3.39b. Following the nonselective 90° pulse, the solute magnetization is described by an operator $-I_y$, and the solvent magnetization is described by an operator S_z. The field gradients flanking the 180° pulses allow formation of a spin echo for solute magnetization (*92*). Any transverse solvent magnetization created

from nonideal performance of the selective 180° pulse and the nonselective 180° pulse is dephased by the field gradient pulses. The bulk of the water magnetization is aligned along the z-axis and is never saturated in this experiment. Radiation damping effects are minimized because any transverse solvent magnetization is dephased by the gradient pulses. In practice, 60–80% of the equilibrium water magnetization can be maintained along the z-axis and $>30\%$ increases in sensitivity are obtained for exchangeable solute ^{1}H spins due to reduced saturation transfer effects (*87, 88*).

A subtle difference between the WATERGATE and flip-back experiments concerns the strength of the gradient pulses. In the WATERGATE experiment, the bulk solvent signal must be dephased and strong (20–30 G/cm) gradients must be employed. In the flip-back experiments, only the fraction of the solvent signal that is not returned to the z-axis must be dephased and relatively weaker (5 G/cm) gradients are satisfactory. WATERGATE and flip-back experiments frequently need to rotate the water magnetization from the $+z$-axis to the transverse x–y plane (''flip-down'') or from the transverse plane to the $+z$-axis (''flip-up'') using relatively long selective pulses. At high static magnetic fields and especially with high Q probes, selective flip-down and flip-up pulses must be calibrated independently, because the effects of radiation damping oppose the former and reinforce the latter.

Examples of various water suppression techniques are given in Fig. 3.41. As described in Section 3.6.4.2, improved water suppression frequently is obtained if Hahn echo sequences are incorporated into the experimental pulse sequence. An example of the improved water suppression obtained is given in Fig. 3.54.

The purpose of the selective pulses in Figs. 3.38 and 3.39 is to independently manipulate magnetization components from solute and solvent ^{1}H spins. If the solute is isotopically enriched with ^{13}C or ^{15}N, then evolution under the heteronuclear scalar coupling Hamiltonian can be used to produce solute magnetization that is orthogonal or inverted relative to the solvent ^{1}H spins (and uncoupled solute ^{1}H spins). Spin lock purge pulses or field gradient pulses can be applied to preferentially dephase the solvent magnetization without recourse to selective pulses (*93*). Such techniques are commonly utilized in multidimensional heteronuclear NMR spectroscopy (Chapter 7).

3.7.4 POSTACQUISITION SIGNAL PROCESSING

Although numerous techniques have been proposed for postacquisition water suppression, the only technique in common usage at present

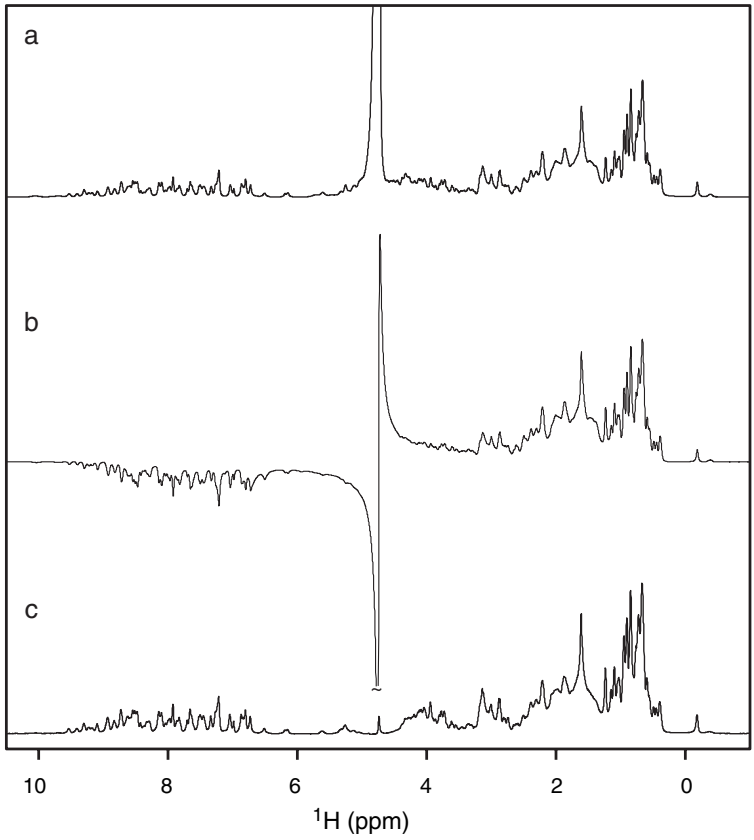

FIGURE 3.41 Water suppression using (a) presaturation, (b) jump–return, and (c) excitation sculpting techniques. Additional postacquisition water suppression can be obtained using a digital low-pass filter as illustrated in Fig. 3.42.

is the convolution difference low-pass filter technique (*94*). In this approach, the low-frequency components are filtered from the signal by constructing the data sequence

$$\tilde{s}(k\Delta t) = \sum_{j=-m}^{m} b_j s([k-j]\Delta t) \Big/ \sum_{j=-m}^{m} b_j \qquad [3.168]$$

in which b_j are filter coefficients. The cosine-bell filter function, $b_j = \cos[\pi j/(2m+2)]$, works well in practice. Typical values of m range between 8 and 32. The filtered data set is then obtained as $s(k\Delta t) - \tilde{s}(k\Delta t)$ If the experimental data consists of points $s(k\Delta t)$ for

$k = 0, \ldots, N-1$, the filtered data set consists of points $m, \ldots, N-m-1$. The missing m points at the end of the data sequence are generally unimportant because the original data set can be truncated; however, the first m points must be reconstructed to avoid large distortions in the resulting filtered spectrum. In the original approach, the first points were obtained by linear extrapolation (*94*); other approaches have included linear prediction of the first m points (*95*) or acquisition of data points for $k < 0$ using a Hahn echo pulse sequence (*96*). In most applications, the carrier is positioned at the frequency of the water signal. Consequently, the water resonance has an offset frequency of zero and the above protocol filters the water signal from the spectrum. If the carrier is positioned elsewhere in the spectrum, the water frequency is shifted digitally to zero by multiplication by a complex exponential function as shown by [3.20]. The convolution filter is applied to suppress the water signal and the original frequency reference is restored by multiplication by the complex conjugate of the original exponential function. The use of the digital low-pass filter for water suppression is illustrated in Fig. 3.42. As shown, the water signal is almost completely removed, although some distortion of the baseline is obtained near the location of the water signal. In all likelihood, improved digital filtration techniques will be developed (or adapted) for use in NMR spectroscopy.

3.8 One-Dimensional ^{1}H NMR Spectroscopy

Nearly all experimental investigations begin with one-dimensional NMR experiments to assess the suitability of the sample for more detailed characterization by multidimensional NMR spectroscopy. In addition, the procedures used to acquire a one-dimensional experiment, including temperature calibration, tuning, shimming, and measurement of pulse lengths, are equally necessary for multidimensional experiments.

3.8.1 SAMPLE PREPARATION

Sophisticated NMR experiments only rarely can compensate for an ill-behaved or ill-prepared NMR sample. Accordingly, in nearly all investigations, preliminary experiments must be performed to determine sample conditions that satisfy the following criteria:

1. The protein must be in a native, functional conformation (unless unfolded or intermediate states of the protein are the focus of investigation). Ideally, the pH and solvent composition should be

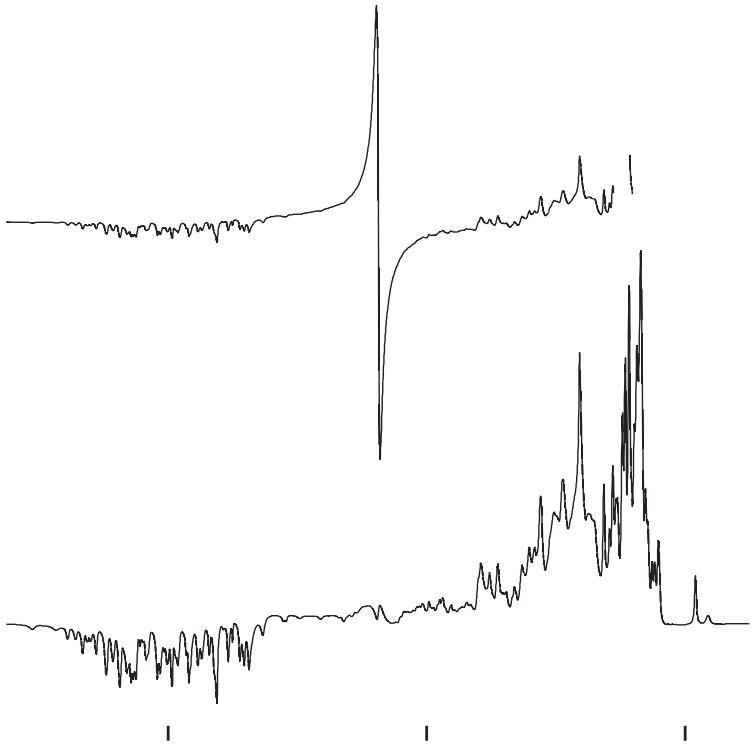

close to physiological conditions so that the structural and dynamic observations reflect a functionally relevant state of the protein.

2. Solubility must be sufficient to permit spectra with satisfactory signal-to-noise ratios to be acquired in reasonable time periods. For conventional probes and sample tubes, 0.4–0.6 ml of a protein solution of approximately 1 m*M* concentration (in a 5-mm NMR tube) will be required for studies at 500 MHz. Sample volumes can be reduced to approximately 0.2 ml in low-volume NMR tubes.

If cryogenically cooled probes are available, sample concentrations can be reduced, depending on the ionic strength of the sample buffer.

3. Protein samples used for NMR spectroscopy must be free of contaminants arising from the NMR tube or the protein preparation. The protein should be monodispersed (unaggregated) at the concentrations required for NMR spectroscopy and stable for time periods longer that the desired NMR experiments.
4. Ideally, NMR spectroscopy should be performed under sample conditions that yield optimal spectra (maximal resonance dispersion and minimal linewidths).

Temperature, pH, concentration, and buffer composition affect dramatically the solubility, aggregation state, and stability of proteins, and must be optimized empirically. Sample preparation for NMR spectroscopy has been the subject of extensive review articles (*97, 98*).

3.8.2 INSTRUMENT SETUP

Temperature calibration, tuning, shimming, and pulse length calibration are preludes to data acquisition for all one-dimensional and multidimensional NMR experiments. Furthermore, information about longitudinal and transverse relaxation rate constants is useful for setting recycle delay times and anticipating the overall sensitivity of particular NMR experiments.

3.8.2.1 Temperature Calibration Most commercial spectrometers have some means of controlling the probe temperature, and this hardware provides a coarse estimate of the actual sample temperature. More accurate schemes have been developed that make use of the temperature-dependent chemical shifts of methanol and ethylene glycol to calibrate the actual temperature of a sample in the probe (*99*). Over the range 250–320 K, the difference in chemical shift between the methyl and hydroxyl resonances of 100% methanol, $\Delta\delta$ (in ppm), is given by

$$T(\mathrm{K}) = 403.0 - 29.53\Delta\delta - 23.87(\Delta\delta)^2. \qquad [3.169]$$

Over the range 300–370 K, the difference in chemical shift between the methylene and hydroxyl resonances of 100% ethylene glycol, $\Delta\delta$ (in ppm), is given by

$$T(\mathrm{K}) = 466.0 - 101.6\Delta\delta. \qquad [3.170]$$

The chemical shift of the ^{1}H spins in H_2O has a slight dependence on pH (0.02 ppm/pH unit), and a more dramatic dependence on temperature. The chemical shift of the water resonance is given by (*100, 101*)

$$\delta(H_2O) = 7.83 - T/96.9\,\text{ppm}, \qquad [3.171]$$

in which the temperature is measured in Kelvin and pH = 5.5.

3.8.2.2 Tuning In order to efficiently deliver rf energy into the sample volume and to sensitively detect precessing transverse magnetization, the probe circuitry must be *tuned* so that the *resonant frequency* of the circuit is equal to the rf frequency. In addition, the *impedance* of the coil must be *matched* to the impedance of the spectrometer electronics ([3.2]). The probe circuitry is tuned and matched by adjusting two capacitors mounted near the coil. The principle is simple: the coil is driven by an rf input and the response is observed as the fraction of reflected power (i.e., the rf power not transmitted into the sample volume). The capacitors are adjusted interactively to optimize the response. Two methods are commonly used to tune and match the probe; the two methods differ in the way in which the rf is applied and the response is detected. Increasingly, the capability to tune and match the probe is built into NMR spectrometers.

In the first method, illustrated in Fig. 3.43a, a sweep generator, a 50-Ω load, an oscilloscope, and the probe are connected to the terminals of an rf bridge. The sweep generator generates an rf field with a frequency that is cyclically varied in time. As the rf frequency "sweeps" through the resonance frequency of the coil circuit, the sides of the rf bridge become more balanced, and a dip (or peak, depending on the input polarity) is observed on the scope. The horizontal position of the dip indicates the resonance frequency of the coil (typically, an rf reference source is also displayed on the oscilloscope in order to calibrate the display); the depth of the dip is a measure of the match between the impedance of the circuit and the 50-Ω load. The tuning and matching capacitors are adjusted until the resonance frequency of the coil equals the desired value and the impedance is optimally matched (as indicated by a maximum in the depth of the dip).

In the second method, illustrated in Fig. 3.43b, a fixed-frequency rf source and a voltage standing-wave ratio (VSWR) rf power meter are connected to the probe through a directional coupler. The signal measured on the power meter is proportional to the power reflected from the probe; as the tuning and matching of the probe improve, the amount of reflected power decreases, because more power is being transmitted

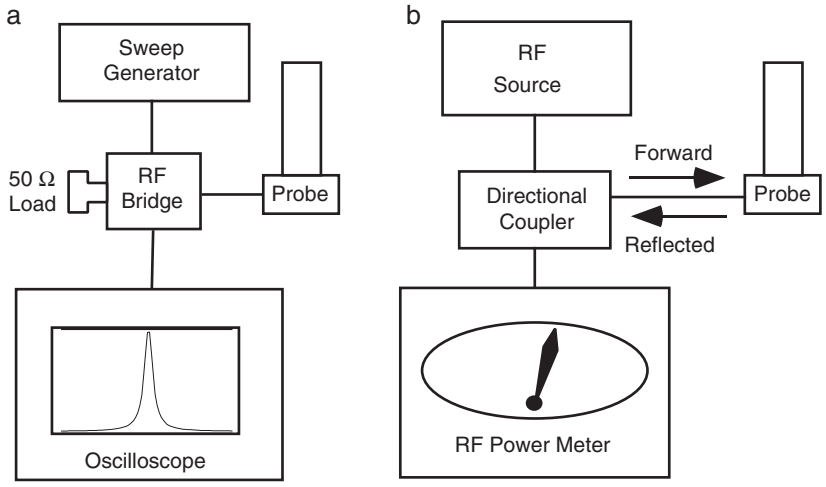

FIGURE 3.43 Tuning circuits employing the (a) sweep generator and (b) monochromatic rf source. Details on the use of these circuits are given in the text.

into the sample volume. Accordingly, the tuning and matching capacitors are adjusted to minimize the reflected power.

If the probe is very poorly tuned, or if one is searching for a new nuclear resonance signal on a broadband probe, the sweep generator configuration is superior because tuning and matching responses are monitored independently. Once the probe is nearly tuned and matched, the second approach typically is more sensitive.

Minimum pulse lengths for a given amplifier power level are obtained only if the probe is properly tuned and matched. A historical record of pulse lengths previously measured for the same sample and probe should be maintained (pulse lengths for different samples are a function of differences in ionic strength). A measured pulse length that deviates by more than a few percent from previous values indicates that either the probe has been improperly tuned or that a problem has developed with the transmitter circuitry.

3.8.2.3 Shimming The homogeneity of the static magnetic field is of paramount importance for high-resolution NMR spectroscopy. The natural magnetic field of a superconducting magnet is not sufficiently homogeneous for high-resolution spectroscopy. Accordingly, a necessary task prior to performance of an NMR experiment is the careful

adjustment of the magnetic fields produced by a set of auxiliary room-temperature electromagnets to compensate the inhomogeneity of the main static field. This process is known as shimming. Two articles devoted to the process of shimming form the basis for the present discussion (*102, 103*).

The spatial variation of the static magnetic field within the bore of the magnet satisfies the Laplace equation and can be described by an expansion in orthogonal spherical harmonic functions, $r^n P_{nm}(\cos\theta)\cos[m(\varphi - \varphi_{nm})]$:

$$B_0(r,\theta,\varphi) = \sum_{n=0}^{\infty}\sum_{m=0}^{n} c_{nm}\left(\frac{r}{a}\right)^n P_{nm}(\cos\theta)\ \cos[m(\varphi - \varphi_{nm})], \qquad [3.172]$$

in which a is the radius of the magnet bore, c_{nm} and φ_{nm} are constants, and $P_{nm}(\cos\theta)$ are the associated Legendre polynomials. The values of n and m for which c_{nm} are nonzero and the particular values of c_{nm} and φ_{nm} are determined (depending on one's point of view) by the empirical variation in the magnetic field or by the solution to the Laplace equation subject to the (complicated) appropriate boundary conditions inside the magnet bore. If the field were perfectly homogeneous, the only nonzero c_{nm} in [3.172] would be c_{00}, the amplitude of the static field.

In principle, the inhomogeneity in the static magnetic field can be compensated identically by generation of additional magnetic fields with spatial variation described by the spherical harmonic functions and amplitude given by $-c_{nm}$. Each additional magnetic field would negate one of the terms in [3.172] and the number of auxiliary fields needed would be determined by the desired degree of compensation. In practice, the auxiliary fields are produced by specially designed electromagnets and the magnitudes of the fields are proportional to the applied electric currents. The shim coils are conventionally described using Cartesian rather than spherical coordinates; the spherical harmonic functions corresponding to shim coils frequently encountered on NMR spectrometers are given in Table 3.1. The functions of degree $m > 0$ appear in pairs with x and y interchanged in order to reproduce the phase dependence, φ_{nm}, in [3.172].

In reality, shim magnets cannot be designed or fabricated to produce a pure spherical harmonic magnetic field; consequently, the field produced by the shim coils is described by

$$B'(r,\theta,\varphi) = \sum_{k=1}^{N} b_k B_k(r,\theta,\varphi), \qquad [3.173]$$

TABLE 3.1
Shim Coil Spherical Harmonic Functions

Order (n)	Degree (m)	Shim name	Functions
1	0	z	z
2	0	z^2	$2z^2-(x^2+y^2)$
3	0	z^3	$z[2z^2-3(x^2+y^2)]$
4	0	z^4	$8z[z^2-3(x^2+y^2)]+3(x^2+y^2)^2$
5	0	z^5	$48z^3[z^2-5(x^2+y^2)]+90z(x^2+y^2)^2$
1	1	x	x
1	1′	y	y
2	1	zx	zx
2	1′	zy	zy
3	1	z^2x	$x[4z^2-(x^2+y^2)]$
3	1′	z^2y	$y[4z^2-(x^2+y^2)]$
2	2	x^2-y^2	x^2-y^2
2	2′	xy	xy
3	2	$z(x^2-y^2)$	$z(x^2-y^2)$
3	2′	zxy	zxy
3	3	x^3	$x(x^2-3y^2)$
3	3′	y^3	$y(3x^2-y^2)$

in which N is the number of shim coils, $B_k(r,\theta,\varphi)$ is the spatial field produced by the kth shim coil, and b_k is the amplitude of the field determined by the electric current applied to the electromagnet. Each $B_k(r,\theta,\varphi)$ is given by an expansion similar to [3.172]; as a result, the terms in [3.173] are not orthogonal and no one-to-one correspondence exists between the terms in [3.173] and the terms in [3.172]. In order to overcome this difficulty, some types of shim systems rely on a matrix design, in which the desired ideal field profiles are generated by supplying current to more than one physical coil. The potential advantage of a matrix shim system is that the difficulties of manufacturing a set of shim coils that generate spatial field profiles with the desired, pure spherical harmonic functional forms can be overcome; this is done by allowing the ideal shim profiles to be approximated more accurately by an appropriately weighted superposition of a subset of the field profiles generated by the actual physical shim coils. The necessary values of the matrix elements that determine the distribution of current in the physical coils are established and set by the manufacturer. Thus, current adjustments are applied to multiple physical coils when adjusting the value of an idealized shim in a matrix

shim system. From a practical point of view, the main reason one may need to know whether a matrix design is in use is for hardware debugging purposes: in a matrix shim system, a bad current supply or broken coil can affect more than one of the apparent shim components $B_k(r, \theta, \varphi)$.

Empirical adjustment of the shim coils is performed using the magnitude of the field frequency lock signal, the decay envelope of the FID, and the lineshape in the frequency domain spectrum as measures of the homogeneity of the magnetic field. The lock signal is the simplest parameter to observe; because the integral of the resonance signal is constant, the lock signal increases in magnitude as the field homogeneity improves and the deuterium lineshape becomes narrower. However, the magnitude of the lock signal does not indicate the quality of the lineshape obtained. In addition, the lock system must be properly calibrated if proper shimming is to be obtained. The phase of the lock receiver must be adjusted to yield a purely dispersive signal. Drifts in the magnetic field are detected most sensitively if the lock signal is dispersive, because the dispersive lineshape has a null at the exact resonance frequency [3.30]. The power level must be adjusted to yield a signal with adequate signal-to-noise ratio without saturating the deuterium resonance. If the FID can be displayed in real time, the magnetic field can be shimmed by observing the shape of the decay envelope. Optimal homogeneity implies that the decay envelope is exponential with a maximal decay time constant. Unlike the lock signal, the FID is a direct indication of the quality of the lineshape. Shimming using the FID is easiest if the decay is dominated by a single resonance line; thus, for samples in water, the magnet can be shimmed using the water resonance. In this case, the probe should be detuned while shimming, to avoid radiation damping that distorts the shape of the FID (Section 3.5). After the magnet is shimmed, the probe is retuned (after tuning, the shims may need additional minor adjustments).

The ultimate measures of the homogeneity of the magnetic field are the lineshape and resolution in the spectrum and quality of the solvent suppression. When beginning a research project on a new biomolecule, a pair of closely spaced resonances, preferably representing a scalar coupled multiplet, should be identified; the pair can be used subsequently to monitor shimming. That is, if a particular multiplet is resolvable when the magnet is properly shimmed, then the quality of the shimming can quickly be checked by examining the degree of resolution of the multiplet lineshape.

External samples also can be used to check the homogeneity of the magnetic field. Samples of basic pancreatic trypsin inhibitor (BPTI),

ubiquitin, or tryptophan are useful in this regard. Unlike resolution test samples used by instrument manufacturers, these molecules can be dissolved in aqueous solutions with buffers and ionic strength matched to the conditions of the sample of interest. For BPTI, resolution can be evaluated by examining the tyrosine 23 $^1H^{\varepsilon}$ multiplet at 6.3 ppm. For ubiquitin, resolution can be evaluated by examining the leucine 50 $^1H^{\delta}$ multiplet at -0.17 ppm or the phenylalanine 45 $^1H^{\delta}$ multiplet at 7.33 ppm. For tryptophan, resolution can be evaluated by examining the $^1H^{\eta 2}$ triplet at 7.24 ppm. In a high-resolution spectrum, the ^4J coupling to $^1H^{\varepsilon 3}$ should be resolvable almost to baseline and the small ($\sim$0.5 Hz) ^6J coupling to $^1H^{\delta 1}$ should be discernible.

The exact manual or semiautomatic protocol that is optimal for empirical shimming (by the operator) of a particular magnet by hand depends upon the complement of shim coils provided by the spectrometer manufacturer. Accordingly, the protocol given in Fig. 3.44 should be taken as a guideline appropriate for the shim set given in Table 3.1. The problem of empirical shimming is simplified somewhat because a given shim field is contaminated primarily by shim fields of lower orders with the same parity (i.e., z^3 contains contributions primarily from z, and z^4 contains contributions primarily from z^2). In addition, the resonance lineshape obtained is frequently indicative of the order of the shim coil that must be adjusted. Misadjustment of the even-order shims result in asymmetric lineshapes; misadjustment of the odd-order shims result in symmetrical, but non-Lorentzian, lineshapes. Furthermore, the effect on the lineshape is observed closer to the baseline for higher order shims. The problem of shimming reduces to implementation of a reasonable strategy for optimizing the coefficients b_k in [3.173] to approximate to [3.172]. Unfortunately, trial-and-error manual adjustments or interative automated routines, in addition to being time-consuming, are prone to finding local optima in the shim values rather than global optima that maximize magnet homogeneity.

The traditional methods for magnet shimming just described are being supplanted by gradient-based techniques that were initially developed for shimming magnets used for magnetic resonance imaging (*104, 105*). These so-called gradient shimming techniques are based on the simple principle of mapping both the magnetic field homogeneity and the magnetic field profiles generated by the various room-temperature shim coils, and then calculating the optimal values for each shim current needed to minimize the residual field inhomogeneity. If the spatial dependence of the magnetic field inhomogeneity, expressed for simplicity using Cartesian coordinates, is given by $\Delta B(x, y, z) = B(x, y, z) - B_0$ [where $B(x, y, z)$ is the actual uncorrected

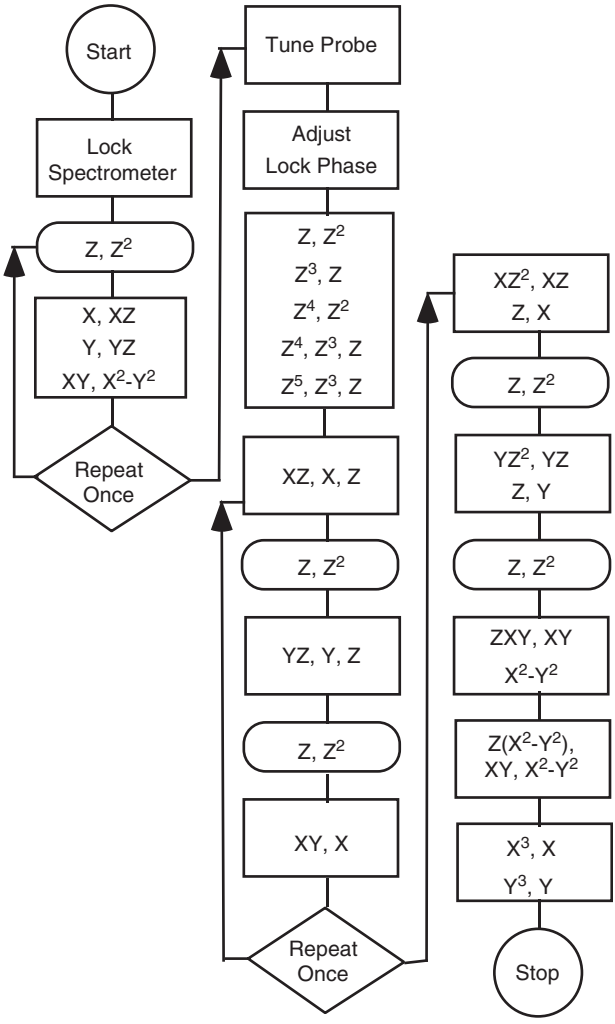

FIGURE 3.44 Shimming protocol.

magnetic field and B_0 is the desired homogeneous field value], and the spatial profile of the magnetic field generated by a given shim coil is given by $S_i(x, y, z)$, then the basic goal of any shimming process is to minimize the residual function $B_{\text{resid}}(x, y, z)$,

$$B_{\text{resid}}(x, y, z) = \Delta B(x, y, z) - \sum_i c_i S_i(x, y, z), \qquad [3.174]$$

by adjusting the values of the coefficients c_i. The summation is over the number of shim components contained in the shim system. The innovation supplied by the gradient shimming-based techniques is to actually map the functions $\Delta B(x, y, z)$ and $S_i(x, y, z)$, such that a straightforward and deterministic mathematical procedure (*106*) can be used to minimize B_{resid}. Gradient shimming methods are noniterative (or rapidly convergent), are insensitive to local minima in [3.174], and provide a robust, convenient, and time-saving method for optimizing magnet homogeneity.

The initial application of gradient shimming in NMR spectroscopy utilized three-axis pulsed field gradient hardware to generate three-dimensional maps of the magnetic field and shim coil field profiles (*106*). In principle, the shim system itself could be used for the imaging experiments required for gradient shimming. However, the original method required that field gradients be switched on and off rapidly (typically less than 1 ms), and that no significant distortions were generated by gradient-induced eddy currents. The shim power supplies are normally designed for high stability in continuous operation, rather than in a pulsed mode, and the shim coils are not shielded, so that problems with eddy currents in pulsed operation would be significant. In addition, typically the shim currents cannot be rapidly switched under pulse sequence control. Some time ago, modified procedures were reported that allowed gradient shimming to be performed with the normal spectrometer shim system (*107*), and the spectrometer manufacturers have continued to develop and implement such techniques. The present discussion of gradient shimming will focus on the use of pulsed field gradient hardware, although most of the general principles remain the same if the shim system itself is employed. Furthermore, for the sake of clarity, the following discussion will be restricted to one-dimensional gradient shimming of the z-shims (*108, 109*). The z-shims are typically the ones most in need of routine adjustment from sample to sample, and thus the use of z-axis gradient shimming is currently the most common application of imaging-based shimming techniques.

The basic task in gradient shimming is to measure, or map, the magnetic field variation within the sample volume of interest. This mapping is accomplished using the principles of magnetic resonance imaging. In the case of z-axis gradient shimming, the sample volume can be imagined to consist of thin disks stacked vertically on top of one another, with the z-axis running through the center of the disks, perpendicular to the plane of the disks. The z-axis is also defined to be collinear with the direction of the external magnetic field. Mapping of

the field along the z-axis therefore consists of measuring the average value of the magnetic field within each disk. This is accomplished by measuring an NMR signal for the sample contained within each imaginary disk. The sample should have one component that gives rise to a single resonance and completely dominates the NMR spectrum; for aqueous protein samples in H_2O, the ^{1}H resonance of the solvent water provides the requisite signal. If an FID is recorded while a substantial, linearly dependent (with respect to the z-coordinate) magnetic field gradient is applied along the z-axis, the exact resonance frequency of the water ^{1}H nuclei contained within each disk will depend on the position of the disk along the z-axis:

$$\begin{aligned}\omega(z) &= -\gamma B_0 - \gamma G z \\ &= \omega_0 - \gamma G z,\end{aligned} \qquad [3.175]$$

in which B_0 is the strength of the external magnetic field, γ is the magnetogyric ratio for the nucleus being observed, and G is the strength of the applied magnetic field gradient. Equation [3.175] assumes that the applied magnetic field gradient is large enough to completely dominate the inhomogeneity in the external field, so that the actual field profile $B(x, y, z)$ can be approximated by the single value B_0. Without loss of generality, the center of the rf coil is assumed to define the origin of the z-axis. Due to the magnetic field gradient, the water resonance will appear as a broad distribution of frequencies in the NMR spectrum. A typical spectrum is shown in Fig. 3.45. For the case of a sample that extends well beyond the confines of the rf detection/transmitter coil, the lineshape of the NMR signal shown in Fig. 3.45 is essentially an "image," or mapping, of the rf field distribution of the coil: the signal dies away at the edges of the spectrum, due to the drop-off in the rf field strength and the detection sensitivity at the extremes of the effective volume of the coil. If the volume of the sample is restricted and does not completely fill the active volume of the rf coil, then the NMR lineshape would in principle be an image of the physical location of the sample. While the horizontal axis in Fig. 3.45 is in frequency units, this can be directly converted to distance units along the z-axis, via [3.175], and assuming that the rf transmitter frequency coincides with the Larmor frequency of the water resonance in the absence of the field gradient. Thus, application of the magnetic field gradient allows spatial resolution of the water signal along the z-axis.

In practice, the lineshape profile depends on the linearity of the applied z-axis magnetic field gradient as well as the rf field distribution within the coil volume. Assuming that the rf field distribution is

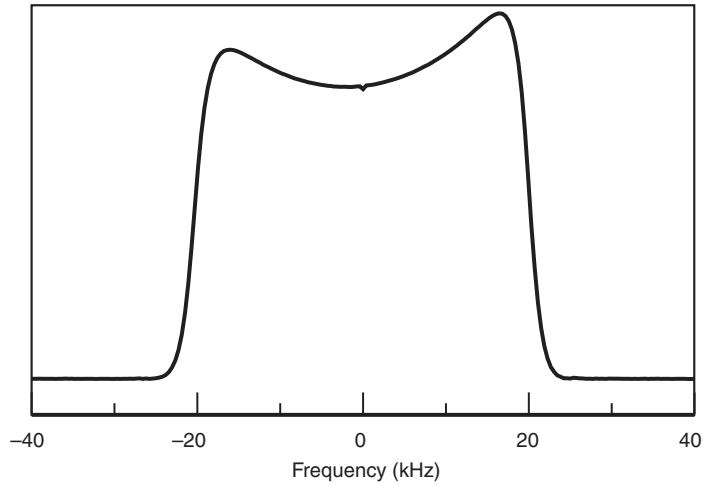

FIGURE 3.45 The ^{1}H NMR spectrum of an H_2O sample, recorded at 600 MHz using the pulse sequence shown in Fig. 3.46a, with $\tau = 0$. The spectrum is plotted in magnitude mode. The spectrum corresponds approximately to a 1D image projection of the effective transmitter/receiver coil volume along the z-axis, which is defined as the direction of the static external magnetic field B_0. The sample was contained in a standard 5-mm-diameter NMR tube; the left-hand side of the spectrum corresponds to the lower half of the effective sample volume (i.e., toward the bottom of the NMR tube). The absence of a flat plateau across the spectrum results from nonlinearity of the z-axis pulsed field gradient.

reasonably homogeneous, nonlinearity of the z-axis magnetic field gradient can result in distortions of the expected flat top profile and give a misleading impression of an unequal distribution of sample within the rf coil. The data shown in Fig. 3.45 were taken on a 9-year-old probe; current probes might exhibit a much flatter profile. In any case, linearity of the field gradient is not required for gradient shimming to work; the necessary condition is that the applied magnetic field increases monotonically as a function of the position along the z-axis.

Having achieved spatial resolution via the application of the z-axis magnetic field gradient during acquisition of the NMR signal, the next step is to measure the actual spatial dependence of the static magnetic field within the active rf coil volume. This is accomplished via the measurement of a so-called phase map. Assume an rf pulse is applied to the sample to create transverse magnetization, and that a period of free precession is allowed to occur. The precession frequency, for a given

nucleus, will be directly proportional to the value of the local magnetic field strength. If the length of the precession period is given by τ, then the phase accumulated by the spin isochromats is given by

$$\begin{aligned}\phi(z) &= \omega(z)\tau + \phi_0 \\ &= -\gamma[B_0 + \Delta B(z)]\tau + \phi_0,\end{aligned} \qquad [3.176]$$

in which the axial field variation, $\Delta B(z)$, resulting from inhomogeneity of the static external magnetic field over the active sample volume, is included explicitly. In this case, $\Delta B(z)$ is the average field inhomogeneity over the x–y plane located at the given position along the z-axis and is the term to be measured and ultimately minimized via shimming adjustments. The constant term φ_0 accounts for the net contribution from precession during periods other than τ. If the experiment is repeated twice, using different values of the free precession period τ_1 and τ_2, then the axial field variation can be determined from [3.176] to be

$$-\Delta B(z) = B_0 + \frac{[\varphi_2(z) - \varphi_1(z)]}{\gamma(\tau_2 - \tau_1)} = B_0 + \frac{\Delta\phi}{\gamma\Delta\tau}, \qquad [3.177]$$

in which $\Delta\phi(z) = \phi_2(z) - \phi_1(z)$ and $\Delta\tau = \tau_2 - \tau_1$. Typically, $\tau_2 > \tau_1 \approx 0$. Thus, by mapping the z-dependence of the phase of the NMR signal, the desired map of the magnetic field inhomogeneity can be determined.

Suitable pulse sequences commonly employed to perform the basic experiment just described are shown in Fig. 3.46. Both sequences in Fig. 3.46 result in the formation of an echo signal during the detection period, the purpose of which will be explained in the following discussion. The first sequence, Fig. 3.46a, is based on the use of a spin echo. Immediately after the initial 90° excitation pulse, a z-axis pulsed field gradient is applied, which is then followed by the variable precession period τ. A 180° refocusing pulse is then applied, which will lead to the formation of a spin echo. At this point in the sequence the "read" gradient is turned on, and the FID is recorded during this period. The timings are arranged such that the maximum of the echo formation occurs in the middle of the data acquisition period, and that the signal is not truncated at the beginning or end of this period. The pulse sequence in Fig. 3.46b is essentially the same as that in Fig. 3.46a except that a gradient-recalled echo is employed instead of a spin echo; the gradient-recalled echo is achieved by inverting the sign of the initial pulsed field gradient, relative to the "read" gradient. Although either sequence can be used to achieve the desired result, the spin echo experiment has at least one practical advantage. The magnetic field inhomogeneity causes dephasing of the NMR signal during the full

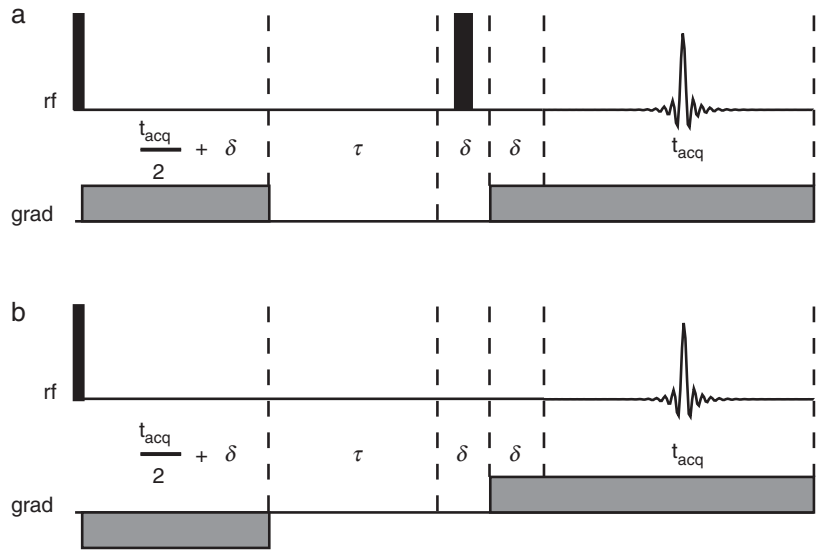

FIGURE 3.46 Pulse sequences for z-axis gradient shimming. Narrow and wide pulses on the rf channel represent 90° and 180° flip angles, respectively. Gradient pulses, represented by the gray boxes, are applied along the z-axis; the first gradient pulse in sequence b is applied with the sign opposite to that used for the second (''read'') gradient. The total acquisition time, t_{acq}, should be set such that the entire, observable echo signal is recorded. The delay Δ (1 ms) allows for dissipation of transient effects when the gradient pulses are turned on and off. FIDs are recorded for two different values of the delay τ to allow the desired measurement of the signal phase evolution.

period of the gradient-recalled echo experiment, whereas the effects of the field inhomogeneity are minimized in the spin echo experiment due to the refocusing effect of the 180° pulse. A common variation of these pulse sequences is to reverse the order of the initial gradient pulse and the variable precession period, in order to eliminate potential problems with gradient ring-down effects during the variable precession period. However, the sequences as drawn in Fig. 3.46 have the advantage that radiation damping of the water magnetization is suppressed by the application of the gradient pulse immediately following the initial excitation rf pulse.

The pulse sequences shown in Fig. 3.46 record the entire echo signal, from the initial buildup, through the echo maximum, and past where the echo has decayed away. If the time origin $t = 0$ is placed at the position

of the echo maximum, then the NMR signal is effectively recorded for the entire period $-\infty < t < +\infty$ (remembering that data collection is arranged such that the signal decays into the noise at the beginning and end of the detection period). Thus, the time-domain signal is no longer causal, and Fourier transformation results in an NMR spectrum that has no dispersive component (*110*). The absence of a dispersive component has two important consequences for application to gradient shimming. First, the phase of the NMR signal as a function of the position along the z-axis, which provides the phase maps $\varphi_i(z)$ needed in [3.177], can be determined by taking the arctangent of the ratio of the real and imaginary components of the NMR spectrum. Second, a magnitude calculation (given by the square root of the sum of the squares of the real and imaginary components) applied to the frequency-domain NMR spectrum will result in a true image of the active coil volume or spin density, as shown in Fig. 3.45. In addition, collection of the full echo signal may result in increased sensitivity, by up to a factor of two depending on the signal loss incurred by delaying acquisition of the FID to allow an echo to form (*110*). A typical spectrum collected with the pulse sequence in Fig. 3.46b is shown in Fig. 3.45.

Several parameters must be optimized in performing the experiments shown in Fig. 3.46. A practical issue concerns the length of the variable delay τ_2. If the sequences as drawn in Fig. 3.46 are employed, only a small decay of the signal intensity occurs between the two spectra acquired for τ_1 and τ_2. If the variable precession period is inserted before the first gradient pulse (or the gradient-recalled echo sequence, Fig. 3.46b) is employed, a substantial reduction in intensity will be observed for the spectrum recorded with the longer τ_2 value relative to that for τ_1, due to signal decay from the combined effects of spin relaxation, radiation damping, translational diffusion, convection, and magnetic field inhomogeneity. On the one hand, a precession period $\Delta\tau$ should be chosen in order to maximize the phase difference $\Delta\phi(z)$ and therefore optimize the accuracy of the measurement of the field inhomogeneity. On the other hand, decay of signal intensity reduces the precision of the phase information that is extracted from the spectra. Maximizing the signal-to-noise ratio of the spectra is important for obtaining the best results. If a spin echo is used (Fig. 3.46a) and/or radiation damping is suppressed, very large values of $\Delta\tau$ can be chosen; otherwise, a reasonable rule-of-thumb in balancing the desire to maximize $\Delta\tau$ without giving up too much in spectral sensitivity is to choose τ_2 such that the spectrum collected at τ_2 is approximately half the intensity of the spectrum collected at the short time point $\tau_1 \approx 0$. In addition, the phase values are determined from taking the inverse

of sinusoidal functions, and are therefore restricted to the range 0°–360°. At some point, as the precession period $\Delta\tau$ is increased, a so-called phase-wrap will occur, where the actual value of $\Delta\phi$ falls outside the 0°–360° range and is aliased or wrapped back into that range; such an occurrence would obviously lead to an incorrect determination of the residual magnetic field ΔB. The simplest solution to this problem is to restrict the duration $\Delta\tau$; however, this restriction compromises the accuracy of the measurement. Instead, algorithms can be devised for unwrapping the phases, thereby freeing up the user to optimize $\Delta\tau$ according to the above criteria.

Along the same line of reasoning, the strength of the pulsed magnetic field gradients used in the pulse sequences (Fig. 3.46) must be large enough to provide adequate spatial resolution of the field map and to dominate the initial static field inhomogeneity, but not so large as to lead to an unacceptable loss in spectra sensitivity, which would result from spreading the spectrum over too wide a frequency range. Finally, the width of the spectral window used for the field mapping must be chosen. The wider the window, the larger the sample volume that can be mapped. On the other hand, the window should not be extended to the point where the signal has decayed essentially to zero, as the resultant errors in the phase map will be propagated into errors in establishing optimal values for the shim currents.

The preceding discussion has focused on mapping the magnetic field inhomogeneity, $\Delta B(z)$, within the active sample volume. However, according to [3.175], the field profile generated by each of the shim coils considered in the gradient shimming process, $S_i(z)$, must be determined (remembering that we are limiting our discussion here to z-axis shimming). Because the actual spatial dependence of the shim fields are mapped, the profiles are not required to have ideal shapes (i.e., deviations of the $Z2$ shim profile from the ideal z^2 dependence are easily tolerated). Mapping the field profiles generated by the shim coils is done in exactly the same fashion as discussed previously for the magnetic field inhomogeneity. Spectra similar to those of Fig. 3.45 are collected, using a pulse sequence such as one of those shown in Fig. 3.46, for two different shim settings for each of the shim coils being considered. Using the resulting phase maps and [3.177], the shim profiles are established. Typical results are shown in Fig. 3.47 for the Z1–Z6 shim coils of a modern NMR spectrometer. The horizontal axis is labeled in frequency units, but this is equivalent to a z-axis scale, via [3.175]. The ideal shapes can be recognized for most of the shim profiles, i.e., the Z1 shim gives a linear dependence, Z2 a parabolic dependence, Z3 a z^3 dependence, and so on; the results shown in Fig. 3.47 also indicate that impurities exist

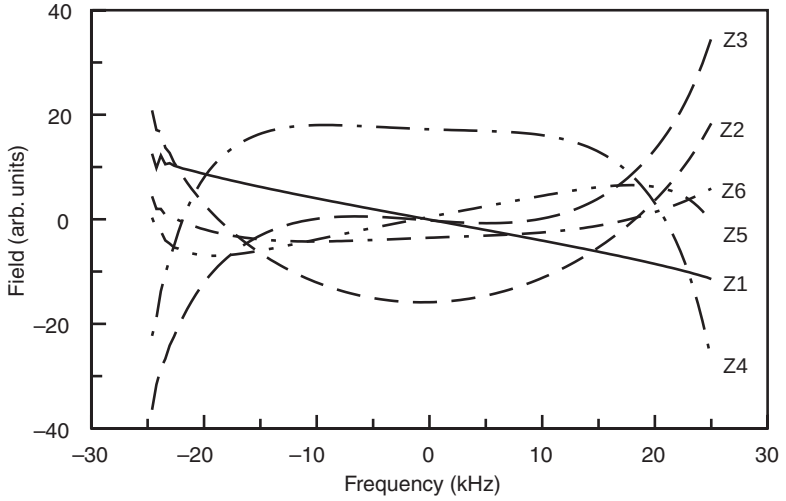

FIGURE 3.47 Typical z-axis shim maps determined using the pulse sequence of Fig. 3.46a, with τ values of 0 and 15 ms. Shim maps are shown for the Z1–Z6 shim coils.

in the various profiles. Practical experience has been that the Z6 shim usually deviates significantly from the ideal result. Once the shim profiles have been determined, calculating the set of weighting coefficients c_i in [3.174] (in other words, the "shim values") that leads to a minimization of the residual magnetic field inhomogeneity is a straightforward mathematical exercise (*106*).

In principle, mapping the field profiles of the shim coils needs to be done only when some major change has occurred, such as switching probes; in practice, very little time is required to map the z-axis shims and the procedure therefore can be performed whenever a sample is changed. An important point to note is that the shimming procedure relies on the shim maps covering the same region as covered by the maps of the field inhomogeneity, which means that the same offset frequency must be used (*111*). As already outlined, only a single mapping of the magnetic field inhomogeneity is needed in principle. However, due to inherent, practical limitations, the procedure usually is iterated until some acceptable level of field correction is achieved. The entire process typically is highly automated by the spectrometer software, and normally only a few iterations are needed to achieve optimal results.

Several variations or extensions of the *z*-axis gradient shimming procedure as already outlined have been implemented. Although the current discussion has focused on *z*-axis gradient shimming, full three-dimensional (3D) mapping can be performed (*106*), which allows all shims to be optimized, instead of just the *z*-axis shims. Full 3D gradient shimming is particularly useful when shimming a new probe, or when trying to obtain optimum lineshape in highly demanding situations such as water suppression. As mentioned already, modified procedures have been devised that allow the use of the room-temperature shims to perform the imaging experiments; this capability is particularly useful because many probes, notably all current-generation cryogenic probes, only have *z*-axis pulse field gradient capability. Gradient shimming also can be performed by observing the deuterium resonance for samples dissolved in a deuterated solvent (*111*); the current generation of commercial NMR spectrometers typically can perform deuterium gradient shimming under software control, without the need to reconfigure the cabling to the deuterium channel of the probe (the rf channel used for deuterium gradient shimming and the separate lock channel both feed into a single port of the NMR probe). When using a deuterium signal for gradient shimming, the phase evolution period $\Delta\tau$ must be lengthened because the ^{2}H nucleus has a smaller magnetogyric ratio than does the ^{1}H nucleus. Finally, a modification of the basic pulse sequences shown in Fig. 3.46 has been reported to be highly effective in minimizing the deleterious effects of sample convection on the gradient shimming process (*112*). As in any gradient-based experiment, sample convention severely attenuates NMR signals, due to incomplete refocusing of magnetization as individual molecules move from one location in the sample to another. Sample convection results from the presence of temperature gradients along the sample, and thus is most likely to occur for sample temperatures far from ambient.

Other methods for shimming have been reported that make use of applied field gradients and do not require any special hardware. Conover described a method referred to as *Z1 profile shimming*, which relies on imaging the magnetic field with the Z1 gradient and manually correcting distortions in expected shape of the profile by adjusting the higher order shims (*102*). An automated procedure referred to as *3D profile edge shimming* has been demonstrated to be quite effective (*113*).

3.8.2.4 Pulse Width Calibration For a spatially homogeneous rf field applied on resonance, the nominal rotation angle is $\alpha = -\gamma B_1 \tau_p$. The pulse duration yielding a particular rotation angle must be determined empirically each time the spectrometer is to be used for an experiment.

Even for the same sample in the same spectrometer, small variations in τ_p may be observed from day to day; however, large increases in τ_p usually indicate mistuning of the probe or equipment failure.

Modern NMR pulse sequences frequently use pulses with reduced amplitudes for solvent saturation, extended rf mixing or spin-locking periods, and selective pulses. Accordingly, the mathematical relationship between attenuation, transmitter power, pulse lengths, and B_1 field strength is useful for approximating the pulse lengths at some attenuation, given the measured pulse lengths at another attenuation. Power levels commonly are measured on the decibel scale:

$$P = P_{ref} \cdot 10^{dB/10}. \quad [3.178]$$

For the dBm scale, $P_{ref} = 1$ mW, and for the dBW scale, $P_{ref} = 1$ W. Thus, an rf amplifier with a maximum power output rated at 20 dBW produces an output of $P = 10^{20/10}$ W $= 100$ W; a preamplifier with a noise figure of -20 dBm produces a noise output of $P = 10^{-20/10}$ mW $= 0.01$ mW. The attenuation difference between two different power levels P_1 and P_2 is given by,

$$dB = 10 \log_{10}(P_1/P_2). \quad [3.179]$$

The B_1 field produced depends upon the voltage in the coil, V, not on the power. Because

$$P = V^2/R, \quad [3.180]$$

in which R is the resistance (typically 50 Ω in a tuned probe),

$$dB = 20 \log_{10}(V_1/V_2). \quad [3.181]$$

The difference between voltage and power is critical: changing the attenuation by 3 dB changes the power by a factor of two, but the attenuation must be changed by 6 dB to change the voltage by a factor of two. Because the B_1 field strength depends on the voltage, doubling the strength of the B_1 field (which is equivalent to halving the 90° pulse length) requires that the power output of the transmitter be quadrupled.

The voltage V in [3.180] is the root-mean-square voltage produced by the rf field. The peak-to-peak voltage, V_{pp}, is more easily measured using an oscilloscope. For a time-dependent voltage, $V(t) = (V_{pp}/2)\cos\omega_{rf}t$, the two quantities are related by

$$V^2 = \frac{V_{pp}^2}{4} \int_0^{2\pi} \cos^2\theta \, d\theta \Big/ \int_0^{2\pi} d\theta = \frac{V_{pp}^2}{8}. \quad [3.182]$$

Combining this result with [3.180] yields the following useful relationship for power measured in watts, voltage measured in volts, and an assumed 50-Ω resistance,

$$P = V_{pp}^2/400. \qquad [3.183]$$

If direct observation of the signal from a particular nucleus is feasible (e.g., ^{1}H), then the length of a 360° pulse is determined by searching for the null in the signal observed after application of the pulse. First, a free induction decay is acquired with a pulse–acquire sequence using a short pulse length. The spectrum is Fourier transformed and phased. The result of this experiment is

$$I_z \xrightarrow{\alpha I_x} I_z \cos\alpha - I_y \sin\alpha, \qquad [3.184]$$

where the pulse applied for a time t produces a net rotation of I_z by α radians. The intensity of the signal will depend upon the rotation angle α (and the time t) in a sinusoidal manner. Determining the length of time required to produce a specific rotation is most accurately accomplished when the observed signal is at a null, i.e., where the pulse produces a rotation by a multiple of π radians. After every pulse–acquire experiment, the system should be allowed to reach equilibrium, so that I_z is at a maximum at the start of the next experiment. For this reason, measurement of a 2π pulse is most accurate: as the null is approached, the magnetization will be rotated almost back to the $+z$-axis and will therefore require less time to return to equilibrium. In addition, a 2π pulse is less sensitive than is a π pulse to resonance offset effects. If the approximate pulse length is not known, care must be exercised to ensure that the null corresponds to a 2π rotation, rather than to a different multiple of π rotations. Once the length of time required for a 2π pulse has been determined, the length of time required for other pulses can be calculated from the proportionality between α and t.

As described in Section 3.4.1, when the offset is large compared to the B_1 field strength, the magnetization does not behave as predicted by [3.184]. Thus, when calibrating the weak pulses required for spin lock or composite pulse decoupling schemes, only the magnitude of signals on resonance should be considered. However, the best solvent suppression is achieved when the H_2O signal is on-resonance, in which case protein peaks that are close to resonance will be obscured by the incompletely suppressed solvent signal. Thus, weak B_1 fields are best calibrated by shifting the transmitter frequency, after the presaturation pulse and prior to the excitation pulse, to be on-resonance with a well-resolved peak,

such as that of an upfield-shifted methyl group. In this way, the pulse length required to achieve a null can be accurately determined without influence of offset effects.

In principle, pulse lengths for the heteronuclear channels can be measured in an analogous way; however, this is rarely practical because of the insensitivity of these nuclei. Further, the heteronuclear experiments described in this book make use of indirect detection of ^{13}C and ^{15}N spins by transfer of coherence to the directly bonded ^{1}H nuclei. Acquisition of such spectra may require different probe and preamplifier configurations than are required for a direct-detect experiment. Because the pulse lengths depend on the exact rf circuitry utilized, pulse lengths for an indirect-detect experiment should be determined by a method that employs the same hardware configuration as employed in the experiments to follow. If the protein sample contains a well-resolved ^{1}H signal scalar coupled to the desired heteronucleus, then the protein sample may be used directly for calibration, although the amount of signal averaging to achieve acceptable signal-to-noise ratios may make such calibrations time consuming. In many cases, heteronuclear pulse lengths can be obtained more readily on a test sample of higher concentration that contains a single labeled moiety for each of the heteronuclei to be calibrated. Small peptides or amino acids are useful for this purpose.

Pulse sequences for indirect calibration rely on the coherence transfer properties of an IS ($I = {}^{1}$H and $S = {}^{13}$C or ^{15}N) spin system. Three pulse schemes for indirect measurements of heteronuclear pulse lengths are given in Fig. 3.48. If the resonance for the I spin attached to the S spin is well resolved, then the pulse sequence of Fig. 3.48a is satisfactory. The product operator analysis of the pulse sequence yields

$$I_z \rightarrow 2I_xS_z \cos\alpha - 2I_xS_y \sin\alpha, \qquad [3.185]$$

in which $\Delta = 1/(2J_{IS})$ and J_{IS} is the scalar coupling constant between the I and S spins. For $\alpha \rightarrow 0$, an antiphase lineshape is obtained; the signal is nulled when $\alpha = \pi/2$, because the $2I_xS_y$ multiple-quantum operator does not evolve into observable coherence during acquisition. The experiment is first run with $\alpha \approx 0$ so that the phase parameters to give an antiphase doublet can be determined; α is then systematically increased until a null is found for the intensity of the doublet. If the spectrum is very crowded, overlapping antiphase components may lead to a large degree of cancellation of the signals and difficulty in accurately determining the pulse length.

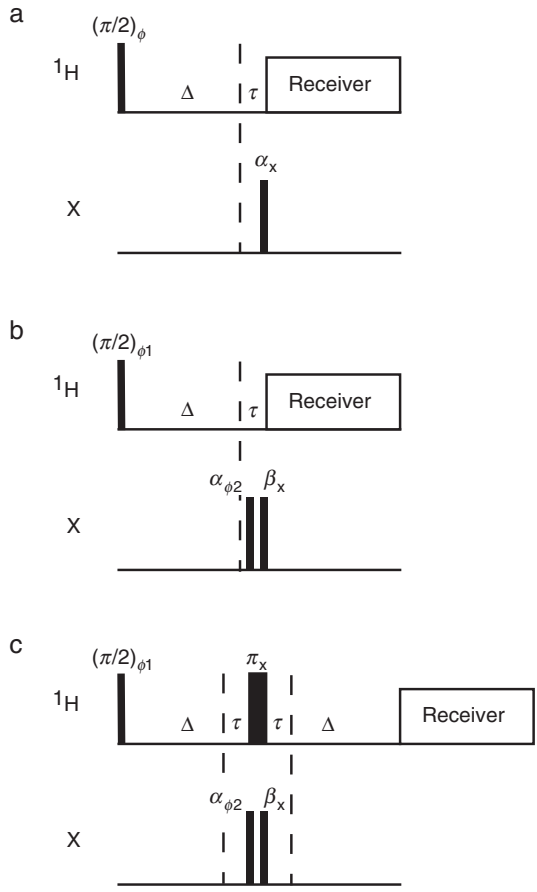

FIGURE 3.48 Pulse sequences for indirect calibration of heteronuclear pulse lengths. In all sequences, $\Delta = 1/(2J_{XH})$ and τ is long enough to encompass the maximum length of the X pulses to be used. Pulses on X nuclei are applied during the delays τ so that the phase of the recorded signal does not depend on the length of the X pulses. Phase cycles are (a) $\phi = \{x, y, -x, -y\}$, receiver $= \{x, y, -x, -y\}$; (b) and (c) $\phi_1 = 2\{x, y, -x, -y\}$, $\phi_2 = \{x, x, x, x, -x, -x, -x, -x\}$, receiver $= \{x, y, -x, -y, -x, -y, x, y\}$. Additional details are given in the text.

If the signal from the *S*-bound ^{1}H spin is not well resolved from signals of ^{1}H spins not bound to heteronuclei (for example, in a peptide containing a single site of ^{15}N incorporation), the signal can be more clearly discerned by using the sequence of Fig. 3.48b. Product operator

analysis yields

$$I_z \rightarrow -2I_xS_z \sin\alpha \sin\beta - 2I_xS_y \sin\alpha \cos\beta. \quad [3.186]$$

This experiment yields antiphase observable signals proportional to $\sin\alpha \sin\beta$. The maximum signal is obtained for $\alpha = \beta \approx \pi/2$, and a null is observed for $\beta = \pi$. This sequence incorporates an isotope filter, by alternating the phase of the first pulse on the heteronuclear channel, so that signals from ^{1}H spins not coupled to an S spin are suppressed. Initially, both α and β are set equal to an estimate of the $\pi/2$ pulse length for the heteronuclear channel, resulting in an antiphase doublet for the S-bound ^{1}H spin. The value of β is then systematically increased, until a null is obtained. Alternatively, in-phase signals can be obtained by using the more elaborate pulse sequence of Fig. 3.48c, which yields

$$I_z \rightarrow -I_y \sin\alpha \sin\beta - 2I_xS_y \sin\alpha \cos\beta. \quad [3.187]$$

Due to the wide spectral widths encountered in ^{13}C and ^{15}N spectra, offset effects can be very severe. Thus, having the S nucleus on-resonance is very important if accurate pulse lengths are to be determined. In cases where the chemical shifts of the S nucleus are not known, the pulses may be roughly measured by estimating the S nucleus frequency. A short HSQC or HMQC experiment (Section 7.1) is acquired to ascertain the exact chemical shift (these experiments are reasonably tolerant to imperfect pulse lengths). With this information in hand, the pulse length can be remeasured accurately.

3.8.2.5 Recycle Delay The optimal combination of the recycle delay between transients and the pulse rotation angle depends upon the rate at which equilibrium magnetization recovers after a perturbation. For signal averaging in a one-pulse experiment with a delay between acquisitions of T (equal to the sum of the recycle delay and acquisition time), the initial amplitude of the FID is proportional to

$$\varepsilon = \frac{1 - e^{-T/T_1}}{1 - e^{-T/T_1}\cos\alpha} \sin\alpha. \quad [3.188]$$

Equation [3.188] is plotted in Fig. 3.49. For a time T, the maximum signal is obtained for a rotation angle, α_e, known as the Ernst angle,

$$\cos\alpha_e = \exp(-T/T_1). \quad [3.189]$$

Thus, if $T < \infty$, then $\alpha_e < 90^\circ$ and $\varepsilon < 1$. Essentially complete recovery of the equilibrium longitudinal magnetization occurs for $T > 3T_1$. Recycle delays of $T_1 < T < 1.5T_1$ yield superior sensitivity per unit time

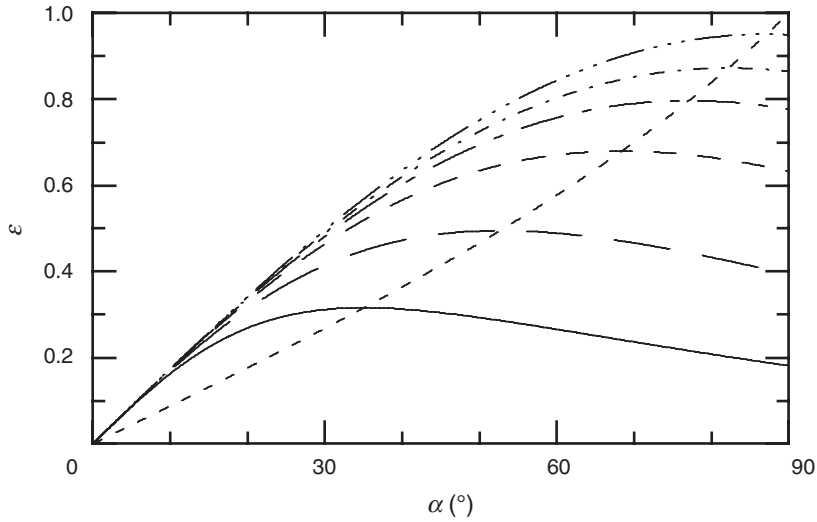

FIGURE 3.49 Ernst angle. The fractional signal intensity, ε, is shown as a function of pulse length, α, in a pulse–acquire NMR experiment. Results are shown for normalized recycle delays, T/T_1, equal to (—) 0.2, (– –) 0.5, (- - -) 1.0, (– - –) 1.5, (–· –·) 2.0, and (–···–) 3.0. The optimal curve yielding the highest value of ε is shown also (- - - -).

and are frequently used in multidimensional experiments, because the reduced recycle delay permits increased signal averaging that offsets the loss of sensitivity due to incomplete relaxation recovery.

The majority of multidimensional homonuclear and heteronuclear NMR experiments used for protein NMR spectroscopy initially excite equilibrium ^{1}H magnetization. The recovery of an equilibrium magnetization state, and therefore the repetition rate of the experiment, depends on the relaxation properties of the ^{1}H nuclei. In order to avoid steady-state artifacts and low amounts of signal per unit of measuring time, the sum of acquisition time and recycle delay usually should be greater than $\sim 1.3T_1$ (Fig. 3.49). The (nonselective) ^{1}H T_1 relaxation rate constant can be estimated from a one-dimensional inversion recovery experiment:

$$\text{recycle}-180^\circ-\tau-90^\circ-\text{acquire}, \qquad [3.190]$$

in which the 90° pulse and receiver are phase cycled in 90° increments. In this case, the recycle delay should be greater than $3T_1$ to ensure complete

relaxation between transients (which may require repeating the experiment following an initial approximate determination of T_1). The magnitude of the transverse magnetization following the 90° pulse varies with the delay, τ, as

$$M(\tau) = M(0)[1 - 2\exp(-\tau/T_1)]. \quad [3.191]$$

The delay is systematically varied until the signal is nulled. The value of T_1 is approximately given by

$$T_1 = \tau_{\text{null}}/\ln 2. \quad [3.192]$$

An example of a nonselective inversion recovery experiment for a ubiquitin sample in D_2O solution is shown in Fig. 3.50. As is evident, the upfield methyl ^{1}H spins in ubiquitin have shorter T_1 values than do the $^1H^{\alpha}$ and aromatic ^{1}H spins, and recover to equilibrium more rapidly. Approximate values of T_1 determined using [3.192] are 0.7, 1.4, and 1.8 s for methyl, α, and aromatic ^{1}H spins, respectively. A small number of persistent $^1H^{N}$ spins with $T_1 \approx 1.0$ s are evident in the spectra.

3.8.2.6 Linewidth Measurement Linewidths, or transverse relaxation rate constants, inevitably determine the sensitivity, or even practicality, of multidimensional NMR experiments, which frequently include extended periods of evolution of transverse coherences. Accordingly, some estimation of the linewidths of the spin resonances is useful in initial assessment of a protein sample. Transverse relaxation of the amide $^1H^{N}$ spins can be estimated from one-dimensional jump–return Hahn echo experiments in which the jump–return technique is used both to avoid saturation of the water signal and to decouple the $^1H^{N}$ and $^1H^{\alpha}$ spins (*114*). The pulse sequence shown in Fig. 3.51 is executed twice for a short, τ_1, and long, τ_2, value of the echo delay, τ. The ratio of signal intensities in the two spectra is used to obtain R_2 from

$$R_2 = -\frac{1}{2(\tau_2 - \tau_1)} \ln \frac{I(\tau_2)}{I(\tau_1)}. \quad [3.193]$$

Spectra for ubiquitin acquired with $\tau_1 = 1$ ms and $\tau_2 = 51$ ms are shown in Fig. 3.52 and yield an average $R_2 = 21.6\,\text{s}^{-1}$ for the envelope of amide resonances. This simple experiment can be elaborated using gradient purge pulses (Section 4.3.3) and selective pulses for decoupling (Section 3.4.4).

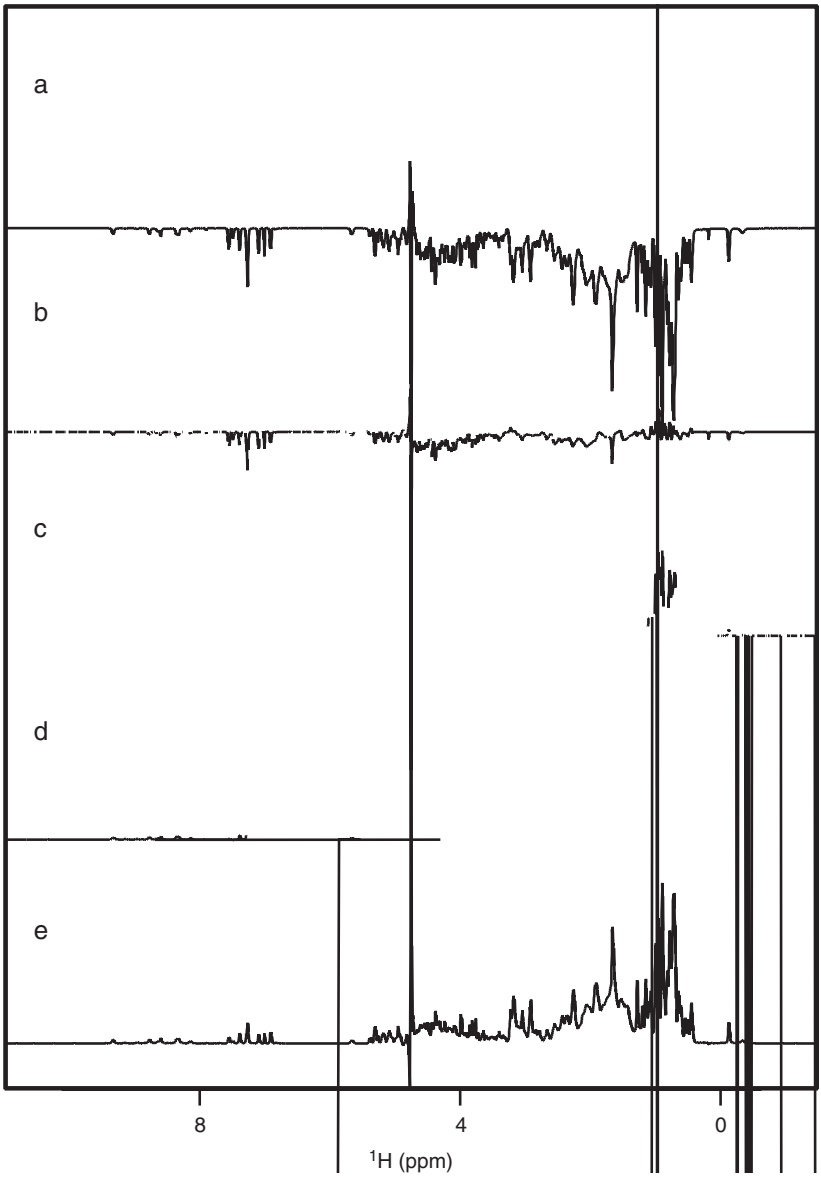

FIGURE 3.50 ^{1}H inversion recovery spectra of ubiquitin. Partially relaxed nonselective inversion recovery spectra of ubiquitin are shown (a–e) for recovery delays of 3 μs and 0.5, 1.0, 1.5, and 2.0 s. Spectra were recorded with a 12-s recycle delay using a ubiquitin sample in 100% D_2O solution.

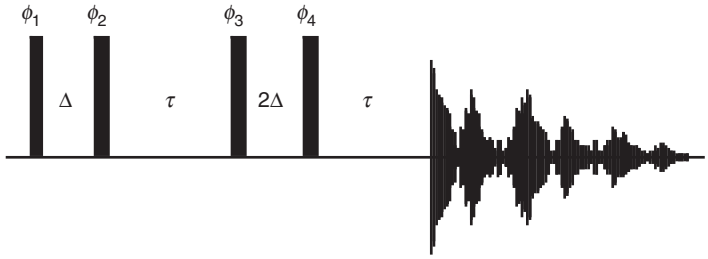

FIGURE 3.51 Pulse sequence for 1D jump–return Hahn echo. The delay $\Delta = 1/(4\Delta\nu_{max})$. The phase cycle is $\phi_1 = x$, $\phi_2 = -x$, $\phi_3 = x, y, -x, -y$, $\phi_4 = -x, -y, x, y$, receiver $= x, -x, x, -x$.

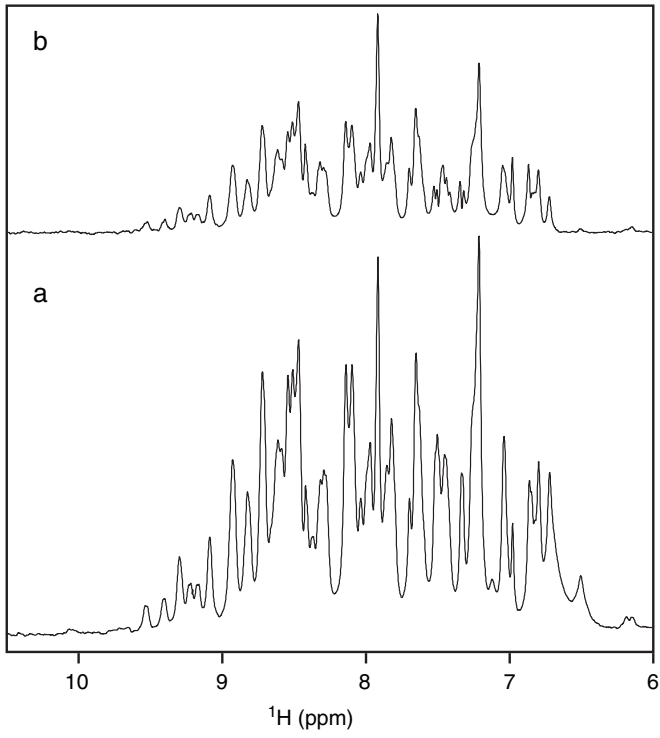

FIGURE 3.52 Estimating ^{1}H R_2 relaxation rate constants. (a) Spectrum of ubiquitin recorded for $\tau = \tau_1 = 1$ ms. (b) Spectrum of ubiquitin recorded for $\tau = \tau_2 = 51$ ms. R_2 is estimated from the ratio of signal intensities using [3.193].

3.8.3 REFERENCING

The concept of the chemical shift was introduced in Section 1.5. To facilitate comparisons of resonance positions between different samples and spectrometers, chemical shifts are measured by reference to a standard compound using units of parts per million, as described by [1.51]. Tetramethylsilane (TMS) is the universal reference for ^{1}H NMR. In studies of organic molecules, TMS can be added directly to the solvent (e.g., deuterated chloroform spiked with TMS is commercially available), thereby providing an internal reference from which the chemical shifts of sample resonances can be determined. The situation is less straightforward in studies of proteins and other biological molecules because TMS is not soluble in aqueous solutions. Instead, either a different internal reference species or an external reference must be used.

The ideal internal chemical shift marker should not interact with the protein under investigation, and should have a single resonance whose chemical shift varies with temperature and pH in a known manner. The resonance should be well resolved from the resonances of the protein, because the reference signal will have a long T_1, and t_1 noise emanating from it may obscure cross-peaks in 2D spectra. The IUPAC–IUBMB–IUPAB Inter-Union Task Group on the Standardization of Data Bases of Protein and Nucleic Acid Structures Determined by NMR Spectroscopy has recommend that the methyl ^{1}H resonance of 2,2-dimethyl-2-silapentane-5-sulfonic acid (DSS; $\delta = 0.00$) be used as the primary chemical shift reference for aqueous solutions of biomolecules (*115*). Concentrations of 10–20 μM DSS are suitable as internal chemical shift reference standards. If DSS binds to the molecule of interest, then alternative internal standards can be used, such as dioxane ($\delta =$ 3.75 ppm); other suitable reference standards are discussed elsewhere (*116*).

Once the ^{1}H shifts are referenced, the heteronuclear chemical shifts are indirectly referenced by using the following relationship (*117, 118*):

$$\nu_0^{\mathrm{X}} = \Xi \nu_0^{\mathrm{H}}, \qquad [3.194]$$

where ν_0^{X} is the absolute frequency of 0 ppm for the X spin, ν_0^{H} is the absolute frequency of 0 ppm for the ^{1}H spin, and Ξ is the relative frequency for the X spin, compared to ^{1}H. Values of Ξ are given in Table 3.2. As an example, if the absolute frequency of DSS is measured to be 500.1366624 MHz at 0.0 ppm, then the absolute zero frequency

TABLE 3.2
Indirect Chemical Shift References[a]

Compound	Ξ	Secondary referenc[b]
^{2}H	0.153506088	DSS (internal)
^{13}C	0.251449530	DSS (internal)
^{15}N	0.101329118	Liquid NH_3 (external)
^{31}P	0.404808636	$(CH_3O)_3PO$ (internal)

[a]Reported values are from the IUPAC recommendations (*115*).
[b]DSS, 2,2-Dimethyl-2-silapentane-5-sulfonic acid.

of ^{15}N is determined from [3.194] to be

$$\nu_0^N = \Xi 500.1366624 = 0.101329118 \times 500.1366624 = 50.67840688\,\text{MHz}. \quad [3.195]$$

Therefore, to perform an HSQC experiment with the ^{15}N region centered in the middle of the amide nitrogen resonances (say at 115.0 ppm), the required experimental offset would be

$$50.67840688(1 + 115.0 \times 10^{-6}) = 50.6842349\,\text{MHz}. \quad [3.196]$$

3.8.4 ACQUISITION AND DATA PROCESSING

Acquisition of ^{1}H spectra is the first step of any investigation by NMR spectroscopy. Such spectra can be acquired by a number of approaches. Two techniques, the one-pulse experiment and the Hahn echo experiment, are discussed in this section. These two experiments can be elaborated to avoid presaturation of the solvent resonance (Section 3.7) or to decouple scalar coupling interactions with heteronuclear spins (Section 3.5).

3.8.4.1 One-Pulse Experiment The basic NMR experiment is the so-called one-pulse experiment in which an rf pulse of rotation angle α is applied to the system and the resulting transverse signal is detected:

$$\text{recycle} - \text{pulse} - \text{acquire}. \quad [3.197]$$

As discussed in Section 4.3.2.3, CYCLOPS phase cycling commonly is used during the one-pulse experiment to suppress quadrature images.

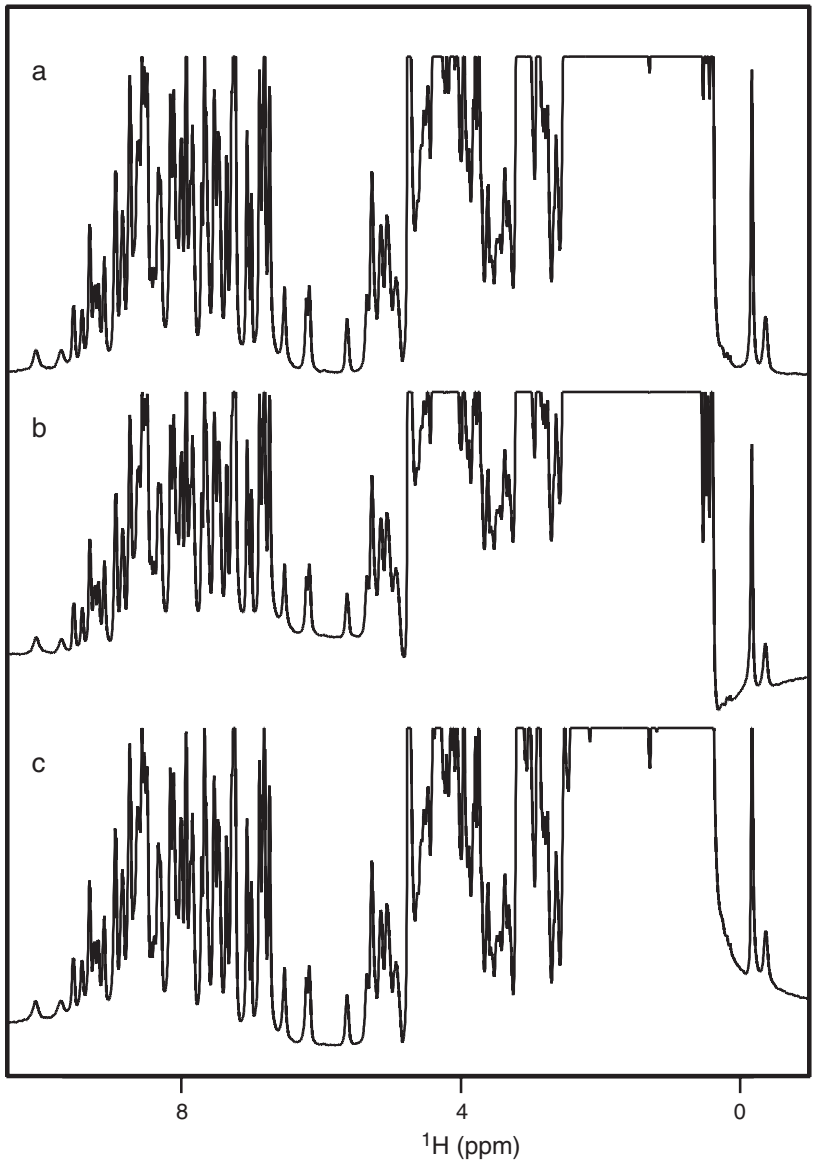

FIGURE 3.53 Hahn echo ^{1}H NMR spectra acquired with a spectral width of 12,500 Hz and a filter width of 30,000 Hz. (a) Echo delays $\tau_1 = 140$ μs and $\tau_2 = 174$ μs are adjusted to eliminate phase errors in the spectrum, (b) τ_2 is misadjusted to be 10 μs shorter than optimal, and (c) τ_2 is misadjusted to be 10 μs longer than optimal.

In CYCLOPS phase cycling, the phase of the pulse and the phase of the receiver are shifted in 90° steps between transients. As a minimum, the following parameters must be adjusted in setting up the one-pulse experiment: recycle delay, rf carrier position, pulse duration, sampling interval or spectral width, number of digitized data points in the time domain, number of transients to be acquired, and receiver amplifier gain. The rf carrier frequency is set to the center of the spectrum or to the frequency of the solvent resonance. Normally the sampling interval, Δt, is adjusted such that the Nyquist frequency is larger than the maximum resonance frequency arising from the sample; however, in some instances, resonances may be deliberately aliased in order to minimize the sampling rate (Section 7.1.2.5). The number of data points acquired, N, is chosen such that $N\Delta t > 3T_2$ in order to minimize truncation artifacts. The receiver gain is adjusted so that the signal arising from the FID does not underflow or overflow the dynamic range of the receiver. The number of transients acquired depends upon the signal averaging required to achieve the desired signal-to-noise ratio in the spectrum; the number of transients must be a multiple of four if CYCLOPS phase cycling is employed.

3.8.4.2 Hahn Echo Experiment The simple one-pulse experiment may not be satisfactory for detailed examination of the one-dimensional spectrum of a biological macromolecule. As was noted in Section 3.3.2.3, baseline distortions can hamper the interpretation of NMR spectra. Removal of baseline distortions can be achieved by the use of a so-called Hahn echo pulse sequence (*119, 120*). This technique, originally introduced for wideline NMR spectroscopy of spin-1/2 nuclei in anisotropic media (*120*), is well suited to application in high-resolution ^{1}H-detected NMR spectroscopy of biomolecules.

In NMR spectroscopy, the entire FID must be recorded to obtain spectra free of distortions. Accurate detection of the early part of the FID is crucial in wideline NMR spectroscopy because the initial signal decays rapidly (the signal typically consists of a broad distribution of resonance frequencies and resonance linewidths can be of the order of several kilohertz). In the simple pulse–acquire detection scheme, a dead time follows the high-power rf pulse as the receiver is saturated and ringing effects are introduced in the tuned circuits. The FID decays markedly during this period; consequently, when the receiver is eventually actuated, the first part of the FID is absent. Rance and Byrd used the Hahn echo pulse sequence

$$90^\circ - \tau_1 - 180^\circ - \tau_2 - \text{acquire} \qquad [3.198]$$

to create a spin echo at τ_2. By having the echo form beyond the receiver dead-time period, the Hahn echo sequence avoids distortions due to finite receiver recovery time.

A similar situation is encountered in high-resolution ^{1}H NMR spectroscopy. Baseline roll in high-resolution spectra, as was discussed in Section 3.3.2.3, commonly is caused by the transient response of the spectrometer to the incoming signal that distorts the first few points of the FID. The Hahn echo sequence allows these distortions to be avoided by the same mechanism as used for wideline spectra.

The delays in the Hahn echo sequence can be calculated as

$$\tau_1 = \tau_2 - 2\tau_{90}/\pi + t_{\text{gate}}, \qquad [3.199]$$

in which τ_2 is greater than the filter response time, τ_{90} is the length of the 90° pulse, and τ_{gate} is the receiver gating delay. In each case, τ_2 is adjusted empirically by small amounts to ensure that acquisition is initiated at the exact top of the echo. As shown in Fig. 3.53, phase errors in the spectrum are eliminated when τ_2 is adjusted accurately. Once τ_2 is optimized with respect to the phase of the spectrum, the value of τ_2 is reduced by enough sample times to allow the filter transient response to decay prior to the top of the echo. Data points acquired prior to the top of the spin echo are discarded before Fourier transformation (*96*). A wide spectral width typically is used for oversampling of the FID (*121*). The basic phase cycle incorporates CYCLOPS phase cycling for the 90° pulse (ϕ) and EXORCYCLE phase cycling for the 180° pulse (ψ) to yield a 16-step phase cycle: $\phi = \{x\,x\,x\,x\,y\,y\,y\,y\,-x\,-x\,-x\,-x\,-y\,-y\,-y\,-y\}$, $\psi = 4\,\{x\,y\,-x\,-y\}$, and receiver $= \{x\,-x\,x\,-x\,y\,-y\,y\,-y\,-x\,x\,-x\,x\,-y\,y\,-y\,y\}$. CYCLOPS and EXORCYCLE are discussed in Section 4.3.2.3.

The Hahn echo sequence is slightly longer than a simple pulse–acquire sequence. Relaxation during the τ_1 and τ_2 delays can reduce the signal intensity; however, the delays are sufficiently short that relaxation effects generally can be safely ignored. Similarly, evolution of the homonuclear scalar coupling occurs during the τ_1 and τ_2 delays. For typical values of $J_{HH} < 15$ Hz, $\cos[\pi J_{HH}(\tau_1 + \tau_2)] > 0.9999$ and $\sin[\pi J_{HH}(\tau_1 + \tau_2)] < 0.016$; consequently, scalar coupling effects also can be ignored. In addition to its other benefits, the Hahn echo sequence also has demonstrated significantly improved water suppression due principally to the refocusing properties of the 180° pulse, which reduces broadening at the base of the residual water peak due to signal originating outside of the homogeneous sample volume. Example one-dimensional NMR spectra acquired with pulse–acquire and Hahn echo pulse sequences are shown in Fig. 3.54.

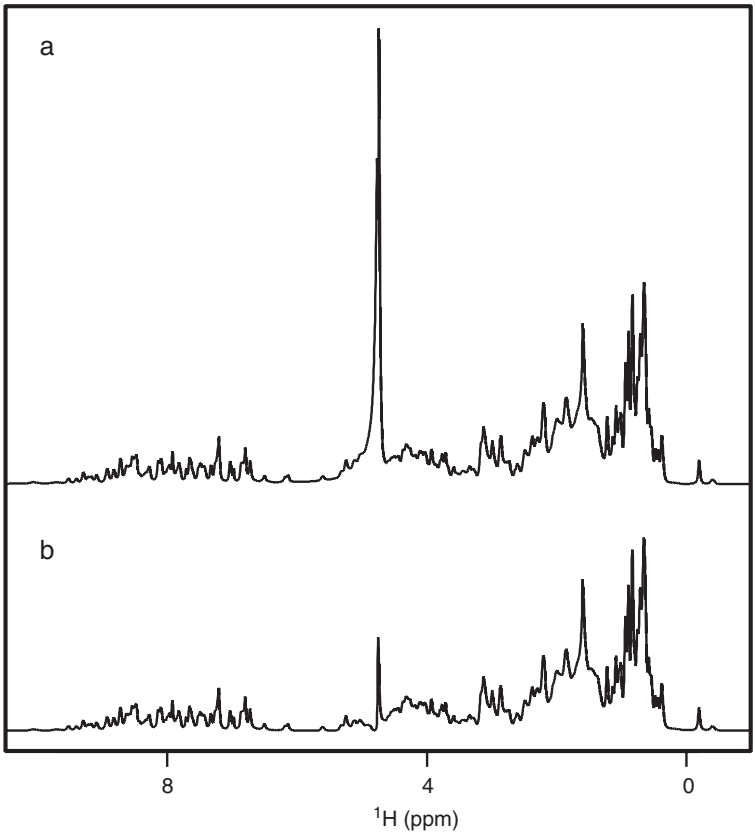

FIGURE 3.54 (a) Pulse–acquire and (b) Hahn echo ^{1}H NMR spectra of ubiquitin. The Hahn echo spectrum has better water suppression and a flatter baseline compared to the pulse–acquire spectrum. Both spectra were acquired with identical spectral and filter widths.

References

1. A. Abragam, "Principles of Nuclear Magnetism," pp.1–599. Clarendon Press, Oxford, 1961.
2. H. Kovacs, D. Moskau, M. Spraul, *Prog. NMR Spectrosc.* **46**, 131–155 (2005).
3. A. E. Kelly, H. D. Ou, R. Withers, V. Dötsch, *J. Am. Chem. Soc.* **124**, 12013–12019 (2002).
4. A. N. Lane, S. Arumugam, *J. Magn. Reson.* **173**, 339–343 (2005).
5. R. W. Dykstra, *J. Magn. Reson.* **84**, 388–391 (1989).
6. T. M. de Swiet, *J. Magn. Reson.* **174**, 331–334 (2005).
7. P. F. Flynn, D. L. Mattiello, H. D. W. Hill, A. J. Wand, *J. Am. Chem. Soc.* **122**, 4823–4824 (2000).

8. M. H. Levitt, *J. Magn. Reson.* **126**, 164–182 (1997).
9. M. H. Levitt, O. G. Johannessen, *J. Magn. Reson.* **142**, 190–194 (2000).
10. R. R. Ernst, G. Bodenhausen, A. Wokaun, "Principles of Nuclear Magnetic Resonance in One and Two Dimensions," pp. 1–610. Clarendon Press, Oxford, 1987.
11. M. H. A. Roehrl, G. J. Heffron, G. Wagner, *J. Magn. Reson.* **174**, 325–330 (2005).
12. D. I. Hoult, C.-N. Chen, H. Eden, M. Eden, *J. Magn. Reson.* **51**, 110–117 (1983).
13. S. L. Marple, "Digital Signal Processing," pp. 1–492. Prentice-Hall, Englewood Cliffs, NJ, 1987.
14. J. G. Proakis, D. G. Manolakis, "Introduction to Digital Signal Processing," pp. 1–944. Macmillan, New York, 1988.
15. A. V. Oppenheim, R. W. Schafer, "Discrete-Time Signal Processing," pp.1–879. Prentice Hall, Englewood Cliffs, NJ, 1989.
16. D. Moskau, *Concepts Magn. Reson.* **15**, 164–176 (2002).
17. J. G. Wurl, Patent 5,652,518 (United States, 1997).
18. J. C. Hoch, A. S. Stern, "NMR Data Processing," pp. 1–196. John Wiley and Sons, New York, 1996.
19. R. N. Bracewell, "The Fourier Transform and Its Applications," 2nd edn., pp. 1–474. McGraw-Hill, New York, 1986.
20. E. Bartholdi, R. R. Ernst, *J. Magn. Reson.* **11**, 9–19 (1973).
21. G. Zhu, D. A. Torchia, A. Bax, *J. Magn. Reson., Ser. A* **105**, 219–222 (1993).
22. A. Bax, M. Ikura, L. E. Kay, G. Zhu, *J. Magn. Reson.* **91**, 174–178 (1991).
23. R. K. Harris, "Nuclear Magnetic Resonance Spectroscopy," pp. 1–260. Longman Scientific and Technical, Harlow, U.K., 1986.
24. H. Barkhuijsen, R. de Beer, W. M. M. J. Bovée, D. van Ormondt, *J. Magn. Reson.* **61**, 465–481 (1985).
25. S. Sibisi, J. Skilling, R. G. Brereton, E. D. Laue, J. Staunton, *Nature (London)* **311**, 446–447 (1984).
26. R. E. Hoffman, A. Kumar, K. D. Bishop, P. N. Borer, G. C. Levy, *J. Magn. Reson.* **83**, 586–594 (1989).
27. J. J. Kotyk, N. G. Hoffman, W. C. Hutton, G. L. Bretthorst, J. J. H. Ackerman, *J. Magn. Reson.* **98**, 483–500 (1992).
28. D. S. Stephenson, *Prog. NMR Spectrosc.* **20**, 515–626 (1988).
29. G. Zhu, A. Bax, *J. Magn. Reson.* **90**, 405–410 (1990).
30. H. Barkhuijsen, R. de Beer, D. van Ormondt, *J. Magn. Reson.* **73**, 553–557 (1987).
31. D. Marion, A. Bax, *J. Magn. Reson.* **83**, 205–211 (1989).
32. E. D. Laue, M. R. Mayger, J. Skilling, J. Staunton, *J. Magn. Reson.* **68**, 14–29 (1986).
33. E.D. Laue, J. Skilling, J. Staunton, *J. Magn. Reson.* **63**, 418–424 (1985).
34. F. Bloch, A. Siegert, *Phys. Rev.* **57**, 522–527 (1948).
35. M. A. McCoy, L. Mueller, *J. Magn. Reson.* **99**, 18–36 (1992).
36. M. A. McCoy, L. Mueller, *J. Magn. Reson.* **98**, 674–679 (1992).
37. M. Sattler, J. Schleucher, C. Griesinger, *Prog. NMR Spectrosc.* **34**, 93–158 (1999).
38. M. H. Levitt, G. Bodenhausen, R. R. Ernst, *J. Magn. Reson.* **53**, 443–461 (1983).
39. A. L. Davis, G. Estcourt, J. Keeler, E. D. Laue, J. J. Titman, *J. Magn. Reson., Ser. A* **105**, 167–183 (1993).
40. M. H. Levitt, *Prog. NMR Spectrosc.* **18**, 61–122 (1986).
41. C. Counsell, M. H. Levitt, R. R. Ernst, *J. Magn. Reson.* **63**, 133–141 (1985).
42. M. A. Smith, H. Hu, A. J. Shaka, *J. Magn. Reson.* **151**, 269–283 (2001).
43. K. Kobzar, T. E. Skinner, N. Khaneja, S. J. Glaser, B. Luy, *J. Magn. Reson.* **170**, 236–243 (2004).

44. J. Keeler, in "Multinuclear Magnetic Resonance in Liquids and Solids-Chemical Applications" (P. Granger, R. K. Harris, eds.), pp. 201–238, Kluwer Academic Publishers, Netherlands, 1990.
45. H. Kessler, S. Mronga, G. Gemmecker, *Magn. Reson. Chem.* **29**, 527–557 (1991).
46. J. Boyd, N. Soffe, *J. Magn. Reson.* **85**, 406–413 (1989).
47. S. L. Patt, *J. Magn. Reson.* **96**, 94–102 (1992).
48. S. Zhang, D. G. Gorenstein, *J. Chem. Phys.* **105**, 5659–5664 (1996).
49. S. Zhang, D. G. Gorenstein, *J. Magn. Reson.* **154**, 73–79 (2002).
50. H. Geen, R. Freeman, *J. Magn. Reson.* **93**, 93–141 (1991).
51. Ē. Kupče, J. Boyd, I. D. Campbell, *J. Magn. Reson., Ser. B* **106**, 300–303 (1995).
52. Ē. Kupče, R. Freeman, *J. Magn. Reson., Ser. A* **105**, 234–238 (1993).
53. Ē. Kupče, *Meth. Enzmol.* **338**, 82–111 (2001).
54. I. I. Rabi, N. F. Ramsey, J. Schwinger, *Rev. Modern Phys.* **26**, 167–171 (1954).
55. J. G. Powles, *Proc. Phys. Soc. (London)* **71**, 497–500 (1958).
56. J. Baum, R. Tycko, A. Pines, *Phys. Rev.* **A32**, 3435–3447 (1985).
57. M. S. Silver, R. I. Joseph, D. I. Hoult, *J. Magn. Reson.* **59**, 347–351 (1984).
58. Ē. Kupče, R. Freeman, *J. Magn. Reson., Ser. A* **115**, 273–276 (1995).
59. F. A. A. Mulder, R. A. de Graaf, R. Kaptein, R. Boelens, *J. Magn. Reson.* **131**, 351–357 (1998).
60. R. A. de Graaf, K. Nicolay, *Concepts Magn. Reson.* **9**, 247–268 (1997).
61. A. Tannus, M. Garwood, *NMR Biomed.* **10**, 423–434 (1997).
62. C. Zwahlen, S. J. F. Vincent, L. E. Kay, *J. Magn. Reson.* **130**, 169–175 (1998).
63. M. R. Bendall, *J. Magn. Reson., Ser. A* **116**, 46–58 (1995).
64. Ē. Kupče, R. Freeman, *J. Magn. Reson.* **127**, 36–48 (1997).
65. J. S. Waugh, *J. Magn. Reson.* **50**, 30–49 (1982).
66. A. J. Shaka, J. Keeler, *Prog. NMR Spectrosc.* **19**, 47–129 (1987).
67. A. J. Shaka, J. Keeler, T. Frenkiel, R. Freeman, *J. Magn. Reson.* **52**, 335–338 (1983).
68. A. J. Shaka, P. B. Barker, R. Freeman, *J. Magn. Reson.* **64**, 547–552 (1985).
69. N. Sunitha Bai, N. Hari, R. Ramachandran, *J. Magn. Reson., Ser. A* **106**, 241–244 (1994).
70. R. Tycko, A. Pines, *Chem. Phys. Lett.* **111**, 462–467 (1984).
71. T. Fujiwara, T. Anal, N. Kurihara, K. Nagayama, *J. Magn. Reson., Ser. A* **104**, 103–105 (1993).
72. R. Fu, G. Bodenhausen, *J. Magn. Reson., Ser. A* **117**, 324–325 (1995).
73. M. R. Bendall, *J. Magn. Reson., Ser. A* **112**, 126–129 (1995).
74. M. McCoy, L. Mueller, *J. Magn. Reson., Ser. A* **101**, 122–130 (1993).
75. A. Wokaun, R. R. Ernst, *Mol. Phys.* **36**, 317–341 (1976).
76. P. B. Kingsley, *J. Magn. Reson., Ser. B* **109**, 243–250 (1995).
77. M. Levitt, *Concepts Magn. Reson.* **8**, 77–103 (1996).
78. W. S. Warren, W. Richter, A. H. Andreotti, B. T. Farmer, *Science* **262**, 2005–2009 (1993).
79. D. L. Mattiello, W. S. Warren, L. Mueller, B. T. Farmer, *J. Am. Chem. Soc.* **118**, 3253–3261 (1996).
80. P. C. M. van Zijl, M. O'Neil Johnson, S. Mori, R. E. Hurd, *J. Magn. Reson., Ser A* **113**, 265–270 (1995).
81. N. Bloembergen, R. V. Pound, *Phys. Rev.* **95**, 8–12 (1954).
82. S. Bloom, *J. Appl. Phys.* **28**, 800–805 (1957).
83. P. J. Hore, *Meth. Enzymol.* **176**, 64–77 (1989).
84. M. Guéron, P. Plateau, M. Decorps, *Prog. NMR Spectrosc.* **23**, 135–209 (1991).
85. P. J. Hore, *J. Magn. Reson.* **55**, 283–300 (1983).
86. P. Plateau, M. Guéron, *J. Am. Chem. Soc.* **104**, 7310–7311 (1982).
87. Y.-C. Li, G. T. Montelione, *J. Magn. Reson., Ser. B* **101**, 315–319 (1993).

88. S. Grzesiek, A. Bax, *J. Am. Chem. Soc.* **115**, 12593–12594 (1993).
89. V. Sklenár, A. Bax, *J. Magn. Reson.* **75**, 378–383 (1987).
90. M. Piotto, V. Saudek, V. Sklenár, *J. Biomol. NMR* **2**, 661–665 (1992).
91. T.-L. Hwang, A. J. Shaka, *J. Magn. Reson., Ser. A* **112**, 275–279 (1995).
92. A. Bax, S. S. Pochapsky, *J. Magn. Reson.* **99**, 638–643 (1992).
93. B. A. Messerle, G. Wider, G. Otting, C. Weber, K. Wüthrich, *J. Magn. Reson.* **85**, 608–613 (1989).
94. D. Marion, M. Ikura, A. Bax, *J. Magn. Reson.* **84**, 425–430 (1989).
95. F. Ni, *J. Magn. Reson.* **99**, 391–397 (1992).
96. J. P. Waltho, J. Cavanagh, *J. Magn. Reson., Ser. A* **103**, 338–348 (1993).
97. N. J. Oppenheimer, *Meth. Enzymol.* **176**, 78–89 (1989).
98. W. U. Primrose, in "NMR of Macromolecules, a Practical Approach" (G. C. K. Roberts, ed.), pp. 7–34. IRL Press, Oxford, 1993.
99. D. S. Raiford, C. L. Fisk, E. D. Becker, *Anal. Chem.* **51**, 2050–2051 (1979).
100. L. P. M. Orbons, G. A. van der Marel, J. H. van Boom, C. Altona, *Eur. J. Biochem.* **170**, 225–239 (1987).
101. A. J. Hartel, P. P. Lankhorst, C. Altona, *Eur. J. Biochem.* **129**, 343–357 (1982).
102. W. W. Conover, in "Topics in Carbon-13 NMR Spectroscopy" (G. C. Levy, ed.), vol. 4, pp. 37–51. John Wiley & Sons, NY (1984).
103. G. N. Chmurny, D. I. Hoult, *Concepts Magn. Reson.* **2**, 131–149 (1990).
104. A. A. Maudsley, H. E. Simon, S. K. Hilal, *J. Phys. Chem.* **E17**, 216–220 (1984).
105. M. G. Prammer, J. C. Haselgrove, M. Shinnar, J. S. Leigh, *J. Magn. Reson.* **77**, 40–52 (1988).
106. P. C. M. van Zijl, S. Sukumar, M. O'Neil Johnson, P. Webb, R. E. Hurd, *J. Magn. Reson., Ser. A* **111**, 203–207 (1994).
107. H. Barjat, P. B. Chilvers, B. K. Fetler, T. J. Horne, G. A. Morris, *J. Magn. Reson.* **125**, 197–201 (1997).
108. G. A. Gray, B. K. Fetler, Varian "Magnetic Moments" (Online, Winter VIII, 1996).
109. M. Weiger, D. Moskau, R. Kerssebaum, W. E. Hull, *Bruker SpinReport*, 3–27 (2005).
110. P. T. Callaghan, "Principles of Nuclear Magnetic Resonance Microscopy," pp. 1–492. University Press, Oxford, 1991.
111. S. Sukumar, M. O'Neil Johnson, R. E. Hurd, P. C. M. van Zijl, *J. Magn. Reson.* **125**, 159–162 (1997).
112. C.-L. Evans, G. A. Morris, A. L. Davis, *J. Magn. Reson.* **154**, 325–328 (2002).
113. P. B. Chilvers, G. A. Morris, *J. Magn. Reson.* **133**, 210–215 (1998).
114. V. Sklenár, A. Bax, *J. Magn. Reson.* **74**, 469–479 (1987).
115. J. L. Markley, A. Bax, Y. Arata, C. W. Hilbers, R. Kaptein, B. D. Sykes, P. E. Wright, K. Wüthrich, *Pure Appl. Chem.* **70**, 117–142 (1998).
116. D. S. Wishart, C. G. Bigam, J. Yao, F. Abildgaard, H. J. Dyson, E. Oldfield, J. L. Markley, B. D. Sykes, *J. Biomol. NMR* **6**, 135–140 (1995).
117. D. H. Live, D. G. Davis, W. C. Agosta, D. Cowburn, *J. Am. Chem. Soc.* **106**, 1939–1941 (1984).
118. A. Bax, S. Subramanian, *J. Magn. Reson.* **67**, 565–569 (1986).
119. D. G. Davis, *J. Magn. Reson.* **81**, 603–607 (1989).
120. M. Rance, R. A. Byrd, *J. Magn. Reson.* **52**, 221–240 (1983).
121. M. Delsuc, J. Lallemand, *J. Magn. Reson.* **69**, 504–507 (1986).
122. M. Edén, Y. K. Lee, M. H. Levitt, *J. Magn. Reson., Ser. A* **120**, 56–71 (1996).
123. G. P. Connelly, Y. Bai, M. F. Jeng, S. W. Englander, *Proteins: Struct. Funct. Genet.* **17**, 87–92 (1993).